Dankwoord

Ik bedank iedereen die op één of andere wijze heeft bijgedragen aan de totstandkoming van mijn proefschrift *"A study into the mechanism of thermoluminescence in a LiF:Mg,Ti Dosimetry material"*.

In het bijzonder bedank ik

dr. Adrie J.J. Bos, voor zijn wijze van begeleiden, voor zijn kritiek, en voor zijn suggesties,
mijn promotoren prof.dr.ir. H. van Dam en prof.dr. A. van Veen, voor hun kritisch doorlezen van het concept-proefschrift en voor de leerzame discussies tijdens werkbesprekingen en daarbuiten,
prof.dr. H.W. den Hartog, voor het leveren van preparaten en voor het gebruiken van zijn absorptiemeetapparatuur,
dr.ir. L.H. Luthjens, voor het ter beschikking stellen van zijn kalibratielampen en de ^{60}Co-bestralingsfaciliteit,
ir. Z.I. Kolar, voor het ter beschikking stellen van zijn thermostaatbad,
de SBD voor het beschikbaar stellen van de bestralingsfaciliteit,
dr. Pieter Dorenbos, Harry Eleveld, en Rogier Visser, voor de interessante discussies over de theorie van de vaste stof,
de studenten Rob Vijverberg, Richard de Jong, Maarten Clement en de stagiair Ton Vermeulen, voor hun bijdrage aan (onder andere) de ontwikkeling van de gebruikte computerprogramma's,
Wim Meulemans, voor zijn onmisbare bijdrage aan de bouw van de opstelling, voor zijn technische ondersteuning en voor de uitvoering van een groot deel van de metingen,
de tekenkamer, instrumentmakerij en de lasserij van het Interfacultair Reactor Instituut (IRI) en de instrumentmakerij van de faculteit Technische Natuurkunde, met name de heren Z. Boerendonk, C. Bok, J. Kolfers, en G. Kerkhof, voor hun grote inzet bij het ontwerpen en bouwen van de onderzoeksfaciliteit,
John Plaisier, voor zijn niet geringe bijdrage aan de ontwikkeling van de elektronische onderdelen van de TL-onderzoeksfaciliteit,
Jan de Roode en Jelle Schut, voor hun advies en hun suggesties,
de groep Cursorisch Onderwijs van het IRI voor het gebruik van hun PC en laserprinter,
Riny Purmer, voor het doorlezen van het proefschrift en het aanbrengen van taalcorrecties
en tot slot alle medewerkers van de vakgroep Reactorfysica voor hun suggesties en discussies tijdens werkbesprekingen en voor de zeer frequent optredende traktaties op koffie met gebak.

Tom Piters

Tom Piters

Curriculum Vitae

naam	Thomas Maria Piters
geboortedatum	9 februari 1962
geboorte plaats	Maastricht

Studieverloop

1981-1988	Studie fysica aan de Rijks Universiteit Utrecht.
1984-1985	Onderzoek naar de oriëntatie van chlorofyl in lipide met behulp van lineairdichroïsme.
1985-1987	Ontwikkeling van een methode om windsnelheid en richting te meten op hoogten van 5 m tot 1 km met behulp van een LIDAR-systeem.
1988	Cursus didactiek.
1988	Doctoraal examen experimentele fysica.
1988-1993	Assistent In Opleiding aan het Interfacultair Reactor Instituut van de Technische Universiteit Delft bij de vakgroep Reactorfysica. Onderwerp: mechanisme van thermoluminescentie in lithiumfluoride gedoopt met magnesium en titaan; bouw TL-emissie-spectrometer.
1989	Cursus stralingshygiëne niveau 3.

Stellingen behorende bij het proefschrift

A Study into the Mechanism of Thermoluminescence in a LiF:Mg,Ti Dosimetry Material

T.M. Piters
oktober 1993

1 De gescheiden dubbele emissiepiek in het spectrum van TLD-100 gemeten door Luff *et al*, is met een aan zekerheid grenzende waarschijnlijkheid een gevolg van een verkeerd toegepaste correctie voor de responsie van de gebruikte meetapparatuur.

Luff B J and Townsend P D (1992) *High sensitivity thermoluminescence spectrometer, Meas. Sci. Technol.* **3** 65, dit proefschrift Hoofdstuk 4 en 6

2 Het warmtecontact tussen preparaat en verwarmingsmedium vormt de belangrijkste factor bij het verkrijgen van reproduceerbare thermoluminescentiemeetresultaten.

Dit proefschrift Hoofdstuk 5, Betts D S and Townsend P D (1993) *Temperature distribution in thermoluminescence experiments. II: some calculational models, J. Phys. D: Appl. Phys.* **26** 849

3 Op grond van reactiekinetiek is het niet uit te sluiten dat meetgegevens van thermoluminescentie of thermisch gestimuleerde geleiding worden verkregen die goed met "snelle *retrapping*" kunnen worden beschreven en tegelijkertijd ook aan de "quasi-evenwichtbenadering" voldoen.

Lewandowski A C and McKeever S W S (1991) *Generalised description of thermally stimulated processes without the quasiequilibrium approximation, Phys. Rev. B* **43** 8163

4 De conclusie dat supralineair gedrag alleen is te verklaren met lege elektronvangstcentra die als concurrenten voor luminescentiecentra dienst doen, is voorbarig. Het is ook mogelijk supralineair gedrag te verkrijgen met concurrenten die bestaan uit niet-lichtgevende recombinatiecentra (defecten met een ingevangen gat) die bij hoge doses verzadigd raken. In dit geval is het ook niet noodzakelijk het lineaire gedeelte van de dosisresponsie toe te schrijven aan een koppeling tussen elektronvangst- en recombinatiecentrum.

Miche E F and McKeever S W S (1989) *Mechanisms of supralinearity in lithium fluoride thermoluminescence dosemeters, Radiat. Prot. Dosim.* **29** 159

5 De zogenaamde "niet door straling geïnduceerde thermoluminescentie" die optreedt in langdurig opgeslagen KCl:Eu^{2+}, wordt veroorzaakt door ioniserende straling afkomstig van het verval van het van nature in KCl aanwezige ^{40}K en niet door het oplossen van Eu-precipitaten tijdens de uitlezing.

Perez Salas R, Barboza-Flores M, Clark Bayon A, and Rodriquez M R (1993) *Evidence of a new thermoluminescent phenomenon in europium doped KCl single crystals, Nucl. Tracks Radiat. Meas.* **21** 151

6 Bij het bepalen van een stralingsdosis in gemengde neutron-gamma stralingsvelden met behulp van een thermoluminescentiedosimeter is de "gloeicurvesuperpositie-methode" ongeveer driemaal nauwkeuriger dan de "tweepiekmethode" in situaties waarbij de bijdrage aan het thermoluminescentiesignaal van één van de stralingscomponenten klein is.

Piters T M, Bos A J J and Zoetelief J (1992) *Thermoluminescence dosimetry in mixed (n,γ) radiation fields using glow curve superposition, Radiat. Prot. Dosim.* **44** 305

7 Het zeer gevoelige thermoluminescentiemateriaal GR-200 verliest zijn gevoeligheid wanneer het te lang aan temperaturen boven 245 °C wordt blootgesteld. De gevoeligheid kan gedeeltelijk worden hersteld door het materiaal 10 minuten op een temperatuur van 600 °C te houden en het vervolgens snel af te koelen tot kamertemperatuur.

8 Een meetresultaat van een bepaald fenomeen dat tegen de verwachting in onafhankelijk blijkt te zijn van een in de theorie opgenomen parameter, is waardevoller voor de theorievorming over dat fenomeen dan een meetresultaat dat afhankelijk blijkt te zijn van een niet in de theorie opgenomen parameter.

9 Indien bij het zoeken naar de beste waarden voor de parameters van een model uit een serie meetgegevens de meetgegevens gecorrigeerd zijn voor de responsie van het meetapparaat, moet er rekening mee worden gehouden dat de fouten in de meetgegevens gecorreleerd zijn. Om problemen bij de zoekprocedure met betrekking tot deze afhankelijkheid te omzeilen is het raadzaam de meetgegevens niet te corrigeren en het model zo aan te passen dat hierin de responsie van het meetapparaat is verwerkt.

10 Bij het invoeren van het één-rij systeem voor verschillende loketten van een bank of postkantoor, zal de gemiddelde wachttijd van de klant niet worden verkort. Wel is er dan bij de klant een verlaging van de gemiddelde stress te verwachten.

A STUDY INTO THE MECHANISM OF THERMOLUMINESCENCE IN A LiF:Mg,Ti DOSIMETRY MATERIAL

T.M. Piters

Interfacultair Reactor Instituut

Technische Universiteit Delft / Delft University of Technology

CIP-GEGEVENS KONINKLIJKE BIBLIOTHEEK, DEN HAAG

Piters, Thomas Maria

A study into the mechanism of thermoluminescence in a LiF:Mg,Ti dosimetry material / Thomas Maria Piters. - Delft : Interfaculty Reactor Institute, Delft University of technology. - I11.
Thesis Technische Universiteit Delft. - With ref.
ISBN 90-73861-13-6
NUGI 812

Subject headings: thermoluminescence / emission spectrometry.

A STUDY INTO THE MECHANISM OF THERMOLUMINESCENCE IN A LiF:Mg,Ti DOSIMETRY MATERIAL

PROEFSCHRIFT

TER VERKRIJGING VAN DE GRAAD VAN DOCTOR
AAN DE TECHNISCHE UNIVERSITEIT DELFT,
OP GEZAG VAN DE RECTOR MAGNIFICUS PROF. IR. K. F. WAKKER,
IN HET OPENBAAR TE VERDEDIGEN TEN OVERSTAAN VAN EEN
COMMISSIE AANGEWEZEN DOOR HET COLLEGE VAN DEKANEN
OP 11 OKTOBER 1993 TE 14.00 UUR

DOOR

THOMAS MARIA PITERS

geboren te Maastricht,
doctorandus in de natuurkunde

Dit proefschrift is goedgekeurd door de promotoren: Prof. dr. ir H. Van Dam en Prof. dr. A van Veen

Dr A.J.J. Bos heeft in hoge mate bijgedragen aan het totstandkomen van het proefschrift

The research described in this thesis has been performed at the Reactor Physics Department of the Interfaculty Reactor Institute of the Delft University of Technology, Mekelweg 15, 2629 JB Delft, The Netherlands.

Contents

Chapter 1

Introduction

1.1 What is thermoluminescence?

Thermoluminescence (TL) is the phenomenon of light emission from an insulator or semiconductor when it is heated after the previous absorption of energy from ionising radiation. Many natural and synthetic materials exhibit this phenomenon. Application of thermoluminescence is found in scientific disciplines like dosimetry (for measuring irradiation dose), archaeology (for dating ancient pottery using the accumulation of background irradiation dose in TL material within the clay which the pottery is made of) and solid state research as a tool to investigate defects in insulators and semiconductors. The background of the research described in this thesis is the interest in dosimetric applications of thermoluminescence.

The application of thermoluminescence to dosimetry has been strongly increased since the work of Daniels *et al* (1953). Thermoluminescence dosimetry has been used for clinical purposes (in radiotherapy and diagnostic radiology), environmental monitoring (*e.g.* near nuclear installations) and reactor engineering (*e.g.* for testing reactor shields) but the most important application is personal dosimetry (*e.g.* in the Netherlands over 25,000 regular radiological workers are equipped with a thermoluminescent dosimeter). Some of the advantages of thermoluminescent detectors (TLD) with respect to other types of detectors (*e.g.* ionisation chambers and film) are their small size allowing high spatial resolution measurements, the large range of measurable doses (from about 1 μGy to 10 kGy), their insensitivity to visible light, humidity and most laboratory fumes and their re-useability (Horowitz 1984 p.11).

The far most wide spread thermoluminescent material used in personal dosimetry is LiF doped with Mg (about 120 ppm) and Ti (about 10 ppm). Its popularity stems from some excellent dosimetric properties: it is tissue equivalent, sensitive to ionising radiation (several μGy), linear in dose response in a large dose range (up to 10 Gy), easy to clean and not hygroscopic.

1.2 Qualitative models for the mechanism of thermoluminescence

1.2.1 Mobile electron model

The mobile electron model for the mechanism of thermoluminescence is based on the energy band theory in insulators (e.g. McKeever 1985, Mahesh *et al* 1989). The model is one of the first models developed for thermoluminescence in alkali halides (Johnson 1939) and its usage for LiF is still wide spread. Figure 1.1 shows schematically the energy levels of an electron in an insulator. The levels are concentrated in the core bands (not shown in Fig. 1.1), valence band and conduction band. For a crystal without lattice defects there are no energy levels between these bands that could be occupied by electrons (band gap). However, when a crystal contains lattice defects (intrinsic or by addition of impurities) the lattice is locally distorted which gives rise to localised energy levels between the valence and conduction band. In the ground state all electrons are localised in the core bands, valence band and the lowest energy levels at the defects.

During irradiation (Fig. 1.1.a) electrons may transit from the valence band into the conduction band leaving a hole in the valence band [transition (1)]. The electron and hole wander through the lattice and come across lattice defects. At a defect the electron may be trapped by a transition to the lowest available energy level at the defect [transition (2)]. The hole may also be trapped at a lattice defect by a transition of the electron from the lowest energy level above the valence band, to the valence band [transition (3)]. So after irradiation an amount of energy is stored in the crystal in the form of separated charge.

When the crystal is heated (Fig. 1.1.b) the charges may be thermally released. The temperature at which the charge carriers (electrons or holes) are released depends on the energy difference of the trap and the conduction band (for electrons) or the valence band (for holes). Let's assume that at a certain temperature the electrons trapped at a certain defect are released [transition (4)]. The electrons wander through the conduction band and may come across a defect with a trapped hole. Due to the relaxation of the lattice around the defect according to the new situation, the electron transits from the ionised state (free electron in conduction band) to an excited state [transition (5)]. This transition is radiationless. The excited electron transits to the ground state (recombination of hole and electron) producing a photon with the energy of the transition [transition

(6)]. The defect where the electron is released is called trapping centre or trap for short. The defect where the electron and hole recombine is called recombination centre or luminescent centre if this recombination produces a photon (as in Fig. 1.1). In this thesis the model used to describe the TL mechanism is based on the mobile electron model.

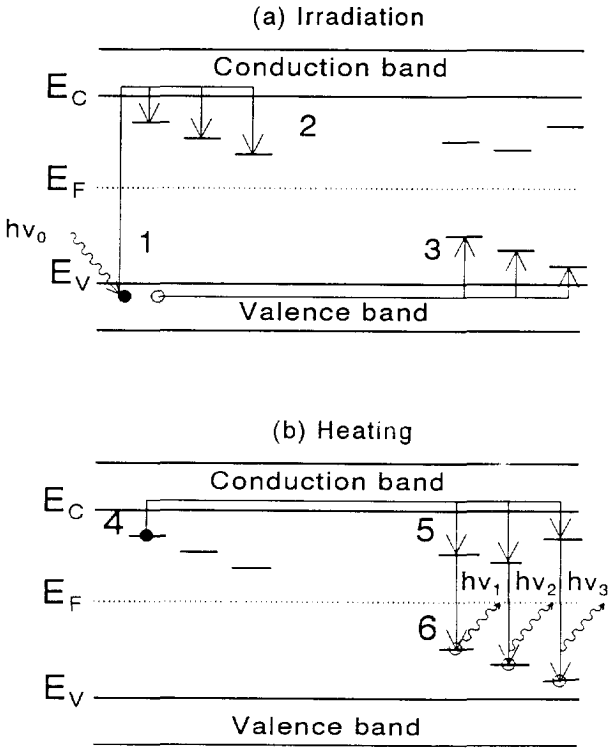

Fig 1.1 Band model for thermoluminescence. E_C is the energy of the bottom of the conduction band, E_V is the energy of the top of the valence band and E_F is the Fermi energy. Transitions are denoted by arrows, electrons by filled circles and holes by open circles.

1.2.2 Mobile interstitial model

The mobile interstitial model is based on the theory of the creation of F-H pairs during irradiation. For thermoluminescence above room temperature of LiF this model was first proposed by Sagastibelza and Alvarez Rivas (1981) and became more and more accepted since.

During irradiation free electrons and self trapped holes (V_k-centre, see Fig. 1.2) are formed. The free electron and V_k-centre recombine and form an exciton. The excitons are mobile and can move around before relaxation. A fraction of the number of excitons is trapped at defect sites (*e.g.* Ti complexes for LiF:Mg,Ti). At high temperature (room temperature) the energy released by the relaxation to the ground state of the (trapped) exciton causes a displacement sequence along the <110> direction of the halide lattice. In this way F-centres (halide vacancy with an electron) and H-centres (halide interstitial with a hole) are formed. The H-centres are mobile and may be captured by impurity defects (like MgV and $(MgV)_3$ in LiF:Mg,Ti) or may cluster to form aggregates. The F-centres are not mobile. So after irradiation the defects formed are impurity defects (MgV and $(MgV)_3$) containing trapped interstitials, impurity defects (Ti complexes) containing F-centres, free F-centres and aggregates of H-centres.

During the readout the H defects dissociate from the impurity defects (*e.g.* MgV and $(MgV)_3$) and become mobile again. They can recombine with F-centres at other impurity defects (Ti complexes) and produce photons. In this picture the moving entities during the readout are not electrons or holes but H-centres.

1.3 Quantitative model for thermoluminescence

For both mechanisms mentioned in section 1.2, thermoluminescence can be described by a phenomenological model. In case of the mobile electron model, the phenomenological model comprises the following rate equations (*e.g.* McKeever 1985):

$$\begin{aligned} \frac{dn}{dt} &= -n\,s\exp\left(-\frac{E}{kT}\right) + n_c\,(N-n)\,A \\ \frac{dn_c}{dt} &= n\,s\exp\left(-\frac{E}{kT}\right) - n_c\,(N-n)\,A - n_c\,n_h\,A_r \\ I_{TL} &= -\frac{dn_h}{dt} = n_c\,n_h\,A_r \end{aligned} \qquad (1.1)$$

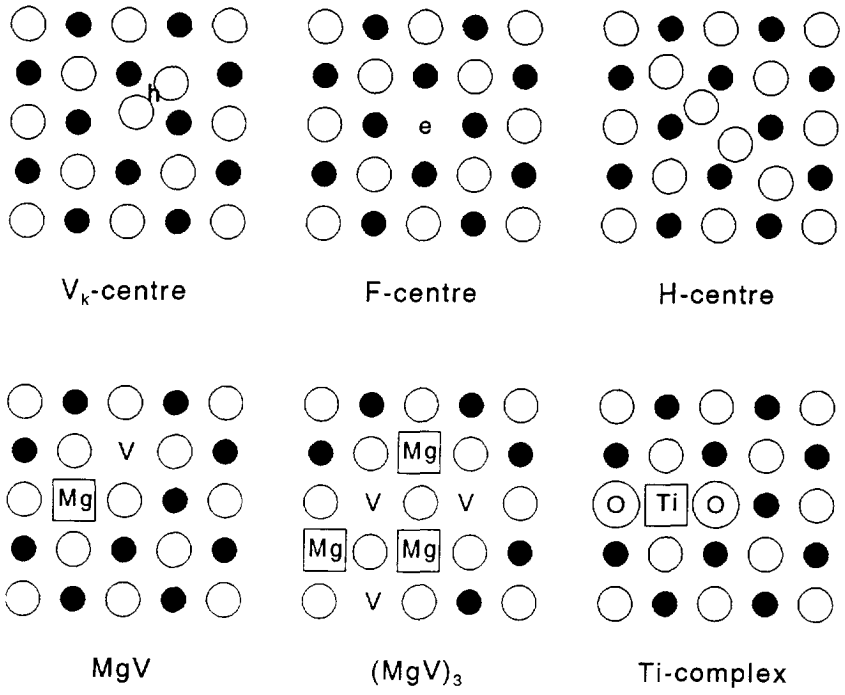

Fig. 1.2 Some defects in an alkali halide lattice. The open circles are the anions (Fluor) and the closed circles are the cations (Lithium).

where n is the concentration of trapped electrons (m^{-3}), n_c is the concentration of electrons in the conduction band (m^{-3}) n_h is the concentration of holes trapped at luminescent centres (m^{-3}), N is the concentration of defects that act as trap (m^{-3}), A is the coefficient for retrapping an electron ($m^3\ s^{-1}$), A_r is the coefficient for recombination of an electron and hole at a luminescent centre ($m^3\ s^{-1}$) and I_{TL} is a quantity proportional to the TL production ($s^{-1}\ m^{-3}$). For TL produced by the release of holes or interstitials (Sagastibelza and Alvarez Rivas 1981) the rate equations are similar to Eq. (1.1). Usually it is assumed that $|dn_c/dt| << |dn/dt|, |dn_h/dt|$ and $n_c << n,n_h$ so $dn/dt \approx dn_h/dt$. The neutrality condition is $n_c + n = n_h$, but since it is assumed that $n_c << n,n_h$, one gets $n = n_h$. With

these assumptions, Eq. (1.1) reduces to:

$$I_{TL} = -\frac{dn}{dt} = \frac{n\,s\exp(-E/kT)}{1+(N-n)\,A/n\,A_r} \tag{1.2}$$

If the coefficients for retrapping and recombination are equal *i.e.* $A = A_r$ then Eq. (1.2) describes a second-order process (power of n is 2)(Garlick and Gibson 1948):

$$I_{TL} = -\frac{dn}{dt} = \frac{n^2}{N}\,s\exp\left(-\frac{E}{kT}\right) \tag{1.3}$$

When retrapping can be neglected *i.e.* $A = 0$ (due to for example, a strong spatial correlation between trapping centres and luminescent centres) Eq.(1.2) describes a first-order process (power of n is 1)(Randall and Wilkins 1945):

$$I_{TL} = -\frac{dn}{dt} = n\,s\exp(-E/kT) \tag{1.4}$$

The power of n in Eqs. (1.3) and (1.4) indicates the order of kinetics. In general Eq. (1.2) has no distinct kinetic order but an n dependence which is weaker than squared (second-order kinetics) and stronger than linear (first-order kinetics). However, one has introduced an effective kinetic order i which has a continuously varying value between 1 and 2 (*e.g.* Chen 1984). The kinetic order i appears in the rate equation of I_{TL} as a power of n:

$$I_{TL} = -\frac{dn}{dt} = n^i\,s\exp(-E/kT) \tag{1.5}$$

where s in this case has the dimension ($s^{-1}\ m^{3i-3}$). Equations (1.3) and (1.4) are special cases of the general order Eq. (1.5) with $i = 2$ and $i = 1$ respectively.

Thermoluminescence is usually measured by the total light emission (integrated over all wavelengths) as a function of the temperature during heating (readout) of the sample with a constant heating rate. The curve obtained in this way is called a glow curve. The technique of measuring glow curves is very sensitive for the absorbed dose (in the order of several μGy) and therefore very useful for personal dosimetry. An example of a glow curve of LiF:Mg,Ti (TLD-100) is shown in Fig. 1.3. The parameters E and s, which describe the different peaks in Fig. 1.3 according to Eq. (1.4) (first-order kinetics), are listed in Table 1.1.

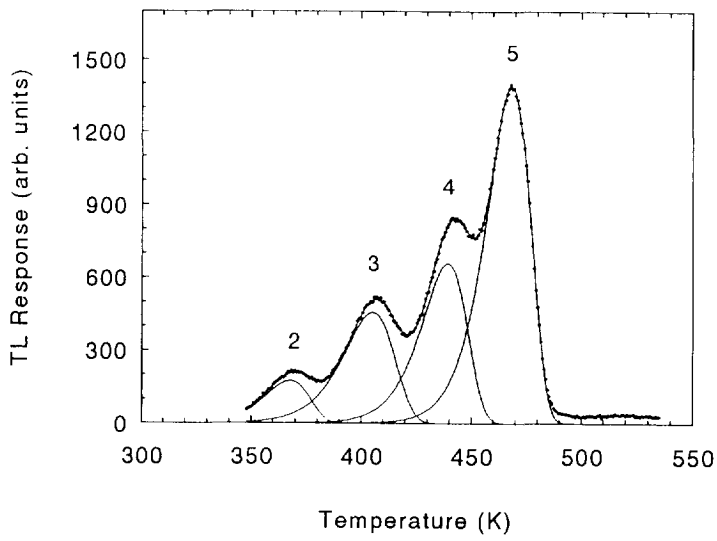

Fig. 1.3 Glow curve of LiF:Mg,Ti (TLD-100). Dots are measured TL intensities and the line is a fit result according to the Randall-Wilkins model. The heating rate during readout is 0.24 K s^{-1}. The data in the figure is obtained from Bos *et al* (1992). The parameters E and s of the glow peaks are listed in Table 1.1.

Table 1.1
Parameter *E* and *s* of LiF:Mg,Ti glow peaks found by glow curve fitting (see Fig. 1.3)

Peak	*E* (eV)	*s* (s^{-1})
2	1.08	1.0×10^{13}
3	1.22	2.5×10^{13}
4	1.61	4.4×10^{16}
5	1.95	1.7×10^{19}

It is possible to obtain information about the kinetic order of the TL process from the asymmetry of a glow peak. The asymmetry of a glow peak can be quantified by a shape parameter $u = d/w$ where d is the lower temperature half half-width and w is the full half-width. For first-order kinetics $u = 0.42$ and for second-order kinetics $u = 0.52$. The value $u = 0.42$ may be used as a criterion for first-order kinetics. However u can only be measured accurately enough for single peaks. Furthermore the criterion assumes an $\exp(-E/kT)$ temperature dependence of the emitted light. A more general criterion for first-order kinetics is that the shape of a glow curve based on first-order kinetics (power of $n = 1$) is independent of the value of the initial concentration of trapped charge carriers $n(t=0)$ (which is proportional to the absorbed dose). This criterion holds for any given temperature dependence of the emitted light and can be measured for single peaks as well as for overlapping peaks. In case of an $\exp(-E/kT)$ dependence of I_{TL} it can be derived (Bos and Dielhof 1991) that if the dose is increased with a factor f the temperature of the maximum intensity shifts to a lower temperature according to:

$$\Delta T \approx T_1 T_2 \frac{k(i-1)}{E} \ln(f) \qquad (1.6)$$

where $\Delta T = T_1 - T_2$, T_1 is the temperature of maximum intensity at a certain dose, T_2 the temperature of maximum intensity at an f times higher dose and i is the order of the reaction. For example, when the activation energy is 2 eV, the peak temperature 400 K and the order 2, one expects a shift of about 47 K when the dose is increased by a factor 1000. For LiF:Mg,Ti (TLD-100) no significant change in the shape and position ($\Delta T < 1$ K) of the glow peaks 2, 3, 4, and 5 has been found within the dose range from 0.0005 Gy to 1 Gy (de Vries *et al* 1988). Thus these glow peaks behave according to first-order kinetics in the mentioned dose range. This is the reason why in this thesis the TL processes in LiF:Mg,Ti (TLD-100) are considered according to first-order kinetics. The model described by the rate equations for first-order kinetics Eq. (1.4) is hereafter referred to as the Randall-Wilkins (RW) model. The model comprises three parameters per trapping centre i.e. the concentration of initially trapped charge carriers $n(t=0)$, the activation energy for releasing a charge carrier E and a frequency factor s.

It is seen from Fig. 1.3, that the RW-model describes the measured TL response very well for LiF:Mg,Ti (TLD-100). However the parameters appear to be dependent on the heating rate during the readout and on the thermal history of

the material (Bos and Piters 1993b). This cannot be explained by the models for the mechanism of thermoluminescent described in section 1.2. Apparently there are other processes involved in the production of TL. Little is known about these other processes.

Note that glow curves only give information about the liberation process [transition (4) in Fig. 1.1]. Information on the recombination process [transition (6)] can be obtained by measuring thermoluminescence as a function of wavelength as well as temperature (TL emission spectrum). However, the technique of measuring emission spectra is much less sensitive for absorbed dose than glow curve measurements. Therefore, measuring TL emission spectra for research into the TL mechanism at low dose levels and possible new dosimetric applications of thermoluminescent material (*e.g.* mixed field dosimetry), is a difficult task.

1.4 The role of defects in thermoluminescence

For LiF:Mg,Ti many attempts have been made to associate the glow peaks of LiF:Mg,Ti with impurity defects, but a consistent picture of the occurring processes is still not available. For example the Z-centre model of Nink and Kos (1976) and later extended by Metha *et al* (1977), relates the glow peaks to Z-centres *i.e.* combinations of Mg ions and F-centres (*i.e.* Z_2' is a Mg^+-F^{2-}-centre, Z_2 is a Mg^+-F^--centre and Z_3 is a Mg^+-F-centre). The Z-centres are identified with optical absorption bands at 225 nm (Z_3), 310 nm (Z_2) and 380 nm (Z_2'). In this model the thermoluminescence at peak 2 (see Fig. 1.3) is a result of the thermal release of an electron from a Z_2'-centre which converts into a Z_2-centre. Peak 5 is a result of the release of an electron from a Z_2-centre. However, the theory has received much criticism (*e.g.* Moharil 1980, Horowitz 1982). According to the Z-centre model the growth characteristics of glow peaks 2 and 5 should be correlated to those of the 380 and 310 nm bands respectively, whereas experiments show that they behave quite differently (Horowitz 1982).

Another model, proposed by Grant and Cameron (1966), associates the glow peaks with MgV and $(MgV)_3$ (where V is an alkali vacancy). The MgV defects and $(MgV)_3$ defects are subject to the reaction:

$$Mg + V \rightleftarrows MgV \rightleftarrows (MgV)_3 \rightleftarrows \text{precipitates} \qquad (1.7)$$

By different annealing procedures the concentration of the different defects can be changed. Comparing dielectric loss experiments with TL measurements lead Dryden and Shuter (1973) to the conclusion that peak 2 and 3 are associated with MgV and peak 4 and 5 with $(MgV)_3$. However, Taylor and Lilley showed that the peak height of peak 2 does not always follow the MgV concentration.

The reason why it is so difficult to relate glow peaks to defects is that glow peaks are associated with two defects a trapping centre and a luminescent centre. The trapping centres and luminescent centres may be involved in other processes than the trap emptying and recombination process which may influence the TL intensity during the readout. So a straight forward comparison of TL measurements with other measurements of defect concentrations like optical absorption and dielectric loss is not possible.

1.5 Motivation of this work

Due to the dependence of the thermal history on thermoluminescence, accurate dosimetry can only be applied when strict procedures for annealing and read out are followed. There is no scientific foundation for the use of a particular procedure due to a lack of understanding of the mechanism of TL. Knowledge of the mechanism of TL in LiF:Mg,Ti is of great importance for improvements in the procedures for accurate dosimetry but also for the development of more sensitive thermoluminescent materials.

An important technique to obtain useful information on the TL mechanism and the processes that influence the thermoluminescence (defect reactions), is the measurement of the light emission during heating of the sample as a function of temperature and photon energy (TL emission spectrum). At absorbed dose levels occurring in personal dosimetry (typically less than 1 mGy), the intensity of the emitted light is so low that an investigation of this light is usually restricted to analysis of the TL emission integrated over all wavelengths (glow curve). Information about the TL mechanism gained from glow curve analysis is limited (Townsend and Kirsh 1989). The information on transition (5) and (6) in Fig. 1.1 is lost and the information about transition (4) is disturbed by the fact that the response of the photo-detector (usually a photomultiplier tube) is wavelength dependent.

Measurements of emission spectra of LiF:Mg,Ti have been done by Crittenden *et al* (1974) , Fairchild *et al* (1978) and Townsend *et al* (1983). But they

were performed at dose levels on the order of 1 kGy. These high dose levels are far from the exposures common in personal dosimetry. It is well-known that the glow curve changes at higher doses [shape of peaks alter and new peaks appear (Jain *et al* 1975)] . Moreover, the intensity of the glow peaks does not vary linearly with increasing dose. Therefore, it is not obvious that the conclusions derived from samples irradiated at high dose levels may be extrapolated to low doses (DeWerd and Stoebe 1972). The main purpose of the work described in this thesis is to construct a TL emission spectrograph for measuring low intensity emission for research into the TL mechanism at dose levels common in personal dosimetry.

In chapter 2 the idea of defect reactions during the readout is introduced as a possible explanation for the dependence of the read-out heating rate on TL. In chapter 3 a model for the description of the emission band is described. The construction of a TL facility comprising the TL emission spectrometer is described in chapter 4. During the readout the sample is heated. The temperature of the sample is measured by the temperature of the heater. A good heat contact between sample and heater is therefore very important. Chapter 5 gives an estimation for the possible errors that are made in the data analysis due to imperfect heat transfer from heater to sample. Chapter 6 shows some measurements with the facility on LiF:Mg,Ti (with different impurity concentrations) submitted to different heat treatments and irradiation doses.

Chapter 2

A model for the influence of defect interactions during heating on thermoluminescence in LiF:Mg,Ti (TLD-100)†

Abstract: Thermoluminescence (TL) in LiF:Mg,Ti (TLD-100) is frequently described with the Randall-Wilkins (RW) model which assumes first-order kinetics. This model fits very well a measured single glow curve (light output as a function of temperature during heating up the sample). If this model describes the TL phenomenon correctly, one expects that the model parameters are not dependent on the experimental conditions. However, the model parameters show a strong dependence on read-out heating rate and annealing procedure. To explain this dependence it is assumed that the defects involved in the TL process are also involved in reactions with other defects. In this chapter, defect reactions are incorporated into the rate equations for TL. Glow curves are simulated at different read-out heating rates for the simple case in which one defect reaction occurs simultaneously with a trap emptying process. It appears that the simulated glow curves can very well be fitted by the RW model and that the dependence of the RW parameters of these simulated curves on the heating rate during read out is comparable with measured data of LiF:Mg,Ti (TLD-100). Moreover, the occurrence of defect reactions during read out gives also an explanation for (a) the dependence of the RW parameters on the annealing procedure and impurity concentration, (b) the too low values of the fading rates predicted by the RW parameters and (c) the unexpected high E and s values of peak 5 of LiF:Mg,Ti (TLD-100).

---

† This chapter is an adapted version of the article "A model for the influence of defect interactions during heating on thermoluminescence in LiF:Mg,Ti (TLD-100) (Piters and Bos submitted).

2.1 Introduction

It has been the subject of many investigations to relate the thermoluminescence glow peaks of LiF:Mg,Ti (TLD-100) to certain defects present in the material and to explain the behaviour of the glow peaks as function of annealing procedure and read-out heating rate. To do so the correlation between the behaviour of the absorption bands (Sagastibelza and Alvarez Rivas 1981) and the dielectric loss5 (Grant and Cameron 1966, Taylor and Lilley 1982a) on the one side and the behaviour of the TL glow peaks on the other have been extensively investigated. Despite of an overwhelming amount of data on this subject (*e.g.* McKeever 1984a) a satisfactory description is still lacking. In most discussions the idea that traps responsible for the TL process in LiF:Mg,Ti react with other defects, plays an important role. For example, Grant and Cameron (1966) proposed a Mg-V dipole for the trap responsible for peak 2 and a $(Mg\text{-}V)_3$ trimer for peak 5. The dipoles can react with each other to form trimers. The trimers can further react with dipoles to form precipitates. Taylor and Lilley (1982b) proposed a somewhat different reaction mechanism. They assumed that the trap responsible for peak 2 in LiF:Mg,Ti (TLD-100) is a Ti complex consisting of Ti, OH and/or O. The Ti complex is denoted by Ti^*. The Ti^* can react with Mg-V dipoles to form another defect with the chemical composition $Ti^*(Mg\text{-}V)$. This defect can further react with the Mg-V dipoles to form $Ti^*(Mg\text{-}V)_m$ which is responsible for peak 5. Next the defect $Ti^*(Mg\text{-}V)_m$ can react with Mg-V dipoles to form precipitates. The two mentioned reaction mechanisms are only concerned with reactions between defects (traps) without any trapped charge carrier. Defects with trapped charge carriers can also be involved in defect interactions, as illustrated by the data of Delgado *et al* (1991). They found that storage of irradiated LiF:Mg,Ti (TLD-100) changes the trap distribution and also causes leakage of trapped charge from one type of trap to another (see also Julius and de Planque 1984).

Although it has been realised that interaction between defects also occurs during the TL read-out cycle and could influence the TL properties (Taylor and Lilley 1982c), it has been neglected in the description of the glow curve. Thermoluminescence in LiF:Mg,Ti (TLD-100) at low doses follows first-order kinetics (see chapter 1) and is usually described by the Randall-Wilkins (RW) model (see Eq. (1.4) in chapter 1). The RW model comprises three parameters per trapping centre i.e. the concentration of initially trapped charge carriers $n(t=0)$, the activation energy for releasing a charge carrier E and a frequency

factor *s*.

A number of methods for the experimental determination of the trapping parameters *E* and *s* exists. For example, the trapping parameters can be determined by isothermal decay experiments, glow curve fitting, peak shape method, analyzing the initial rise of the glow curve and by analyzing heating rate plots (Kirsh 1992). The parameters found by any method based on the RW model are further referred to as Randall-Wilkins (RW) parameters. For LiF:Mg,Ti (TLD-100) these different methods yield good fitting results. However, there are large discrepancies between the parameter values found by different authors (Yeh and Weng 1991). In particular the *E* and *s* values of the main peak of TLD-100 (peak 5) tend to be much lower for isothermal decay experiments than for glow curve measurements at heating rates ranging from 0.1 K s^{-1} to 10 K s^{-1} (Yossian *et al* 1993). Moreover, there are some observations concerning TL in LiF:Mg,Ti that cannot be explained by the RW model. For example:

1) The annealing procedure influences the values of the RW parameters $n(t=0)$, *E* and *s* obtained by glow curve fitting for most of the glow peaks (Bos and Piters 1993a).
2) The RW parameters depend on the read-out heating rate (Kitis *et al* 1993, Bos *et al* 1992). For example, the peak area, activation energy and frequency factor of the so-called peak 2 increases when the heating rate is varied from 0.2 K s^{-1} to 6 K s^{-1}.
3) The fading rates of the glow peaks at room temperature calculated from the RW parameters obtained from glow curve fitting are much lower than the measured fading rates (Bos 1988, Bos and Piters 1993b).
4) The frequency factor *s* obtained by glow curve analyses of the main TL peak (peak 5) is somewhere between 10^{19} s^{-1} and 10^{24} s^{-1} (Taylor and Lilley 1978). This value is unexpectedly high. Realistic values of *s* are on the order of the Debye frequency 10^{11} - 10^{13} s^{-1} (Böhm and Scharmann 1981).
5) The concentration of the impurities Ti and Mg influences the RW parameters of the glow peaks (Vana and Ritzenger 1983).

From these observations it is clear that, although the RW model mathematically describes the LiF:Mg,Ti (TLD-100) glow curve very well, there must be other processes than the one described by the RW model, involved as well. A number of extensions of the RW model have been proposed.

Levy (1984) formulated rate equations for thermoluminescence in cases

where charges released from one type of trap may be retrapped in other types of traps (so-called interactive kinetics). This model may explain some of the properties of TL in LiF:Mg,Ti. However, this model predicts even at low doses a strong dependence of the RW parameters on irradiation dose which has not been observed in LiF:Mg,Ti (TLD-100) (see chapter 1).

Tale *et al* (1990) suggested that a trap actually consists of two levels with different activation energies. Transitions between these levels occur due to reorientation of the defect and it is assumed that the distribution over the two levels is that of thermal equilibrium.

Piters and Bos (1991) suggested a semi-continuous level distribution. They assumed that the activation energy of a trap is affected by the surrounding defects of the trap. Transitions between the levels can occur due to the mobility of the surrounding defects.

Lewandowski and McKeever (1991) developed a generalized description of TL, taking into account the life-time of the charge carriers before recombination.

Simulations of single glow peaks according to the above mentioned models show that the fitted RW parameters E and s can change as a function of the heating rate during read out. However they are not able to explain the changes in peak area as function of the heating rate.

None of the above mentioned models accounts for the effect of defect reactions during read out. The purpose of this chapter is (1) to present a model for TL that incorporate the idea of defect reactions during read out and (2) to investigate whether this model can explain the observed behaviour of the RW parameters in LiF:Mg,Ti (TLD-100). The development of the model is carried out for one TL producing trapping centre that contributes to a simple defect reaction. Simulations of glow curves are performed with the parameters chosen in such a way that the results of the simulation could be compared with measured data of LiF:Mg,Ti (TLD-100).

2.2 The interactive defect model

In this section the influence of defect reactions on thermoluminescence is described. Firstly the influence is described in general, next some simplified defect reactions are described in more detail.

Defects are hereafter denoted by capitals (*e.g.* A, A_i, B, ..). When a distinction in notation is desired between defects with and without a trapped charge carrier, the defects with trapped charge carriers are denoted by an asterisk (*e.g.* A^*, B^*, C^*, ..). The charge carrier could be an electron or a hole but also an interstitial halogen atom as proposed by Sagastibelza and Alvarez Rivas (1981). A free charge carrier is denoted by an e. The concentration of a defect is denoted by n with a subscript indicating the type of defect.

Defects can be subjected to more than one defect reaction. In general, for a specified reaction k with m different types of defects A_i, the reaction equation can be written as (*e.g.* Agullo-Lopez *et al* 1988 p. 31):

$$a_{1k}A_1 + \ldots + a_{ik}A_i + \ldots + a_{mk}A_m \rightarrow a'_{1k}A_1 + \ldots + a'_{ik}A_i + \ldots + a'_{mk}A_m \qquad (2.1)$$

where a_{ik} and a'_{ik} are the stoichiometric numbers (a_{ik} = 0,1,2,...) characteristic for reaction k, and i is an integer number ($1 \le i \le m$). If we adapt the theory of chemical kinetics in solutions (*e.g.* Moelwyn Hughes 1971 p. 72) for reactions between defects in solids the reaction rate α is:

$$\alpha_k = \prod_i n_i^{a_{ik}} s_k \exp\left(-\frac{E_k}{kT}\right) \qquad (2.2)$$

where n_i is the concentration of defect A_i, E_k the activation energy for this reaction and s_k a pre-exponential factor characteristic for this reaction. The pre-exponential factor s_k is in general dependent on the temperature typically of the form T^a (with $-1 \le a \le 1$, Moelwyn-Hughes 1988). Because this temperature dependence is very weak compared to the exponential dependence we assume that s_k is independent of the temperature. To illustrate the usage of Eq. (2.1) and Eq. (2.2) consider the defect reaction $3(MgV) \rightarrow (MgV)_3$ in LiF:Mg,Ti (TLD-100). In the formalism of Eq. (2.1) this reaction can be written as:

$$3\,MgV + 0\,(MgV)_3 \rightarrow 0\,MgV + 1\,(MgV)_3 \qquad (2.3)$$

The rate of this reaction is according to Eq. (2.2):

$$\alpha = n_{MgV}^3 s \exp\left(-\frac{E}{kT}\right) \qquad (2.4)$$

This reaction has been investigated by Taylor and Lilley (1982a). They found for

the parameters s = 1.3 $\cdot 10^{16}$ s^{-1} (mole fraction)$^{-2}$ and E = 0.83 eV. Note that this reaction does not contain any defect with trapped charge carriers. The goal of this chapter is to include reactions with defects with trapped charge carriers as well and to investigate the consequences of these reactions on the TL process.

The rate equations for the defect concentrations depend on the possible reactions in which the defects are involved. Table 2.1 shows some possible reactions involving A^* and the corresponding term in the rate equation for n_{A^*}. Reactions where A^* is one of the end products contribute to an increase of n_{A^*} (positive sign). Reactions where A^* is one of the starting products contribute to a decrease of n_{A^*} (negative sign). In general the rate equation of the concentration of the defect of type i is:

$$\frac{dn_i}{dt} = \sum_k \Delta a_{ik}\, \alpha_k \qquad (2.5)$$

where $\Delta a_{ik} = a'_{ik} - a_{ik}$.

Table 2.1 Some examples of defect reactions involving defect A^*. The effect of the reaction on the concentration of A^* is seen in the third column (contribution to $\dot{n}_{A^*}$). Column 4 (contribution to I_{TL}) shows the effect of the reaction to the thermoluminesce

Case	Reaction	Contribution to $\dot{n}_{A^*}$	Contribution to I_{TL}
(a)	$A^* \rightarrow A + e$	$-n_{A^*} s_a \exp(-E_a/kT)$	$n_{A^*} s_a \exp(-E_a/kT)$
(b)	$A^* + B \rightarrow C^*$	$-n_{A^*} n_B s_b \exp(-E_b/kT)$	0
(c)	$A^* + B \rightarrow C + e$	$-n_{A^*} n_B s_c \exp(-E_c/kT)$	$n_{A^*} n_B s_c \exp(-E_c/kT)$
(d)	$A^* + B \rightarrow A + B^+ + e$	$-n_{A^*} n_B s_d \exp(-E_d/kT)$	$n_{A^*} n_B s_d \exp(-E_d/kT)$
(e)	$A^* + B \rightarrow A + B^*$	$-n_{A^*} n_B s_e \exp(-E_e/kT)$	0
(f)	$A^* + B^* \rightarrow C^{**}$	$-n_{A^*} n_{B^*} s_f \exp(-E_f/kT)$	0
(g)	$A^* + B^* \rightarrow C^* + e$	$-n_{A^*} n_{B^*} s_g \exp(-E_g/kT)$	$n_{A^*} n_{B^*} s_g \exp(-E_g/kT)$
(h)	$A^* + B^* \rightarrow C + 2e$	$-n_{A^*} n_{B^*} s_h \exp(-E_h/kT)$	$2n_{A^*} n_{B^*} s_h \exp(-E_h/kT)$
(i)	$A^* + B^* \rightarrow A + B^* + e$	$-n_{A^*} n_{B^*} s_i \exp(-E_i/kT)$	$n_{A^*} n_{B^*} s_i \exp(-E_i/kT)$
(j)	$A + B^* \rightarrow A^* + B$	$+n_A n_{B^*} s_j \exp(-E_j/kT)$	0
(k)	$C^* \rightarrow A^* + B$	$+n_{C^*} s_k \exp(-E_k/kT)$	0

For TL in LiF:Mg,Ti (TLD-100) irradiated at room temperature at a low dose (less than 1 Gy) an important reduction in the number of possible reactions can be made. For low doses the concentration of filled traps is so low (less than $3x10^{-8}$ mole fraction) that (1) reactions between filled traps can be neglected, (2) the concentration of unfilled traps (between 10^{-6} - 10^{-3} mole fraction) is not significantly affected by the changes in the concentration of filled traps and (3) the concentration of filled traps is proportional to the absorbed dose. As a consequence each term in the sum of Eq. (2.5) of which Δa_{ik} is not zero contains the concentration of one and only one type of filled trap. The shape of the glow curve described by such a set of differential equations is independent of the absorbed dose and the intensity of the TL signal is proportional to the absorbed dose (first-order kinetics). This is indeed the case for LiF:Mg,Ti (TLD-100) at low doses (*e.g.* Busuoli 1981, de Vries *et al* 1988). In this chapter only reactions of this reduced set of possible reactions are described.

The light production can be found by adding up all terms that represent reactions involving the recombination between an electron and a hole multiplied by an efficiency factor. The efficiency may be dependent on temperature (quenching). However, we assume no temperature dependence.

It is not difficult to construct the rate equations for the defect concentrations even for a large number of different types of defects and defect reactions. However, as the number of possible reactions and different types of defects increases, it becomes more difficult to draw general conclusions about the behaviour of the system. Therefore, the behaviour of some very simple cases is investigated.

Consider a TL material containing defects of types A, B, C and D. Defects A and C are electron traps and form with a trapped electron A^* and C^*. Defect D acts as luminescent centre (see Fig. 2.1). It is assumed that thermoluminescence in the considered temperature region is only due to trap emptying of defect A^*. Defect C^* does not empty in the considered temperature region. During thermoluminescence it is assumed that the concentration of free charge carriers is in a quasi equilibrium state *i.e.* the rate of trap emptying is equal to the rate of recombination. In this case the light production is proportional to the rate of trap emptying (reaction (a) in Table 2.1). Defect A^* and C^* can be involved in a defect reaction with defect B. Defect A^* may react with B to form C^* (reaction (b) in Table 2.1) and C^* may dissociate into A^* and B (reaction (k) in Table 2.1). Figure 2.1 shows the energy levels and the possible transitions due to the trap emptying (a) and defect reactions (b) and (k). Three cases denoted as (**I**), (**II**)

and (III) are investigated. The differences between the cases are in the possible reactions between the defects A^*, B and C^*.

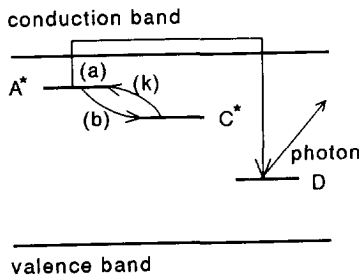

Fig. 2.1 Energy level diagram of the ID model. The arrows indicate transitions due to (a) trap emptying, (b) defect reaction $A^* + B \rightarrow C^*$, and (k) the inverse defect reaction $C^* \rightarrow A^* + B$. Only the trap emptying process leads to light production. Reactions (a), (b) and (k) are listed in Table 2.1

Case (I): Defect reaction $A^* + B \rightarrow C^*$.
In this case reactions (a) and (b) of Table 2.1 occur:

$$\begin{aligned} A^* &\rightarrow A + e \\ A^* + B &\rightarrow C^* \end{aligned} \qquad (2.6)$$

Both reactions contribute to the total rate of the decrease of n_{A^*} but only the first reaction contributes to the light production I_{TL} (due to electron hole recombination):

$$\begin{aligned} \frac{dn_{A^*}}{dt} &= -\alpha_a - \alpha_b \\ I_{TL} &= \eta\,\alpha_a \end{aligned} \qquad (2.7)$$

where $\alpha_a = n_{A^*} s_a \exp(-E_a/kT)$, $\alpha_b = n_{A^*} n_B s_b \exp(-E_b/kT)$ and η is the efficiency of the TL process. For the equations the real value of η is not important, it only scales the light output. Without loss of generality, η is assumed to be equal to 1. Note that s_a and s_b have different dimensions *i.e.* the dimension of s_a is s^{-1} and that od s_b is $m^3\ s^{-1}$.

As a first approximation we assume that the concentration of B does not change significantly. This is the case when n_B is much larger than n_{A^*} and the defect B is not significantly involved in other reactions.

In the limit $\alpha_b = 0$ Eq. (2.7) reduces to the set of equations according to the RW model. In the limit $\alpha_a << \alpha_b$ the rate equations of n_{A^*} and I_{TL} become:

$$\begin{aligned} \frac{dn_{A^*}}{dt} &= -n_{A^*} n_B s_b \exp(-E_b/kT) \\ I_{TL} &= n_{A^*} s_a \exp(-E_a/kT) \\ &= n_{A^*} n_B s_b \exp(-E_b/kT) \ \frac{s_a}{n_B s_b} \exp(-(E_a - E_b)/kT) \end{aligned} \tag{2.8}$$

So the light production I_{TL} is that of the RW model with parameters $E \approx E_b$ and $s \approx n_B s_b$, multiplied by $(s_a/n_B s_b)\exp(-(E_a-E_b)/kT)$. The factor $s_a/n_B s_b$ only scales the light output, but does not change its shape. The exponential factor $\exp(-(E_a-E_b)/kT)$ is a rapidly increasing function of T. The effect of multiplying a glow peak with this function is that the glow peak shifts to a higher temperature and that the width of the peak decreases. This may lead to high values of s if this glow curve is analyzed with the RW model. Because $\alpha_a << \alpha_b$, practically all traps are involved in the defect reaction and very few in the trap emptying process. Therefore, the TL production is not very efficient and $n(t=0) << n_{A^*}(t=0)$.

Case (II): Reaction $C^* \rightarrow A^* + B$

In case (II) the possible reactions are (a) and (k) of Table 2.1:

$$\begin{aligned} A^* &\rightarrow A + e \\ C^* &\rightarrow A^* + B \end{aligned} \tag{2.9}$$

Now the rate equations become:

$$\begin{aligned} \frac{dn_{A^*}}{dt} &= -\alpha_a + \alpha_k \\ \frac{dn_{C^*}}{dt} &= -\alpha_k \\ I_{TL} &= \alpha_a \end{aligned} \tag{2.10}$$

were $\alpha_k = n_C s_k \exp(-E_k/kT)$. The solution of these equations depends on the defect concentrations at $t = 0$: $n_{A^*}(t=0)$ and $n_{C^*}(t=0)$. In general the defect concentrations of A^* and C^* at $t = 0$ are both not zero. The exact distribution of the two defect concentrations depends on the capture cross-section for charge

carriers during irradiation. For simplicity it is assumed that $n_{C^*}(t=0) \neq 0$ and $n_{A^*}(t=0) = 0$. The behaviour of Eq. (2.10) of two extreme cases are now further explored.

Firstly we consider the case: $s_a\exp(-E_a/kT) >> s_k\exp(-E_k/kT)$. In this case the traps A^* that are produced by the dissociation of C^*, empty immediately so the concentration n_{A^*} stays almost zero. In other words $dn_{A^*}/dt = 0$ so $\alpha_a = \alpha_k$ (see Eq. (2.10)). From Eq. (2.10) it can be derived that the produced glow curve in this case is that of the RW model according to the parameters $s = s_k$ and $E = E_k$.

Next we consider the case: $s_a\exp(-E_a/kT) << s_k\exp(-E_k/kT)$. Now n_{A^*} firstly increases till $n_{A^*} = n_{C^*}(t=0)$. When the temperature is high enough, n_{A^*} decreases according to the RW model with the parameters $s = s_a$ and $E = E_a$. The light production is also according to the RW model with the same parameters $s = s_a$ and $E = E_a$.

In the intermediate case where the parameters are chosen such that $s_a\exp(-E_a/kT) \approx s_k\exp(-E_k/kT)$ it is less clear in what way the glow curve will behave. In the temperature range where the defect A^* empties, the concentration of A^* increases till most of the defects C^* are dissociated. The glow peak becomes narrower and its maximum shifts to a higher temperature than expected from the RW model with parameters $s = s_a$ and $E = E_a$. This may lead to high s and E values when the glow curve is fitted with the RW model (see paragraph 2.3).

Case (III): $A^* + B \rightleftharpoons C^*$

A more complicated situation emerges when the reactions of both cases (I) and (II) occur simultaneously. The reactions that describe the thermoluminescence process are now:

$$\begin{aligned} A^* &\rightarrow A + e \\ A^* + B &\rightleftharpoons C^* \end{aligned} \qquad (2.11)$$

The set of differential equations that describe the TL becomes:

$$\begin{aligned} \frac{dn_{A^*}}{dt} &= -\alpha_a - \alpha_b + \alpha_k \\ \frac{dn_{C^*}}{dt} &= \alpha_b - \alpha_k \\ I_{TL} &= \alpha_a \end{aligned} \qquad (2.12)$$

Eq. (2.7) which describes case (I) is obtained from Eq. (2.12) by choosing the parameters in such way that $\alpha_k=0$. In this case the rate equation for n_{A^*} and the equation for I_{TL} in Eq. (2.12) are the same as in Eq. (2.7). The rate equation for n_{C^*} is of no interest in case (I) because it does not affect the TL production. Equation (2.10) which describes case (II) is obtained for $\alpha_b=0$.

An interesting property of Eq. (2.12) is that it can produce two glow peaks. This is the case when the parameter values are such that at low temperatures α_a, $\alpha_b >> \alpha_k$ and at high temperatures $\alpha_k >> \alpha_b$. The first peak emerges when the defects A^* are emptied. When at higher temperatures the defect C^* dissociates into A^* and B, the created A^* defects empty immediately. This causes the second peak.

2.3 Simulations and results

For cases (I), (II) and (III) some simulations were carried out. The glow curves obtained by these simulations were fitted with the RW model to investigate the influence of defect interactions on the RW parameters.

The simulations and analyses were performed with a VAX-4300 computer. The differential equations were solved with the Bulirsch-Stoer method (Press *et al* 1988 p. 563). For case (II) and (III) the Bulirsch-Stoer method was modified with the implicit Euler scheme to obtain stability (Press *et al* 1988 p. 572). The fits were carried out with the routine FATAL (Fits Anything To Anything you Like, Salmon and Booker 1972). The "goodness of fit" was measured by the FOM (Figure Of Merit, Balian and Eddy 1977) defined as:

$$\mathrm{FOM} = \frac{\sum_{i=1}^{N} |(x_i - y_i)|}{\sum_{i=1}^{N} y_i} \qquad (2.13)$$

where x_i are the simulated data points, y_i the data points of the fit and N the number of data points. Following Balian and Eddy (1977), a FOM less than 2 % indicates a good fit. There is no special reason for using the FOM as measure for the "goodness of fit". In fact any measure for the "goodness of fit" which is independent of a scale factor in the intensity of the glow curve could be used.

Table 2.2 shows all the parameters used in the simulations. The choices for the values of the parameters $n_{A^*}(t=0)$ and $n_{C^*}(t=0)$ do not influence the shape of the simulated glow curves. A different choice would only scale the simulated glow curves. The choices of the parameters E_a, s_a, E_b and $n_B s_b$ in cases (I.a) through (I.d) were chosen in such way that the width and position of the simulated glow curves were in the same temperature range as the measured glow peak 2 of LiF:Mg,Ti (TLD-100). The parameters in cases (I.e) through (I.h) where chosen in such way that the defect reaction was dominant over the trap emptying process. The goal of the simulations with these parameters and those of case (II.a) through (II.c) is to show that one can obtain glow curves with high s values ($\sim 10^{19}$ s^{-1}) when fitted according to the RW model, while the frequency factors of all processes described in Eq. (2.9) and Eq. (2.10) are on the order of 10^{10}-10^{13} s^{-1}. The parameters in case (III) are chosen such that two glow peaks occur. The RW parameters obtained by fitting the simulated curves to the RW model are shown in Table 2.3

Figure 2.2 shows three glow curves simulated according to case (I). The parameters are chosen from the parameter set (I.a), (I.b) and (I.c) from Table 2.2 For the simulation a heating rate of 3 K s^{-1} has been assumed. The glow curves differ in the rate of the reaction $A^* + B \rightarrow C$ (see Table 2.2). When the reaction rate is increased the peak area decreases and the peak maximum shifts to lower temperatures. The data points obtained by the simulations are considered as experimental measured data and fitted according to the RW model. The FOM for the three fits are (a): 0.02 %, (b): 0.37 % and (c): 1.6 %. These low values indicate that the fits are very good.

Table 2.2 Parameters used in simulations according to the ID model.

Case	$n_{A^*}(t=0)$	E_a	s_a	E_b	$n_B s_b$	$n_{C^*}(t=0)$	E_k	s_k
	(arb)[a]	(eV)	(s^{-1})	(eV)	(s^{-1})	(arb)[a]	(eV)	(s^{-1})
$A^* + B \rightarrow C^*$								
(I.a)	10^5	1.36	4.3×10^{16}	0.414	148	0	∞	0
(I.b)	10^5	1.36	4.3×10^{16}	0.414	1.3×10^4	0	∞	0
(I.c)	10^5	1.36	4.3×10^{16}	0.414	4.4×10^4	0	∞	0
(I.d)	14.5	1.36	4.3×10^{16}	0.414	5.5×10^3	0	∞	0
(I.e)	10^{10}	1.25	1.07×10^{13}	0.9	7.2×10^{10}	0	∞	0
(I.f)	10^{10}	1.50	1.07×10^{13}	0.9	7.2×10^{10}	0	∞	0
(I.g)	10^{10}	1.75	1.07×10^{13}	0.9	7.2×10^{10}	0	∞	0
(I.h)	10^{10}	2.00	1.07×10^{13}	0.9	7.2×10^{10}	0	∞	0
$C^* \rightarrow A^* + B$								
(II.a)	0	1.25	1.45×10^{12}	∞	0	10^5	1.25	1.07×10^{13}
(II.b)	0	1.25	1.07×10^{13}	∞	0	10^5	1.25	1.07×10^{13}
(II.c)	0	1.25	7.90×10^{13}	∞	0	10^5	1.25	1.07×10^{13}
$A^* + B \rightleftharpoons C^*$								
(III.a)	10	1.36	4.3×10^{16}	0.414	3.0×10^3	0	0.62	3.3×10^6
(III.b)	10	1.36	4.3×10^{16}	0.414	8.1×10^3	0	0.62	3.3×10^6
(III.c)	10	1.36	4.3×10^{16}	0.414	2.2×10^4	0	0.62	3.3×10^6

[a] Concentration at t=0 in arbitrary units.

Table 2.3 Effective Randall-Wilkins parameters obtained by fitting the simulated glow curves. The glow curves are obtained by simulations according to the ID model. The parameters used for the simulation are shown in Table 2.2.

Case	$n_1(t=0)$ (arb.)[a]	E_1 (eV)	s_1 (s^{-1})	$n_2(t=0)$ (arb.)[a]	E_2 (eV)	s_2 (s^{-1})	FOM (%)
(I.a)	9.90×10^{4}	1.36	4.0×10^{16}				0.02
(I.b)	5.12×10^{4}	1.24	1.8×10^{15}				0.37
(I.c)	1.38×10^{4}	1.05	8.4×10^{12}				1.6
(I.e)	4.36×10^{7}	1.38	8.4×10^{14}				3.1
(I.f)	2.79×10^{4}	1.52	2.8×10^{16}				4.5
(I.g)	18.8	1.65	7.0×10^{17}				5.5
(I.h)	1.32×10^{-2}	1.77	1.4×10^{19}				6.4
(II.a)	10^{5}	1.34	1.18×10^{13}				6.3
(II.b)	10^{5}	1.79	6.38×10^{18}				7.0
(II.c)	10^{5}	1.62	3.51×10^{17}				8.8
(III.a)	8.5	1.34	2.4×10^{16}	1.5	0.93	3.7×10^{10}	1.0
(III.b)	6.6	1.30	7.6×10^{15}	3.4	0.92	2.7×10^{10}	2.2
(III.c)	3.5	1.17	1.1×10^{14}	6.6	0.91	2.0×10^{10}	3.2

[a] Concentration at t=0 in arbitrary units.

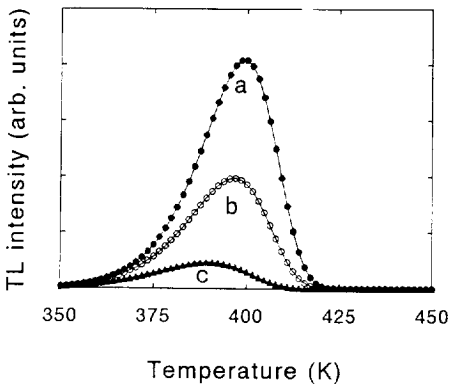

Fig. 2.2 Fits of simulated glow curves according to case (I) of the ID model. The simulated glow curves a (•), b (O), and c (▲) are according to case (I.a), (I.b) and (I.c) of Table 2.2 respectively at a heating rate of 3 K s^{-1}. In these cases trap A^* is simultaneously involved in a trap emptying process $A^* \rightarrow A + e$ which leads to light production [(a) in Table 2.1] and a defect reaction $A^* + B \rightarrow C^*$ [(b) in Table 2.1]. The simulated glow curves have been considered as experimental measured data and fitted according to the Randall-Wilkins model (lines). The fitting parameters are shown in Table 2.3. It is seen that for the cases in question the glow curves according to the ID model can be perfectly fitted by the RW model.

The parameter set (I.d) of Table 2.2 is used to simulate glow curves at different heating rates. The glow curves obtained by the simulations were again considered as experimental measured data and analyzed according to the RW model. For all used heating rates the RW model appeared to describe again very well the glow curves simulated with the Interactive Defect (ID) model. However, the analyses yield that the (effective) RW parameters E, s, and $n(t=0)$ differ for different heating rates (see lines in Fig. 2.3). It is seen that the peak area of the simulated glow curves (Fig. 2.3.a) increases with heating rate. This is because the traps A^* have more time to react with B at low temperature (where the defect reaction is dominant) at low heating rates than at high heating rates. So at high heating rates there are more traps available in the trap emptying process than at low heating rates. The (effective) RW parameters E and s also increase with increasing temperature (Fig. 2.3.b and Fig. 2.3.c). The dots in Fig. 2.3 are fitted RW parameters obtained by a fit of the so-called peak 2 of LiF:Mg,Ti (TLD-100)

(the data is obtained from Bos and Piters 1993a). They are shown to illustrate that the expected changes in the RW parameters according to the ID model (lines) are comparable with changes in the RW parameters of measured glow curves (dots). Although the simulated data do not precisely match the measured data, the trends are clearly the same.

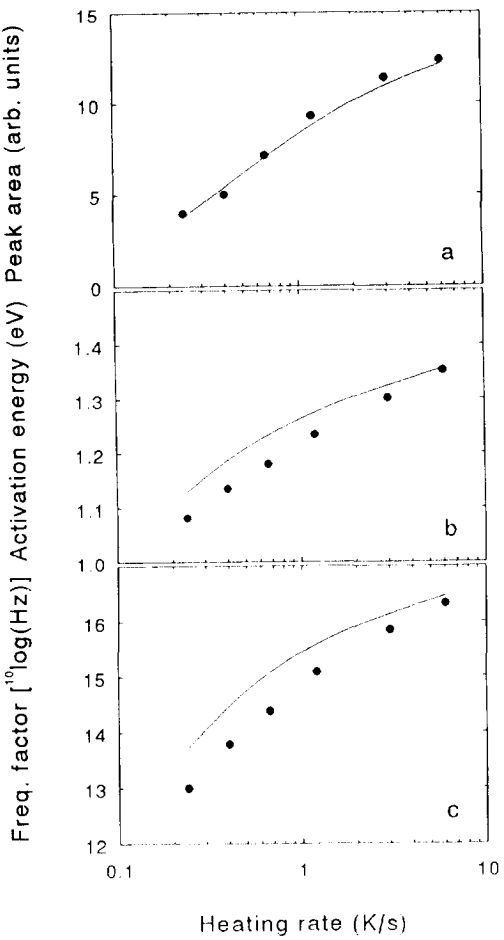

Fig. 2.3 RW parameters peak area (a), activation energy (b) and frequency factor (c) as function of the heating rate. The lines are obtained as follows. Firstly, glow curves were simulated according to case (I.d) of the ID model (see Table 2.2) at different heating rates. Next these curves were considered as experimental measured data and analyzed according to the RW model. The parameters obtained by this fitting procedure are plotted as lines. In case (I.d) of the ID model, the trap A^* is simultaneously involved in a trap emptying process $A^* \rightarrow A + e$ which leads to light production [(a) in Table 2.1] and a defect reaction $A^* + B \rightarrow C^*$ [(b) in Table 2.1]. The (•) points are the RW parameters of the measured glow peak 2 of LiF:Mg,Ti (TLD-100) at different heating rates (after Bos and Piters 1993a). The annealing procedure of the LiF:Mg,Ti (TLD-100) samples involved 1 hour at 673 K followed by a quick cooling down to room temperature.

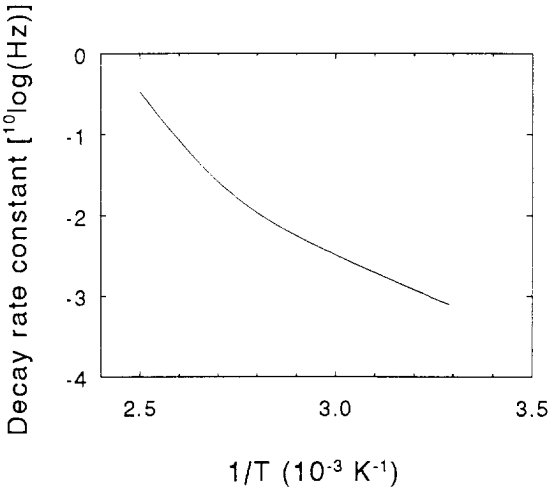

Fig. 2.4 The ^{10}log of the decay rate constant versus $1/T$ for case (I.d) of the ID model (see Table 2.2). The decay rate constant is equal to $\lambda_d = s_a \exp(-E_a/kT) + n_B s_b \exp(-E_b/kT)$. It is seen that for the case in question this plot does not yield a straight line.

The parameter set (I.d) is also used to determine the behaviour of the isothermal decay rate constant as function of the temperature. The decay rate constant λ_d is defined as:

$$\frac{dI_{TL}}{dt} = -\lambda_d I_{TL} \tag{2.14}$$

When the temperature is kept constant the derivative of I_{TL} can be derived from Eq. (2.7):

$$\frac{dI_{TL}}{dt} = -I_{TL}\left(s_a \exp(-E_a/kT) + n_B s_b \exp(-E_b/kT)\right) \tag{2.15}$$

So the factor $[s_a \exp(-E_a/kT) + n_B s_b \exp(-E_b/kT)]$ is the decay rate constant for isothermal decay according to the ID model. With the parameters used for the simulations in Fig. 2.3, (I.d), the isothermal decay rate constant is calculated at different temperatures. Figure 2.4 shows the logarithm of the decay rate constant

as function of $1/T$. The plot shows a curved line, while according to the RW model the plot would show a straight line. At the high temperature region the decay is mainly determined by the trap emptying process while at the low temperature region the decay is mainly determined by the defect reaction $A^* + B \rightarrow C^*$. Under experimental conditions the temperature region of decay rate measurements is usually smaller than shown in Fig. 2.4. Therefore the bend in the curve may be easily overlooked. When the logarithm of the decay rate constant in a small temperature region is assumed to be linear dependent on $1/T$, then the RW parameters E and s could be determined from the slope and the intersection with the $^{10}\log(\lambda_d)$ axis at $T \rightarrow \infty$. However, the RW parameters determined in this way are dependent on the position of the temperature region. The decay rate constant at room temperature (293 K) for the simulated process (I.d) is 4.2×10^{-4} s^{-1}. This is much faster than expected from the RW parameters found at a heating rate of 3 K s^{-1} (1.9×10^{-7} s^{-1}). A similar discrepancy can be observed for the fading rate of peak 2 of LiF:Mg,Ti(TLD-100). For this peak the measured decay rate at room temperature is 10^{-5} s^{-1} while the value calculated with the RW parameters obtained by glow curve analyses at a heating rate of 3 K s^{-1} come to 3×10^{-7} s^{-1} (Bos and Piters 1993b).

Figure 2.5 shows four simulations of case (I) with extreme parameter values such that $\alpha_b >> \alpha_a$. The parameters are from the sets (I.e), (I.f), (I.g) and (I.h). Fits according to the RW model yield FOM values between 3.1 % and 6.4 %. From Table 2.2 and Table 2.3 it is seen that for these choices of parameters in the simulation, the RW parameter s is much larger than s_a and s_b. The parameter s increases with increasing E_a. The RW parameter E lies between E_a and E_b. The fitted peak area $n(t=0)$ is much less than $n_{A^*}(t=0)$ and decreases with increasing E_a.

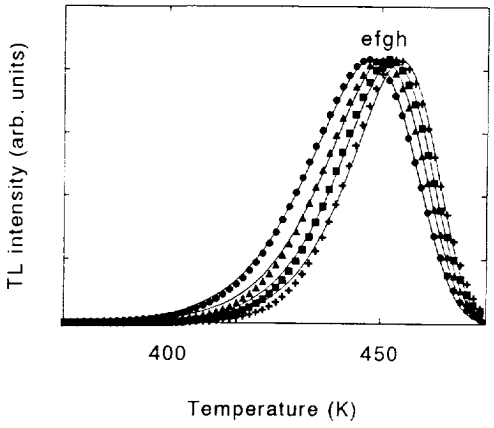

Fig. 2.5 Fits of simulated glow curves according to case (**I**) of the ID model for some extreme cases. Simulated glow curves e (●), f (▲), g (■), and h (+) are obtained for cases (**I**.e), (**I**.f), (**I**.g) and (**I**.h) of Table 2.2 respectively at a heating rate of 3 K s^{-1}. In these cases trap A^* is simultaneously involved in the trap emptying process [(a) in Table 2.1] and in a defect reaction $A^*+B \rightarrow C^*$ [(b) in Table 2.1]. The reaction rate $\alpha_b = n_{A^*} n_B s_b \exp(-E_b/kT)$ is much higher than the emptying rate $\alpha_a = n_{A^*} s_a \exp(-E_a/kT)$. The simulated glow curves are considered as experimental measured data and fitted according to the RW model (lines). Each curve is normalized. The fitting parameters are shown in Table 2.3.

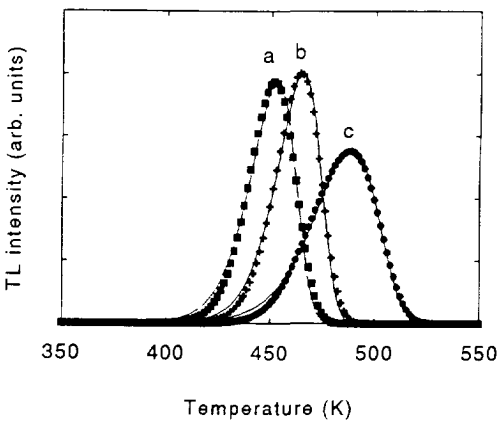

Fig. 2.6 Fits of simulated glow curves according to case (**II**) of the ID model. The simulated glow curves a (■), b (+) and c(●) are obtained by cases (**II**.a), (**II**.b) and (**II**.c) of Table 2.2 respectively at a heating rate of 3 K s^{-1}. In these cases the trap C^* dissociates to A^* and B: $C^* \rightarrow A^* + B$ [(k) in Table 2.1]. Simultaneously, trap A^* is involved in the trap emptying process $A^* \rightarrow A + e$ which leads to light production [(a) in Table 2.1]. The simulated glow curves are considered as experimental measured data and fitted according to the Randall-Wilkins model (lines). The fitting parameters are shown in Table 2.3.

Figure 2.6 shows three simulations of case (II). At t = 0 all trapped charge carriers are trapped by defect C. The defects C do not empty but are involved in a dissociation process $C^* \rightarrow A^* + B$. The defect A^* empties which leads to light production. The data points obtained by the simulations are fitted with the RW model. The fits diverge from the simulated curves at the low temperature side of the glow peaks and the FOM values are rather high (between 6.3 % and 8.8 %). It is seen that the value of the RW parameter s is much higher than s_a or $n_B s_b$ if the reaction rate of the dissociation process of C^* is equal to the reaction rate of the emptying process of A^* (case II.b).

Figure 2.7 shows some simulations of case (III). The simulations were fitted with two glow peaks according to the RW model. Fits were reasonable but less good than the fits of Fig. 2.2. FOM values are (a): 1 %, (b): 2.2 % and (c): 3.2 %.

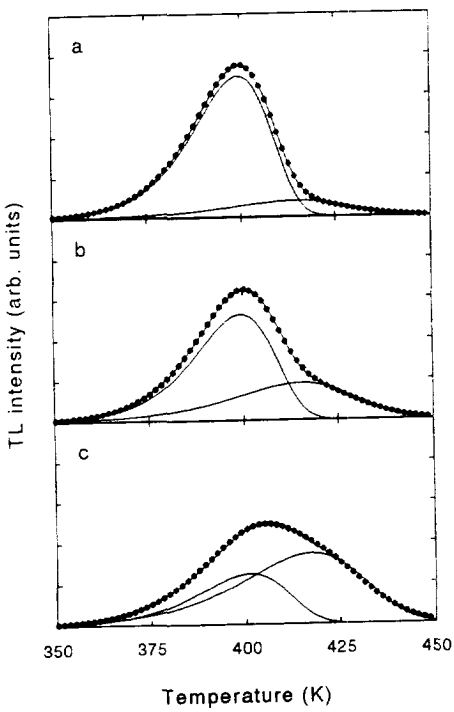

Fig. 2.7 Fits of simulated glow curves according to case (III) of the ID model. The simulated glow curves (dots) a, b and c are obtained by case (III.a), (III.b) and (III.c) of Table 2.2 respectively at a heating rate of 3 K s^{-1}. In these cases the trap responsible for TL, A^* is simultaneous involved in the emptying process [(a) in Table 2.1], the defect reaction $A^* + B \rightarrow C^*$ [(b) in Table 2.1] and the reverse reaction $C^* \rightarrow A^* + B$ [(k) in Table 2.1]. The simulated glow curves are considered as experimental measured data and fitted according to the Randall-Wilkins model with two glow peaks (lines). The fitting parameters of these two glow peaks are shown in Table 2.3.

2.4 Discussion and conclusions

The cases of the ID model used for the simulations in this chapter are very simple and account only for one or two defect reactions. In real solids like LiF:Mg,Ti (TLD-100) the number of reactions that influences the thermoluminescence is probably higher. Nevertheless the simple cases of the ID model described in this chapter show that the occurrence of defect reactions during read out may explain the following observations of thermoluminescence which cannot be explained by the RW model.

(1) The dependence of E and s on the annealing procedure and impurity concentration.

Both a change in the annealing procedure and impurity concentration will change the defect concentration (in particular n_B). The rate of the reaction in which the trap is involved, is proportional to the defect concentrations of all involving defects. So a change in the concentration of the defects means a change in the rate of the defect reactions and this influences the shape of the glow peak. If the glow peak is still fitted according to the RW model the fitting parameters will show a dependence on annealing procedure and impurity concentration. Simulations with parameters (I.a) to (I.c) from Table 2.2 show that the (effective) RW parameters E and s increase with decreasing n_B (Table 2.3 case I.a, I.b and I.c).

(2) The dependence of peak area, E and s on heating rate.

The glow curves of LiF:Mg,Ti (TLD-100) can be fitted very well with the RW model. However, the RW parameters depend on the heating rate during read out. For example The RW parameters of peak 2 increase with increasing heating rate (see dots in Fig. 2.3). With the ID model (case (I.d)) it is possible to produce glow curves that can be fitted very well with the RW model and of which the effective RW parameters increase with heating rate (lines in Fig. 2.3) in a similar way as those of peak 2.

(3) High fading rates.

The occurrence of defect reactions as in case (I.d) explains why fading rates are higher than expected from the RW parameters and why isothermal decay

experiments lead to different values of the RW parameters.

(4) High *s* values

We found two explanations for the unexpected high *s* values of peak 5 in TLD-100. The first explanation is that the corresponding trap is involved in a very fast reaction (compared with the rate of the trap emptying) which decreases the concentration of the traps very rapidly [case (I.e)..(I.h)]. In these cases the number of trapped charge carriers that produce TL is about 10^{-9} - 10^{-12} times the number of trapped charge carriers initially present. This means that the TL efficiency would be smaller than 10^{-9}. This is much smaller than measured in LiF:Mg,Ti (TLD-100) (η = $4x10^{-4}$ Attix 1986 p. 400). Therefore this explanation for the high *s* value is unrealistic.

The other explanation is that the trap itself does not empty. Instead it is involved in a dissociation process in which one of the dissociation products is an unstable trap. [case (II.a)..(II.c)]. The rate of the emptying process of the unstable trap is more or less equal to the reaction rate of the dissociation. In this case all trapped charge carriers lead to TL. However, the shape of the glow curve according to this model shows some aberrations from the RW model. It is necessary to assume that the emptying rate and dissociating rate are more or less equal. A mechanism for peak 5 of LiF:Mg,Ti (TLD-100) that is described by such a reaction has been proposed by McKeever (1985, p. 112). He suggested that peak 5 is the result of the dissociation of a $(Mg\text{-}V)_3^*$ trimer into two Mg-V dipoles and a Mg-V dipole plus a trapped charge (associated with peak 2). The trapped charge at the Mg-V dipole is immediately released to the conduction band at the dissociation temperature. However, our findings suggest that this mechanism would not lead to high *s* values because the trap emptying process of the Mg-V dipoles (peak 2) at the temperature region of peak 5 is much faster than the dissociation process. The RW parameters *s* and *E* obtained by glow curve fitting would be of the parameters of the dissociation process [case II with condition $s_a\exp(-E_a/kT) >> s_k\exp(-E_k/kT)$]. A slightly different mechanism may be that the $(Mg\text{-}V)_3^*$ trimer dissociates into a Mg-V dipole and a $(Mg\text{-}V)_2^*$ dimer. If we assume that the latter trap is more stable than the $(Mg\text{-}V)^*$ trap so that the rate of the emptying process is on the same order as the dissociation rate, a high *s* value can be expected.

Inherent to the ID model is that it needs more parameters than the RW model. This could be a problem when the ID model is applied to a fitting procedure on glow peaks because single glow peaks are already very well

described by just three parameters (RW model). Adding more parameters to the description of the glow peaks results into a loss of sensitivity and consequently a less accurate determination of the parameters. A solution for this problem is fitting simultaneously more glow curves measured under different experimental conditions.

Another problem concerns the required calculation time for solving the differential equations numerically. As the number of differential equations increases, the calculations become very time consuming which is especially a problem with fitting. It has been shown that in some cases the set of differential equations can be reduced to one differential equation (Kantorovich *et al* 1990). Further investigation into methods of solving huge set of differential equations could perhaps lead to efficient calculation methods.

In spite of the difficulties in experimental verification of the ID model we think that the ID model shows some promising possibilities to explain some serious problems of thermoluminescence in TLD-100 that cannot be explained by the RW model. Developments in fitting procedures (simultaneous fits of glow curves measured under different experimental conditions) and calculation methods for huge sets of differential equations could help to get a better experimental verification of the ID model.

Chapter 3

A simple model for the shape of emission bands

Abstract: In this chapter the shape of a TL emission band is described according to a simple model. In this model the lattice vibrations are classically treated and the electronic transitions are assumed to be instantaneously (Franck-Condon principle). According to this model the shape of the emission spectrum (number of emitted photons per unit photon energy) can be described by a Gauss function of photon energy. The central emission energy is temperature independent and the width is proportionally to the square root of the absolute temperature T. This temperature dependence of the width of the emission spectrum is equal to the high temperature limit of more advanced models of the shape of the emission spectrum in which the width of the emission band is proportional to the square root of $\hbar\omega\coth(\hbar\omega/2kT)$. A relationship between the shape of the emission spectrum and the decrease of the luminescence efficiency due to quenching is deduced. It appears that due to quenching the luminescence efficiency of broad emission bands is less than that of narrow bands.

3.1 Introduction

The TL emission spectra of thermoluminescent materials like LiF:Mg,Ti and CaF_2:Tm show some prominent emission bands of which the intensity is temperature dependent. Studying the behaviour of these emission bands may give some information about the mechanism of thermoluminescence in these materials (Townsend and Kirsh 1989). However, emission bands are often overlapping so it becomes difficult to investigate the behaviour of these bands separately. Computational methods may be used to separate the overlapping bands. For such methods there is a need for a good description of the shape of the emission band. It is the purpose of this chapter to fill in this need. The models for emission (and absorption) spectra of luminescent centres in solids originate from the theory of molecule spectra. Although there are very extended and sophisticated models for emission in solids available (Lax 1952), we developed a

very simple model based on a classical treatment of the lattice vibrations and the Franck-Condon principle. This makes a brief but complete description of the derivation possible. The treated model provides us not only with a band shape necessary to separate emission bands but also with some insight into the formation of emission bands. Furthermore, a relationship between the decrease of the efficiency of TL production with increasing temperature (quenching) and the shape of the emission band can be deduced from the model.

3.2 Configuration diagram of the luminescent centre

The band model for thermoluminescence is usually represented as in Fig. 1.1 of chapter 1. In this chapter the recombination step [transition (5) and transition (6) in Fig. 1.1 of chapter 1] is treated in more detail.

The recombination step is thought of as a two step process. In the first step [transition (5)] the electron is localized around the recombination centre due to the relaxation of the lattice around the luminescent centre when the electron approaches the centre. This relaxation of the lattice occurs at a rate of approximately 10^{13} s^{-1} (Debye frequency). During this step no photons are emitted. After this step the luminescent centre is still in an excited state.

The second step [transition (6)] is an electronic transition from the excited state to the ground state. This step occurs at a rate of approximately 10^{8} s^{-1} (Mahesh *et al* 1989) and is the cause of the light emission.

The potential energy of the excited state and the ground state of the luminescent centre is influenced by the configuration of the lattice around the luminescent centre. The configuration vibrates around an equilibrium configuration and can be represented by a set of configuration coordinates. Figure 3.1 shows two examples of a configuration vibrating in one dimension. In these examples the configuration can be described by one configuration coordinate: the distance between the nearest neighbours of the luminescent centre. The equilibrium configuration of the excited state is different from that of the ground state, because of a strong electron-lattice interaction. In a so-called *configuration diagram* of Fig. 3.2, the potential energy of the excited and ground state are expressed as function of the configuration coordinate. The horizontal lines drawn in Fig. 3.2 represent the total energy levels of the luminescent centre, *i.e.* the electronic excitation energy E_e plus the vibration energy E_v.

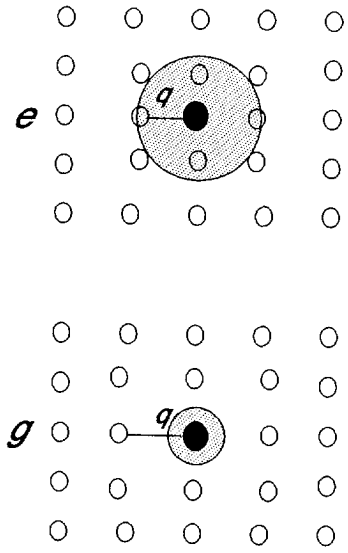

Fig. 3.1 Examples of a configuration of a luminescent centre in the excited state (e) and in the ground state (g). The extensiveness of the electron wave function is represented by the shaded area. The difference in configuration of the excited and ground state is caused by the electron-lattice interaction. The distance between the luminescent centre and its nearest neighbour q is used to characterise the configuration. The coordinate q is called the configuration coordinate.

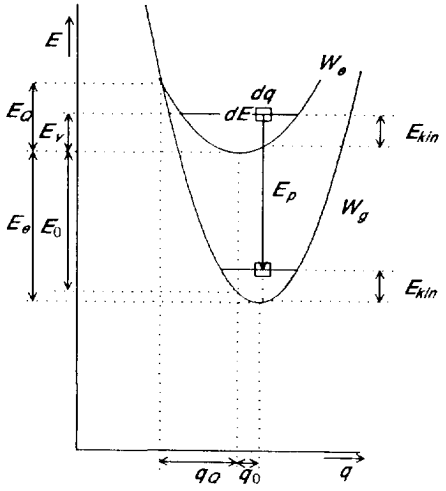

Fig. 3.2 Configuration diagram of the luminescent centre with potential energy curves as function of the configuration coordinate q for the excited state (W_e) and ground state (W_g). The minimum of the potential curve of the excited state is shifted over a distance q_0 with respect to the ground state. The difference in energy of the minimum of both curves is the excitation energy E_e. The horizontal lines represent energy levels of the luminescent centre. The vertical arrow represents a transition between excited and ground state with photon energy E_p. During the transition the kinetic energy E_{kin} is preserved. E_v is the vibration energy, E_0 the central photon energy of the emission band. At configuration q_Q and vibration energy E_Q the potential curves intersect. At this point a non radiative transition is possible.

3.3 Transitions

The vibrating configuration of a luminescent centre, is treated as a classical harmonic oscillator. For a harmonic oscillator the potential energy of the excited state W_e and the ground state W_g are quadratic with the configuration coordinate q:

$$\begin{aligned} W_e(q) &= C_e q^2 + E_e \\ W_g(q) &= C_g (q-q_0)^2 \end{aligned} \tag{3.1}$$

where C_e is related to the force constant F_e in the excited state ($2C_e = F_e$), C_g related to the force constant F_g in the ground state ($2C_g = F_g$), E_e the excitation energy and q_0 the displacement of the equilibrium. Transitions from the excited to the ground state are assumed to be instantaneous. This means (1) the configuration coordinate does not change during the transition and (2) the impulse or kinetic energy of the configuration does not change during the transition (this is the classical interpretation of the Franck-Condon principle). In the configuration diagram the possible transitions can be represented as vertical lines from a vibration level in the excited state to a vibration level in the ground state (see Fig. 3.2). There are two possible types of transitions between the excited and ground state: radiative and non-radiative.

During a radiative transition the energy difference between excited and ground state is released by a photon. The photon energy is equal to the energy difference. The probability of a radiative transition per unit time is assumed to be independent of the configuration and the vibration energy.

During the non-radiative transition the energy is released by heat. This means that vibration energy of the luminescent centre is transferred to the lattice. The luminescent centre is in thermal equilibrium with the lattice and only small amounts of energy (on the order of kT = 0.05 eV at 580 K) can be transmitted. Therefore non-radiative transitions only occur at configurations where the potential energy difference between excited and ground state is small *i.e.* in the surroundings of the intersection of the two potential energy curves. The rate of transition between vibration levels of one state is assumed to be much higher than that of the transitions between excited and ground state. With this assumption, the distribution of the vibration levels is that of equilibrium.

3.4 Shape of the emission band for one dimension

In this section the vibration of the luminescent centre is considered to be in one dimension. In section 3.5 it is shown that in case of a vibration in more dimensions, the derivation of the shape of the emission spectrum is similar to that of an one dimensional vibration.

The shape of the emission band is determined by the distribution of the number of photons with different photon energies E_p. The number of emitted photons with an energy between E_p and $E_p + dE_p$ is proportional to the probability $a(E_p)dE_p$ of photon emission as function of the photon energy between E_p and $E_p + dE_p$. This is the sum of all probabilities of transition by which a photon with an energy between E_p and $E_p + dE_p$ is emitted. So to obtain $a(E_p)dE$ we have to find firstly all transitions [from (E,q) to $(E - E_{photon}, q)$] with a photon energy between E_p and $E_p + dE_p$ and secondly the probabilities $P(E,q)dEdq$ of these transitions.

One group of transitions with the same photon energy is the group of all transitions occurring at the same configuration coordinate. This can be understood as follows. The change in the total energy of the luminescent centre during a transition is the same as the change in the potential energy, because the kinetic energy does not change during the transition. The potential energy does only depend on the configuration coordinate and not on the energy of the vibration level. So all transitions at the same configuration coordinate change the energy with the same amount.

To find all coordinates with the same photon energy during a transition, the difference between the potential energy of the excited and ground state must be determined. Because the potential energies of both states are quadratic functions of the configuration coordinate, the difference between the potential energies is also a quadratic function:

$$E_p = W_e - W_g = (C_e - C_g)q^2 + 2C_g q_0 q + E_0 \qquad (3.2)$$

where $E_0 = E_e - C_g q_0^2$. For simplicity we assume that $C_e = C_g = C$. Then Eq. (3.2) becomes:

$$E_p = 2Cq_0 q + E_0 \qquad (3.3)$$

For a transition with a certain photon energy there is just one unique

configuration coordinate:

$$q = \frac{E_p - E_0}{2Cq_0} \tag{3.4}$$

So the sum of all probabilities of transition with photon energy E_p is the integral over all vibration levels at a certain coordinate:

$$a(E_p)dE_p = \int_{E=W_e(q)}^{\infty} P(E,q)dE\,dq \tag{3.5}$$

where $P(E,q)dEdq$ is the probability of finding the configuration in the interval $dqdE$ at coordinate q and energy level E.

The next task is to calculate the probability $P(E,q)$. The calculations can be split into two parts. Firstly, we calculate the probability $P(E)$ of finding the luminescent centre at a certain vibration level. Secondly, we calculate the probability $P(E,q)\,|_E$ of finding the luminescent centre at a certain configuration coordinate when the vibration level is fixed at a specified energy E. The product of these two probabilities is the desired probability $P(E,q)$.

For the first part of the calculation we assume Bolzmann statistics. Then the probability of finding the luminescent centre in an energy interval dE at a vibration level E is equal to:

$$P(E)dE = \frac{\exp(-E/kT)}{\int_{E_e}^{\infty} \exp(-E/kT)\,dE}\,dE \tag{3.6}$$

The second part of the calculation is based on the theory of the harmonic oscillator. Let T_p be the time required for one period of the oscillation cycle. The probability of finding the configuration between q and $q + dq$ is equal to the time the configuration is in this interval during one cycle divided by T_p:

$$P(E,q)\,|_E\,dq = \frac{dt}{T_p} \tag{3.7}$$

The time dt that the configuration is in the interval dq is equal to the number of times the configuration passes q (2 times) times the length of the interval dq

divided by the absolute value of the velocity v of the configuration in q:

$$dt = \frac{2\,dq}{v\,(q,E)} \tag{3.8}$$

For a harmonic oscillator:

$$\begin{aligned} q(E,t) &= \sqrt{\frac{E_v}{\omega_e^2 m}}\,\sin(\omega_e t) \\ \frac{dq}{dt} &= \sqrt{\frac{E_v}{m}}\,\cos(\omega_e t) \\ T_p &= \frac{2\pi}{\omega_e} \end{aligned} \tag{3.9}$$

where $\omega_e = \sqrt{(C_e/m)}$, E_v the vibration energy: $E_v = E - E_e$ and m the effective mass of the configuration. Substituting Eq. (3.8) and Eq. (3.9) into Eq. (3.7) gives:

$$P(E,q)\,|_E\,dq = \frac{dq}{\pi\sqrt{\frac{E_v}{C_e} - q^2}} \tag{3.10}$$

Multiplying $P(E,q)\,|_E$ with $P(E)$ gives:

$$P(E,q) = \frac{\exp\left(-\frac{E}{kT}\right)}{\pi\sqrt{\frac{E_v}{C_e} - q^2}\int_{E_e}^{\infty}\exp\left(-\frac{E}{kT}\right)dE} \tag{3.11}$$

The shape of the emission band can be determined by integrating $P(E,q)$ over all energy levels [see Eq. (3.5)]. The details about the calculation can be found in

Appendix A. The result of the integration appears to be a Gauss function of q:

$$a(E_p)dE_p = \sqrt{\frac{C}{\pi kT}} \exp\left(-\frac{q^2 C}{2kT}\right) dq \tag{3.12}$$

From Eq. (3.4) it follows that:

$$dq = \frac{1}{2Cq_0} dE_p \tag{3.13}$$

substituting Eq. (3.13) and Eq. (3.4) into Eq. (3.12) gives:

$$a(E_p) = \frac{1}{U\sqrt{2\pi}} \exp\left[-\frac{(E_p - E_0)^2}{2U^2}\right] \tag{3.14}$$

where:

$$\begin{aligned} E_0 &= E_e - C q_0^2 \\ U^2 &= 2 C q_0^2 kT \end{aligned} \tag{3.15}$$

The shape of the emission band is described by just two parameters *i.e.* E_0 and Cq_0^2. The parameter E_0 specifies the position of the emission band and the parameter Cq_0^2 is an indication for the width of the emission band.

At this point it is useful to compare this result with the shape of the emission band used by other authors (Fairchild *et al* 1978, Jacobs and Menon 1971). Their expression for the shape of the emission band is based on a model that treated the vibrations of the excited and ground state quantum mechanically. They used the same expression as Eq. (3.14) but with:

$$\begin{aligned} E_0 &= C_1 - C_2 \coth\left(\frac{\hbar\omega}{2kT}\right) \\ U^2 &= S(\hbar\omega)^2 \coth\left(\frac{\hbar\omega}{2kT}\right) \end{aligned} \tag{3.16}$$

where C_1 and C_2 are constants, $\hbar\omega/2\pi$ is the effective vibration frequency and S is the Huang-Rhys factor. So for the description of the emission band according to Eq. (3.14) and Eq. (3.16) one needs four parameters *i.e.* C_1, C_2, ω and S. In the case $C_2 = 0$ and $kT >> \hbar\omega$, then Eq. (3.16) approaches Eq. (3.15). In that case

C_1 could be identified with E_0 and $\hbar\omega S$ with Cq_0^2.

In practice the emission band is usually measured as the emitted energy $I(\lambda)$ as function of wavelength. The correct expression for $I(\lambda)$ can be found by the equivalence between the emitted power over a small wavelength interval $\Delta\lambda$ calculated with $I(\lambda)$ and with $a(E)$:

$$I(\lambda)\,|\Delta\lambda| \;=\; N\,a(E)\,E\,|\Delta E\,| \tag{3.17}$$

where N is the total number of emitted photons. E and ΔE correspond to λ and $\Delta\lambda$ according to:

$$\begin{aligned} E &= \frac{hc}{\lambda} \\ |\Delta E| &= \left|\frac{dE}{d\lambda}\Delta\lambda\right| = \left|\frac{hc}{\lambda^2}\Delta\lambda\right| \end{aligned} \tag{3.18}$$

Substituting Eq. (3.18) and Eq. (3.14) into Eq. (3.17) results into:

$$I(\lambda) \;=\; \frac{h^2c^2}{\lambda^3}\frac{A}{U\sqrt{2\pi}}\exp\left[-\frac{(hc/\lambda - E_0)^2}{2U^2}\right] \tag{3.19}$$

The broadening of the emission spectrum caused by the difference between the configuration in the excited and ground state as treated in this chapter is in the range of $U \approx 0.01$ eV to 1 eV (*e.g.* T = 450 K, Cq_0^2 = 3 eV $\Rightarrow$ U = 0.48 eV). This broadening is very large compared to other broadening mechanisms in nature [*e.g.* the natural line width for most transitions is on the order of 0.5 μeV (Wichmann 1971) and the Doppler broadening in hot gas (1000 K hydrogen 2S → 1S) is on the order of 0.2 meV].

3.5 Vibrations in more dimensions

In this section it is shown that the result obtained in section 3.4 for vibrations in one dimension is also valid for vibrations in more dimensions if we assume that all vibrational modes are harmonic oscillators and the force constants are not

influenced by excitation. The potentials of the excited and the ground state are:

$$W_e(q_1.....q_N) = \sum_{i=1}^{N} C_i q_i^2 + E_e$$
$$W_g(q_1.....q_N) = \sum_{i=1}^{N} C_i(q_i - q_{0i})^2 \qquad (3.20)$$

It is always possible to rotate the basis $(q_1....q_N)$ to a new basis $(p_1....p_N)$ such that p_1 is in the direction of the shift $\vec{q}_0 = (q_{01}....q_{0N})$. The summations in Eq. (3.20) can be interpreted as the square of the length of a N-dimensional vector. The length of a vector is invariant under the rotation of the base. So on the new basis Eq. (3.20) can be expressed as:

$$W_e(p_1.....p_N) = D_1 p_1^2 + E_e + \sum_{i=2}^{N} D_i p_i^2$$
$$W_g(p_1.....p_N) = D_1(p_1 - p_0)^2 + \sum_{i=2}^{N} D_i p_i^2 \qquad (3.21)$$

The photon energy is:

$$E_p = W_e - W_g = 2 D_1 p_0 p_1 + E_0 \qquad (3.22)$$

The photon energy E_p depends only on the coordinate p_1. The values of the coordinates $p_{i\neq1}$ have no effect on the emission. Therefore Eq. (3.3) to (3.15) may also be used for the more dimensional case.

3.6 Quenching

Quenching is the phenomenon that the luminescence efficiency decreases as the temperature increases. It is caused by the competition between the non-radiative transition and the radiative transition. A simple formula for the efficiency of luminescence as function of the temperature can be derived from the model for the luminescent centre. Let q_Q be the configuration coordinate where potential and kinetic energies of the excited and ground state are equal (see Fig. 3.2).

According to Eq. (3.4) q_Q is equal to (E_p=0):

$$q_Q = \frac{-E_0}{2Cq_0} \tag{3.23}$$

We assume that the non-radiative transition only occurs in a small area Δq around q_Q for which $|E_p| \leq kT$:

$$\Delta q = \frac{kT}{Cq_0} \tag{3.24}$$

The rate of the non-radiative transition P_{nr} is equal to the attempt-to-transit frequency for non-radiative transitions s_{nr}, times the probability of finding the configuration in Δq:

$$\begin{aligned} P_{nr} &= s_{nr} \sqrt{\frac{C}{\pi kT}} \exp\left(-\frac{C q_Q^2}{kT}\right) \Delta q \\ &= s_{nr} \sqrt{\frac{kT}{2\pi C q_0^2}} \exp\left(-\frac{C q_Q^2}{kT}\right) \end{aligned} \tag{3.25}$$

The rate of a radiative transition P_r is equal to the attempt-to-transit frequency of radiative transitions s_r. The luminescence efficiency η is defined as the fraction of transitions that are radiative:

$$\eta(T) = \frac{P_r}{P_r + P_{nr}} \tag{3.26}$$

Substituting Eq. (3.25) and $P_r = s_r$ in Eq. (3.26) gives:

$$\eta(T) = \frac{s_r}{s_r + s_{nr}\sqrt{kT/(2\pi C q_0^2)}\ \exp(-q_Q^2 C/kT)} = \frac{1}{1 + c(T)\ \exp(-E_Q/kT)} \qquad (3.27)$$

where

$$E_Q = q_Q^2 C = \frac{E_0^2}{4 C q_0^2} \qquad (3.28)$$

$$c(T) = \frac{s_{nr}}{s_r}\sqrt{\frac{kT}{2\pi C q_0^2}}$$

Typical values for s_{nr} and s_r are $s_{nr} \approx 10^{13}$ s^{-1} (Debye frequency) and $s_r \approx 10^8$ (Mahesh *et al* 1989 p 34). From Eq. (3.27) and Eq. (3.28) it is seen that the efficiency η decreases with increasing temperature. For a high value of E_Q the term $c(T)\exp(-E_Q/kT)$ is small and the efficiency is almost 1. The higher E_Q the better the efficiency for luminescence. The parameter E_Q can be determined from the parameters E_0 (the central emission energy) and Cq_0^2 (measure for width of the emission band) that describe the shape of the emission band. From Eq. (3.28) it is seen that the most efficient luminescence is originating from narrow emission bands at high emission energy.

Chapter 4

An automated research facility for measuring thermoluminescence emission spectra†

Abstract: A facility for research into the mechanism of thermoluminescence (TL) is described. The facility comprises three units: an annealing oven, an irradiator and a TL emission spectrometer. Crystals or hot pressed chips can be moved from and to the mentioned units by an automated sample changer. All units operate automatically and are controlled by a personal computer program. The spectrometer is based on a dispersive grating and an intensified diode array (512 active elements) and covers the 200-800 nm wavelength range. The wavelength resolution of the spectrometer is 6 nm when a 25 μm wide entrance slit is used and 29 nm when a 1 mm wide entrance slit is used. The sensitive spectrometer could measure emission spectra of CaF_2:Dy (TLD-200) irradiated at an absorbed dose as low as 3 mGy at a signal to noise ratio of 10:1. For LiF:Mg,Ti (TLD-100) this ratio was obtained at 75 mGy. A detailed description is given how measured data can be related to spectra predicted by a model, taking into account all system aberrations. Spectra of LiF:Mg,Ti (TLD-100) irradiated to an absorbed dose of 5 Gy are analyzed according to the Franck-Condon model for light emission. Two emission bands with peak energies of 3.03 eV and 2.62 eV at 463 K have been found.

4.1 Introduction

Knowledge of the mechanism of thermoluminescence (TL) is of great importance for the development of thermoluminescent materials and thermoluminescent techniques for personal dosimetry. The basic model for the mechanism of thermoluminescence (TL) comprises three steps (McKeever 1985, chapter 1 of this thesis): (1) the trapping of charge carriers during irradiation with ionizing radiation, (2) the release of charge carriers out of traps due to thermal heating

† This chapter is an adapted version of the article "An automated research facility for measuring thermoluminescence emission spectra" (Piters *et al* 1993)

and (3) the capture of charged particles in luminescent centres under photon emission.

An important technique to obtain useful information about the three steps in the TL mechanism is the measurement of the light emission during heating of the sample as a function of temperature and photon energy (TL emission spectrum). However, at absorbed dose levels occurring in personal dosimetry (typically less than 1 mGy), the intensity of the emitted light is so low that an investigation of the emitted light is usually restricted to analysis of the TL emission integrated over all wavelengths (glow curve). In practical personal dosimetry the integrated light intensity is sufficient to determine the absorbed dose. Analysis of the glow curve provides some additional information. However, to study the TL mechanism the information gained from glow curve analysis is limited (Townsend and Kirsh 1989). The information about step (3) is lost and the information about step (2) is disturbed by the fact that the response of the photodetector (usually a photomultiplier tube) is wavelength dependent.

The most widely used TL material for dosimetry is LiF:Mg,Ti. Measurements of emission spectra of this material have been done by Crittenden *et al* (1974), Fairchild *et al* (1978) and Townsend *et al* (1983). However, these measurements were performed at dose levels on the order of 1 kGy. These high dose levels are far from the exposures common in personal dosimetry. It is well-known that the glow curve changes at higher doses [shape of peaks alter and new peaks appear (Jain *et al* 1975)]. Moreover, the intensity of the glow peaks does not vary linearly with increasing dose. Therefore, it is not obvious that the conclusions derived from samples irradiated at high dose levels may be extrapolated to low doses (DeWerd and Stoebe 1972).

In this chapter an automated TL research facility is described. It comprises a very sensitive spectrometer allowing to study the TL mechanism at low dose levels (down to 3 mGy for CaF_2:Dy and 75 mGy for LiF:Mg,Ti). The facility is designed to study the TL of samples after different thermal treatments. With this facility it is possible to study the emission spectra as a function of the annealing or ageing procedure and under different read-out conditions. By way of example, the analysis according to the Franck-Condon model (Fairchild *et al* 1978, Lax 1952) of photon emission of LiF:Mg,Ti measured at different temperatures, is given.

4.2 Design considerations

The facility has been designed considering the research needs of a thermoluminescence dosimetry laboratory. Its primary purpose is to provide the emission spectra of samples used in dosimetry with special interest in LiF:Mg,Ti. The physical form of TL samples appears in loose powder or solid dosemeters (single crystals or hot-pressed multi-crystalline chips). Since the use of loose powder is rare in personal dosimetry (and since handling of this form of sample is very difficult to automatize) the facility has been designed for the solid form of samples.

In earlier experiments (Bos and Piters 1993a, Bos *et al* 1992) in which only two-dimensional glow curves *i.e.* total light intensity versus temperature, were recorded, it was shown that thermal treatments of LiF:Mg,Ti strongly influence the trapping parameters of this material. The facility should, therefore, enable us to do experiments on the samples comprising the four following steps: (1) pre-irradiation thermal treatment, (2) irradiation, (3) post-irradiation thermal treatment and (4) measurement of thermoluminescent emission under heating.

For the thermal treatments an oven was needed in which TL materials could be efficiently and reproducibly heated. The heating profile (i.e. the temperature versus time curve) should be versatile and easily adaptable to suit different thermal treatments. In particular, there was a need to control the cooling rate after the high temperature treatment. A fast cooling rate will freeze in the defect structures as present at high temperatures. Slow cooling rates will allow the defects to cluster and precipitate. A controllable cooling rate (from slow to fast) was therefore a design requirement.

The detection of thermoluminescence emission spectra is a difficult task because the emission is extremely weak in a short period of time. The early used spectrometers (Crittenden *et al* 1974, Fairchild *et al* 1978, Townsend *et al* 1983) were dispersive rapid scanning spectrometers based on a scanning dispersive system (monochromator with a grating or prism) and one detector at the exit of the dispersive system measuring one wavelength interval at a time. The disadvantage of this type of spectrometers is that only a small wavelength interval of the emitted spectrum is measured at one time interval.

During the last decade a number of new sensitive spectrometers based on a charged coupled device (CCD) as detector were successfully employed in TL research (Kanemaki *et al* 1991, Bakas 1984). These spectrometers also use a

dispersive system (in this case a polychromator) but with the scanning mechanism and the detector replaced by a CCD which is actually an array of light detectors. The dispersive system images a whole spectrum on the CCD. The light intensity over the whole array can be measured simultaneously and hence the spectrum is measured over all wavelengths at the same time. Although the principle of detecting all wavelengths simultaneously improves the sensitivity, the CCD is not sensitive in the UV region of the spectrum. Instead of a CCD we used an intensified diode array which has the same advantages as the CCD and is in addition very sensitive in the UV-VIS region (200 nm - 800 nm). The polychromator used was chosen for a high aperture which means a high light throughput. The measurement of the emission spectrum of most TL materials used in TL dosimetry does not require a high wavelength resolution. Therefore, a wide entrance slit can be chosen.

The whole facility is automated for reasons of reproducibility, error reduction and efficiency. The samples can move automatically to different units for thermal treatment, irradiation or readout. To reach maximum efficiency the treatments of the samples in different units are independent and could be executed simultaneously.

Furthermore, the facility has been designed to be easily expanded in the future with other units with other functions.

4.3 Description of the TL research facility

Figure 4.1 shows a schematic overview of the research facility. The centre of the facility consists of a sample changer surrounded by three units: an annealing oven, an irradiator and a reader (TL emission spectrometer). Each unit can be programmed and activated by a main microprocessor. The main microprocessor is connected to a personal computer by a RS-232 connection. Via the personal computer the main microprocessor can be programmed to perform a full experiment. The different parts of the facility are described below.

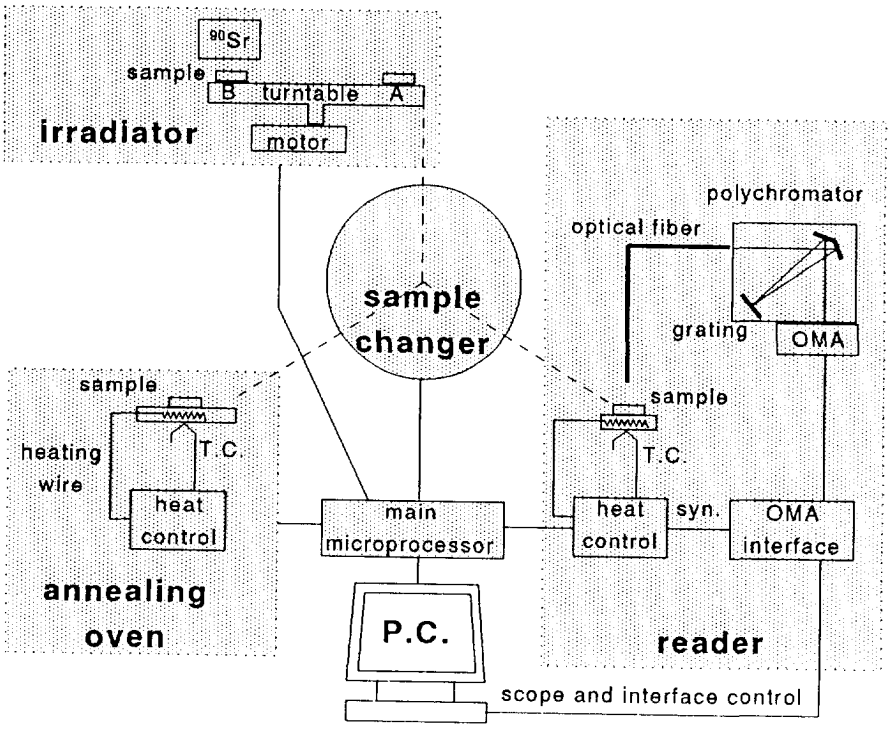

Fig. 4.1 Schematic overview of the research facility. T.C. is a thermocouple, syn. is an interrupt line to synchronize the heating of the sample with the time period of the emission measurement, and OMA is an Optical Multichannel Analyzer.

4.3.1 Sample changer

The sample changer of the facility consists of a robot arm and a storage disk of 30 cm diameter which can contain up to 100 solid samples (crystals or hot-pressed chips) in holes of 4.6 mm diameter situated along the circumference. From the storage disk the samples (typical 3.2 mm x 3.2 mm x 0.9 mm) can be displaced to one of the units by the robot arm. A vacuum probe mounted at the end of the arm is used to pick up and lay down the samples. The storage disk and the robot arm can rotate around the centre of the storage disk independently

of each other with steps of (0.09 ± 0.01) degrees. This corresponds with 0.25 mm on the circumference. The robot arm also can move in radial direction with steps of (0.25 ± 0.03) mm. For these movements three stepping motors are used. The reproducibility of the positioning of the samples was tested by annealing, irradiating and reading out one sample 50 times. After the test no significant change in position was observed.

4.3.2 Irradiator

The irradiator consists of a turntable and a 74 MBq $^{90}Sr/^{90}Y$ source (halflife is 28.5 a). The sample is placed in position A (see Fig. 4.1) on the turntable which rotates the sample to position B under the source. The dose rate in air at position B is 6.36 mGy s^{-1} with a minimal dose of 40.3 mGy (nov 1991). After an adjustable period of time the turntable rotates the sample back to position A.

4.3.3 Annealing oven

The annealing oven of the facility is shown in Fig. 4.2. It can contain up to 16 samples. On top of the oven a sleeve valve has been mounted which can be automatically closed and opened by a piston. The samples are placed on a heating element in the sample chamber. The sample chamber can be filled with nitrogen gas. The heating element is a 3 mm thick cylindrical copper block with a diameter of 30 mm in which a spiral of 1 mm deep is milled out. In this spiral a thermocoax resistance wire is embedded in solder. The block with the wire is covered with a 1 mm gold plate. Gold was used because it is chemical inert at high temperatures and it is easy to braze on the copper block. Moreover, the emissivity of gold is relatively low. The thermocouple is shoved in a hole drilled sideways into the copper block just under the resistance wire. The copper block is mounted on a thin walled inconel cylinder for thermal isolation. The inconel cylinder also separates the sample chamber from the cooling chamber. The cooling chamber is provided with a venturi cooling tube for active cooling with pressured air. To achieve high cooling rates (up to 135 K s^{-1}) water can be sucked in by a sideways entrance of the venturi tube to be sprayed against the bottom of the heating block. The presence of the inconel cylinder prevents contact between cooling water and sample. The required temperature of the heating element is achieved by heating it according to an adjustable heating profile. The temperature of the heating element is measured and compared with a programmable temperature profile. The difference between the temperature profile

and the actual measured temperature of the heating element is used for feed-back.

The temperature versus time and heating versus time profiles comprise a number of segments. Each segment is characterized by a heating rate (or cooling rate), dwell time, current through the heating element, and the way of cooling (no active cooling, cooling by pressured air or cooling by spraying water). The number of segments can be chosen freely. The temperature range of the heating element is from 290 K to 773 K. The maximum heating rate that can be achieved is on the order of 10 K s^{-1} and the maximum cooling rate is approximately 135 K s^{-1} in the temperature range of 773 K to 373 K.

The deviation between the desired and the measured temperature of the heating element is smaller than 0.1 K when a constant temperature level is applied. The aberration of an adjusted heating rate (or cooling rate) is less than 1%. Figure 4.3 shows an example of a measured temperature profile during operation.

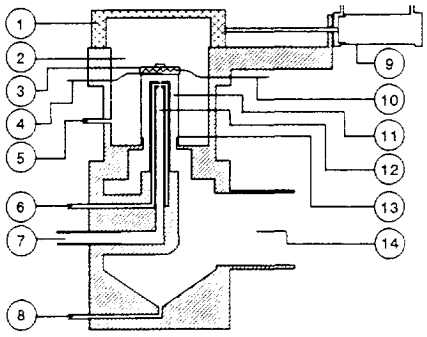

Fig. 4.2 Annealing oven. (1) sleeve valve, (2) sample chamber, (3) heating element with sample, (4) thermocouple, (5) nitrogen gas inlet, (6) water inlet for fast cooling, (7) pressured air inlet for cooling, (8) water drain, (9) piston for closing and opening sleeve valve, (10) heating wire, (11) cooling chamber, (12) venturi cooling tube, (13) inconel thin-walled cylinder, (14) air outlet.

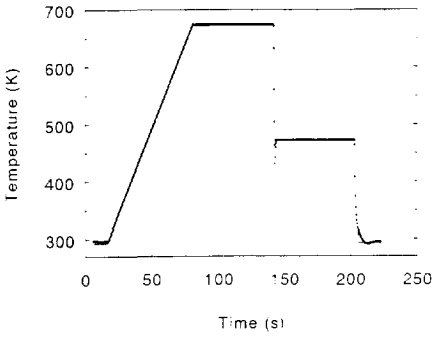

Fig. 4.3 An example of a thermal treatment in the annealing oven. The dots are measurements of the temperature and the solid line is the required temperature profile. Temperature profile: 6 Ks^{-1} from 293 K (20 °C) to 673 K (400 °C); 60 s at 673 K; -135 K s^{-1} from 673 K to 473 K (200 °C); 60 s at 473 K; -80 K/s from 473 K to 293 K.

4.3.4 Reader for TL emission spectra

The design of the heating element in the reader is similar to that of the annealing oven but with an optical fibre for light collection mounted through the sleeve-valve. The sample is laid down on the heating block. During the readout the light-tight sleeve valve is closed. In this position the entrance of the optical fibre is 2 mm above the sample. During the heating, the emitted light is guided through the optical fibre into the polychromator. Heating rates can be varied from 0.01 K s^{-1} up to 20 K s^{-1} and the temperature range is from 290 K to 773 K.

The entrance of the optical fibre is circular (diameter 5 mm). The exit of the optical fibre has a slit shape of 1 mm. For most experiments the exit of the optical fibre is used as entrance slit for the polychromator.

The polychromator is a MonoSpec 18 optical system with an aperture of F/3.8 and a focal length of 156 mm. The grating used has 150 grooves and a 450 nm blaze angle. The wavelength dispersion of the polychromator is 23.5 µm/nm.

The detector used is an intensified diode array (EG&G instruments type 1455B-512-HQ) with 512 active elements. The active elements are 25 µm wide and 2.5 mm high. The total width of the detecting area is 12.8 mm. This corresponds with a spectral range of 545 nm (from 206 nm to 751 nm in the present settings). The range of the detecting area can be shifted along the whole spectral range of the spectrometer from 200 to 800 nm. The detector contains a bi-alkali photocathode which emits electrons when struck by photons. The photo-electrons are multiplied in a microchannel plate (MCP) and strike a phosphor screen causing it to emit photons. The light output of the phosphor screen is coupled via fibre optics to the diode array. The detector is cooled down to -40 °C to reduce the background signal. The spectral response of the detector, the polychromator and the optical fibre is discussed in section 4.4. The measured spectrum is stored into the memory of the detector interface model (EG&G instruments model 1461) at fixed intervals. During the measurement the detector signal is monitored by an oscilloscope card PCIP-SCOPE (Keithley). The monitored signal is used to build up a 3D-picture on the computer screen during the measurement. This shows the operator a quick preview of the measured TL spectrum.

4.3.5 Software

A program has been written in Quick Basic to control the facility from an IBM compatible personal computer. The program is menu driven and makes it possible for the user to program thermal treatments for the oven (temperature profile), read-out parameters for the TL reader (like temperature profile, the segment of the temperature profile where the measurements of the TL emission start and the number and integration time of the measured emission spectra), and the irradiation time for the irradiator. The profiles and the read-out parameters can be stored in files. The program allows the user to create any desired treatment or measurement sequence. Sequences may include thermal treatment according to a previously programmed temperature profile, read out according to previously programmed read-out parameters and an irradiation according to an adjustable time interval. Figure 4.4 shows an example of a sequence. Accounts are kept of the positions of all samples. The user does not have to be concerned about the position of the samples on the facility or if one of the units is presently occupied by another sample. In an experiment the user only has to specify the sample and the unit. If the unit still contains another sample the program automatically empties the unit and brings the specified sample to the desired position. During the measurement of an emission spectrum a 3D-picture is built up and displayed. After the measurement of a TL emission spectrum the measured data (typical 126 spectra of 512 channels) is read from the OMA interface and stored on a 40 Mbyte hard disk. Data can be transported to a VAX-4300 computer for data analysis.

```
!          EXAMPLE TREATMENT AND MEASURE SEQUENCE
!-------------------------------------------------------------
!SAMPLES        DEVICE   CONFIGURATION          FILE
!-----------    NUMBER   (Irr. time, anneal     (to store the
!FIRST  LAST             or readout)            measurements)
!-----  -----   ------   -------------------    -------------
  1      5        4      ANNEAL1.ANN
  6      10       4      ANNEAL2.ANN
  1      5        3      370
  1      5        2      STKP03KS.STK           TEST2.HDR
  6      10       3      740
  6      10       2      STKP06KS.STK           TEST3.HDR
```

Fig. 4.4 An example of a command file for the performance of a thermal treatment, irradiation or read-out sequence. The lines beginning with the character ! are comment lines. The other lines stand for commands which perform a thermal treatment, irradiation or readout. The first two numbers denote the first and last sample on the store disk to undergo a specified treatment or measurement. The third number specifies the unit where the samples undergo their treatment or measurement (2: reader, 3: irradiator, 4: annealing oven). The files with the temperature profiles are denoted by the file name with the extension .STK for the reader and .ANN for the annealing oven. The file to store the measured data is denoted by the file name with the extension .HDR. The irradiation time is denoted by a number which expresses the irradiation time in seconds.

4.4 System response

The emission spectrum as measured by the detecting system is the resultant of the emitted spectrum and some aberrations. These aberrations, inherent to the system, should be taken into account when emission spectra are evaluated. Five types of system aberrations can be distinguished.

The first aberration is due to an off-set signal or dark count rate $F(i)$ per detector element i and could be easily corrected for by subtracting the off-set from the measured spectrum $M(i)$. The off-set is about 5 counts per second per detector element (corresponding to approximately 1 nm wavelength interval) and varies about 3 counts per second per detector element.

The second aberration is caused by the spectral response $P(\lambda)$ of the optical system including the optical fibre, the dispersive grating and the detector.

In the expression for $M(i)$ the undisturbed spectrum $I(\lambda)$ is multiplied by $P(\lambda)$. The spectral response is determined by measurements of the spectra of a tungsten and deuterium calibration lamp. Figure 4.5 shows the spectral response. The maximum in the spectral response at 420 nm is mainly determined by the blaze angle of the dispersive grating at 450 nm. At about 300 nm the efficiency of photocathode of the detector is maximal which results in a lump in the spectral response at about 300 nm.

The third aberration is caused by the varying sensitivity $g(x)$ along the detector with x the position along the detector. In the expression for the measured spectrum $M(i)$ the illumination $L(x)$ (corrected for the spectral response) at position x along the detector is multiplied by $g(x)$. It is difficult to measure $g(x)$. However, the sensitivity per detector element $G(i) = \int g(x)dx$ where the integral is over one detector element, can be measured easily by illuminating the detector homogeneously. The variation of the sensitivity of the detector elements is of the order of 15 %.

The finite width of the entrance slit and imperfections of the grating determine the wavelength resolution. The effect of this system property on the illumination at position x can be described by a convolution between the unperturbed spectrum $I(\lambda)$ and the resolution function $H(x)$. The resolution function describes the image (intensity as a function of the position) of a δ shaped spectral line on the detector. The illumination $L(x)$ at position x on the detector can now be written as:

$$L(x) = \int H\left(x - \frac{dx}{d\lambda}(\lambda-\lambda_0)\right) I(\lambda)\, d\lambda \qquad (4.1)$$

where $dx/d\lambda$ is the wavelength dispersion of the system and λ_0 is the wavelength corresponding with $x=0$. The function $H(x)$ has been determined by a measurement of the 435.83 nm spectral line of a mercury spectral lamp which was assumed to be δ shaped. The other spectral lines were filtered out by an interference filter. The results of the determination of $H(x)$ with different entrance slits are shown in Fig. 4.6. Results of measurements of the 365.0 nm mercury spectral line were similar and therefore it is assumed that $H(x)$ is wavelength independent. The full width at half maximum (FWHM) of this function for a 1 mm entrance slit is 0.67 mm. This corresponds with a wavelength resolution of 29 nm. The wavelength resolution for a 500 μm and a 25 μm slit are 18 nm and 6 nm, respectively.

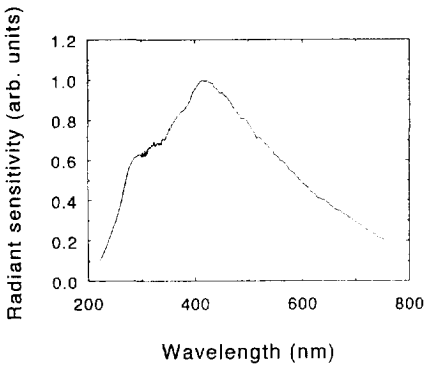

Fig. 4.5 Spectral response (detected energy per wavelength divided by the emitted energy per wavelength) of the optical system including optical fibre, dispersive grating and detector. In case one is interested in the number of detected photons divided by the number of emitted photons (arbitrary units) the curve should be divided by the wavelength.

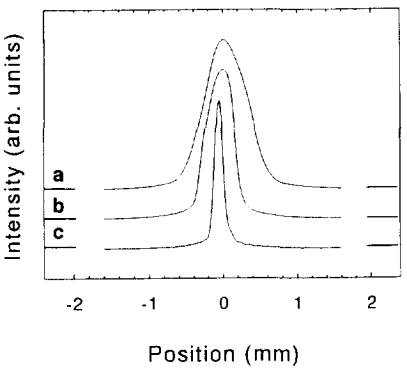

Fig. 4.6 Measured image function $H(x)$ of a single δ shaped spectral line using a slit width of (a) 1000 µm, (b) 500 µm, (c) 25 µm. The corresponding wavelength resolutions, defined by the Full Width at Half Maximum (FWHM) of $H(x)$ times the dispersion (23.5 µm/mm) are 29 nm, 18 nm and 6 nm respectively. The functions are normalized at the highest point.

Due to second order diffraction an additional spectrum appears at twice the wavelength. The contribution $\alpha(\lambda)$ to the measured spectrum caused by second order diffraction is expressed as a fraction of the corresponding spectrum caused by first order diffraction. This contribution is wavelength dependent. Figure 4.7 shows $\alpha(\lambda)$ determined from five lines from a mercury spectral lamp which show measurable second order lines.

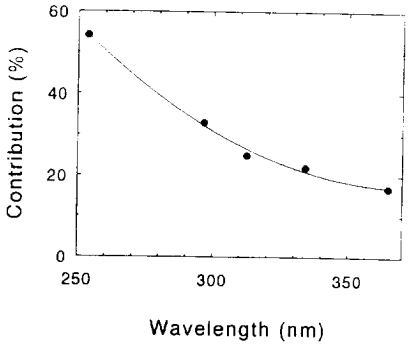

Fig. 4.7 Wavelength dependent contribution of the second order diffraction determined with five lines of the Hg-spectrum. The contribution is expressed in a percentage of the first order diffraction. The wavelength scale should be read as follows. If a source emits a first order signal at 260 nm with an intensity of 100 counts then at 520 nm a second order signal appears with an intensity of 50 counts.

With all above mentioned aberrations the measured spectrum can be expressed by:

$$M(i) = F(i) + \int_i g(x) \left\{ \int H\left(x - \frac{dx}{d\lambda}(\lambda-\lambda_0)\right) P(\lambda)\ I(\lambda)\ d\lambda + \int H\left(x - \frac{dx}{d\lambda}(2\lambda-\lambda_0)\right) \alpha(\lambda)\ P(\lambda)\ I(\lambda)\ d\lambda \right\} dx \tag{4.2}$$

where $I(\lambda)$ is the unperturbed emission. The integral over the position $\int_i dx$ is over the width of the detector element i. For our situation where the width of the detector element di/dx is much smaller than the width of the function $H(x)$, the function $g(x)$ can be approximated by a series of δ functions with a peak at each detector element:

$$g(x) = \sum_i G(i)\ \delta\left(x - \frac{dx}{di}(i-i_0)\right) \tag{4.3}$$

were i_0 is the index of the detector element at position $x=0$.
With Eq. (4.3), Eq. (4.2) becomes:

$$M(i) = F(i) + G(i) \left\{ \int H\left(\frac{dx}{di}(i-i_0) - \frac{dx}{d\lambda}(\lambda-\lambda_0)\right) P(\lambda)\ I(\lambda)d\lambda + \int H\left(\frac{dx}{di}(i-i_0) - \frac{dx}{d\lambda}(2\lambda-\lambda_0)\right) \alpha(\lambda)\ P(\lambda)\ I(\lambda)d\lambda \right\} \tag{4.4}$$

Equation 4.4 shows that the measured spectrum comprises three terms. The first term is an off-set signal, the second term is due to first order diffraction and the third term is due to second order diffraction.

4.5 Method of data analysis

In this section it is described how measured data can be related to curves predicted by a model for light emission. The method is illustrated with the Franck-Condon model as used by Fairchild *et al* (1978) but can be applied to any model for light emission (*eg.* the simple version of the Franck-Condon model as described in chapter 3). The Franck-Condon model (Fairchild *et al* 1978, Lax 1952) describes a single emission band by a Gaussian shaped curve as a function of energy. The shape of a single emission band describing the spectral irradiance $I(\lambda)$ (J m^{-3} s^{-1}) as function of the wavelength λ (m) is according to this model (see chapter 3):

$$I(\lambda) = \frac{h^2c^2}{\lambda^3} \frac{A}{U\sqrt{2\pi}} \exp\left(\frac{-(E-E_0)^2}{2U^2}\right) \tag{4.5}$$

where h is Planck's constant (J s), c is the velocity of light (m s^{-1}), A is the total number of photons per steradian per second (m^{-2} s^{-1}), E is the energy of the photon with wavelength λ: $E = hc/\lambda$ (J), E_0 is the photon energy at the maximum of the emission peak (J) and U is a measure of the width of the emission band (J). E_0 and U are dependent on the temperature according to:

$$E_0 = C_1 - C_2 \coth\left(\frac{\hbar\omega}{2kT}\right) \tag{4.6}$$

$$U^2 = S\,(\hbar\omega)^2 \coth\left(\frac{\hbar\omega}{2kT}\right) \tag{4.7}$$

where C_1 is the initial energy (J), C_2 is a constant (J), $\hbar$ is Dirac's constant (J s), $\omega/2\pi$ is the vibrational frequency (Hz), k is Boltzmann's constant ($J{\cdot}K^{-1}$) and S is the Rhys-Huang factor. In spectra which comprise more than one emission band the total spectrum is formed by a summation of the different bands.

To relate this model to a measured spectrum, for each emission band in the spectrum the parameters C_1, C_2, S, ω, and A are fitted by a minimization

procedure of the weighted sum of squared differences between the measured spectrum and the spectrum according to the model. The weight w of the terms is determined by the square of the estimated error σ in the measured spectrum: $w = \sigma^{-2}$.

The estimation of the error σ is based on Poisson statistics of the measured photons *i.e.* σ is proportional to the square root of the number of measured photons: $\sigma_{ij}^2 = \alpha M(i,T_j)$ where α is the number of counts per measured photon. At maximum sensitivity α = 1.3 counts per photon.

When the minimization procedure is applied, one should take into account the system response as described in the previous section. This can be done in two ways: (1) by a *de*convolution of the measured spectrum and a comparison of the result with the spectrum predicted by the model, (2) by a convolution of the spectrum predicted by the model and a comparison of the result with the measured spectrum. When method (1) is used, the errors in the points of the deconvoluted spectrum become correlated. Because of this correlation the sum of squared differences between the deconvoluted spectrum and the predicted spectrum is not any longer the statistical correct parameter to minimise for determining the best fit (Martin 1971). It is possible to correct the sum of squared differences for the correlation between the points of the deconvoluted spectrum, however this requires a significant number of extra summations and thus much more computation time. The calculations are less complicated when method (2) is used. Method (2) keeps the data points of the measured spectrum intact. The errors of the data points remain uncorrelated and no corrections on the sum of squared differences are necessary. For this reason we used method (2) to correct for the system response. The convoluted spectrum predicted by the model is described by Eq. (4.4) in which the functions $F(i)$, $G(i)$, $H(x)$, $P(\lambda)$ and $\alpha(\lambda)$ are known and $I(\lambda)$ is given by Eq. (4.5). The expression to be minimized is a function of the parameters C_1, C_2, S, ω, and A of all emission bands. It is denoted by Q^2 and can be written as:

$$Q^2(C_1, C_2, S, \omega, A, \ldots\ldots) = \sum_i \sum_j \frac{\left(M(i,T_j) - M'(i,T_j)\right)^2}{\sigma_{ij}^2} \qquad (4.8)$$

where $M(i,T_j)$ is the convoluted spectrum predicted by the model at temperature T_j, and $M'(i,T_j)$ is the measured spectrum. The index i indicates a summation over the detector elements (wavelengths), and the index j indicates a summation over all temperature regions. The dots indicate the dependence of Q^2 on the

same kind of parameters of other emission bands (if present). The number of emission bands is not a fitting parameter. If the number of bands is not known it can be found by fitting the spectrum several times with a different number of bands.

We note that this method of data analysis implies a simultaneous fit of measured emission spectra at different temperature regions *j*. The parameters describing the theoretical shift and broadening of the peak as function of the temperature [see Eq. (4.6) and Eq. (4.7)] are therefore simultaneously fitted by the parameters describing the shape of the emission bands at one temperature. In other words it is not just the shape of one emission spectrum which is analyzed but also how this shape changes with temperature.

4.6 Performance

4.6.1 Example of emission spectrum

Figure 4.8 shows a measured emission spectrum of a LiF:Mg,Ti(TLD-100) sample (3.2 mm x 3.2 mm x 0.9 mm) represented as a 3D-plot and a contour plot. The sample was obtained from Harshaw Chemical Company, Ohio, USA. The annealing procedure was: 1 hour at 673 K followed by a fast cooling down to room temperature. The sample was irradiated to an absorbed dose in air of 5 Gy and read out at a heating rate of 3 K s^{-1}. The temperature resolution is 2.6 K and the wavelength resolution is 29 nm. The emission is peaked around 410 nm. The four glow peaks, in the usual nomenclature peak 2 (at 403 K), peak 3 (at 446 K), peak 4 (at 478 K) peak 5 (at 505 K), and a complex of high temperature peaks (at 560 K) are recognized.

4.6.2 Sensitivity

To demonstrate the sensitivity of the TL spectrometer the measured emission spectrum of CaF_2:Dy(TLD-200) irradiated to an absorbed dose in air of 3 mGy and read out at a heating rate of 6 K s^{-1} is shown in Fig. 4.9. The sample was obtained from Harshaw Company, Ohio, USA and its dimensions are 3.2 mm x 3.2 mm x 0.9 mm. The annealing procedure was 1 hour at 673 K (400 °C) followed by a fast cooling down to room temperature. The resolution in wavelength is 29 nm and the resolution in temperature is 22 K. The signal to noise ratio is about 10:1 at the highest intensity in this spectrum. The two dominant emission bands at 480 nm and 580 nm are clearly seen. The rise at the

long wavelength - high temperature corner is caused by the thermal emission of the gold plate.

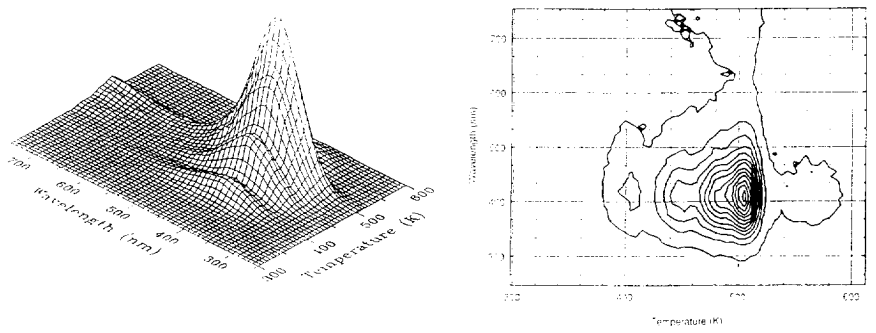

Fig. 4.8 Three-dimensional plot and a contour plot of an emission spectrum of LiF:Mg,Ti (TLD-100). The spectrum has not been corrected for the system response. The annealing procedure was 1 hour at 673 K followed by a rapid cooling down to room temperature. The absorbed dose is 5 Gy. The heating rate during the measurement was 3 K s^{-1}.

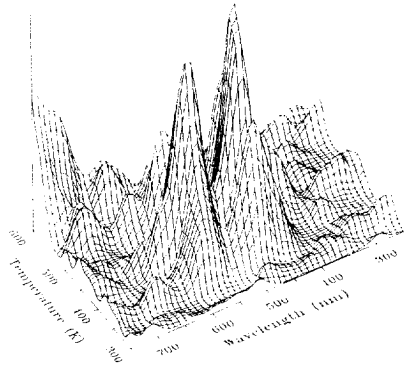

Fig. 4.9 TL emission spectrum of CaF_2:Dy (TLD-200) irradiated to an absorbed dose of 3 mGy in air.

4.6.3 Analysis of TLD-100 emission spectrum

The emission spectrum of LiF:Mg,Ti from Fig. 4.8 has been analyzed according to the Franck-Condon model for three samples. The parameters ω and C_2 were fixed at the values given by Fairchild *et al* (1978), i.e. $\omega/2\pi = 2.21 \cdot 10^{13}$ Hz and $C_2 = 0.04$ eV. The other parameters were fitted by minimizing Q^2 [see Eq. (4.8)]. The summation in the expression of Q^2 is over five temperature intervals of 26 K (403 K, 446 K, 478 K, 505 K and 560 K at the middle of the intervals) and over 300 detector elements. The fitting range is from 326 nm to 645 nm. The number of degrees of freedom ν of the fit is 1486. From Fig. 4.10 it is seen that the reduced chi-square χ^2/ν (χ^2 is the minimum of Q^2) is expected to be found in a small area around 1. However, the value of χ^2/ν does not only depend on the 'goodness of fit' but also on the 'goodness of the estimation of the errors'. A deviation of 5 % in the estimation of the errors results in a shift of the χ^2/ν-distribution of 0.1. The estimated error squares are $\sigma^2 = 1.3\, M(i,T_j)$ counts.

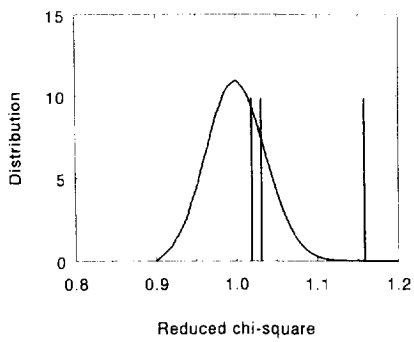

Fig. 4.10 The probability distribution function for χ^2/ν with 1486 degrees of freedom. The distribution is calculated with (Bevington 1969 p. 189):

$$P(\chi^2,\nu) = \frac{(\chi^2)^{1/2(\nu-2)}\, e^{-\chi^2/2}}{2^{\nu/2}\, \Gamma(\nu/2)}$$

where ν is the number of degrees of freedom and $\Gamma(x)$ is equivalent to the factorial function $x!$ extended to nonintegral arguments. For integral and half integral arguments: $\Gamma(1) = 1$, $\Gamma(1/2) = \sqrt{\pi}$ and $\Gamma(x+1) = x\Gamma(x)$

The three bars are the reduced chi-squares of the fits of the emission spectra of three samples to the Franck-Condon model.

The calculations for the fitting procedure are performed on a VAX-4300 computer using the routine FATAL (Salmon and Booker 1972). The time required to compute the best fit is typically five minutes. The best fits are obtained with two emission bands with reduced chi-squares of 1.02, 1.03 and 1.16 (see Fig. 4.10). The results for the averaged values of the parameters are shown in Table 4.1. Figure 4.11 shows the fitting result for one sample. If the spectra are fitted with three bands the third peak drifts away from the fitting region. When fitted with one band no satisfactory fits were obtained (the values of the reduced chi-squares are 2.78, 2.64 and 2.82).

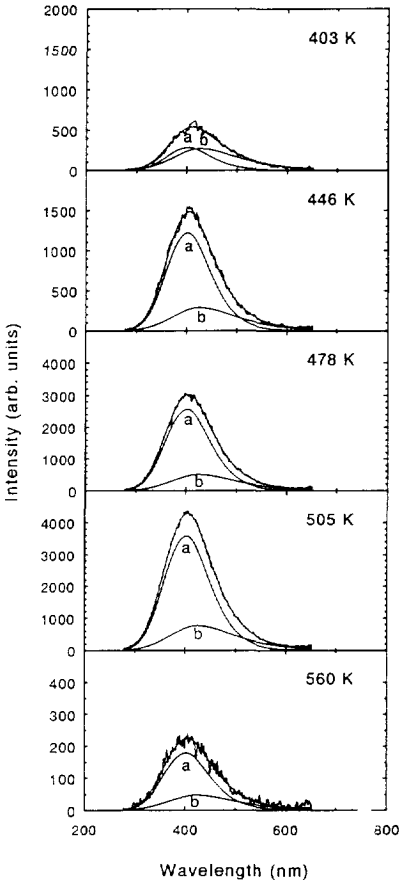

Fig. 4.11 Results of an analysis of the TL emission spectrum of LiF:Mg,Ti (TLD-100) shown in Fig. 4.8 at different temperatures (indicated at the right top corner of each graph) using the Franck-Condon model. The emission spectra at 403 K, 446 K, 478 K, and 505 K correspond to the glow peaks 2, 3, 4, and 5. The emission spectrum at 560 corresponds to the glow peaks 6 to 11. The band energies at 463 K of the emission bands are (a) 3.03 eV and (b) 2.63 eV. It is seen that the ratio of the intensities of both emission bands vary with the temperature. The fringy curves are measured; the smooth curves are fitted.

Table 4.1 Parameters of TL emission spectrum of TLD-100

Author	Band	E_0[(b)] (eV)	FWHM[(c)] (eV)	C_1 (eV)	C_2[(d)] (eV)	S	$\omega/2\pi$[(d)] (Hz)
Fairchild[a]	1	3.01	0.90	3.07	0.04		$2.21 \cdot 10^{13}$
	2	2.90	0.72	2.94	0.04		$2.21 \cdot 10^{13}$
	3	2.71	0.96	2.75	0.04		$2.21 \cdot 10^{13}$
This work	1	3.03±0.01	0.83±0.01	3.08±0.01	0.04	12.4±0.2	$2.21 \cdot 10^{13}$
	2	2.62±0.04	0.94±0.04	2.68±0.04	0.04	15.6±1.2	$2.21 \cdot 10^{13}$

[a]Fairchild *et al* 1978.
[b]E_0 is calculated with Eq. (4.6) at 463 K (190 °C).
[c]FWHM = $2U\sqrt{[2\ln(2)]}$, and U calculated with Eq. (4.7) at 463 K.
[d]Not fitted.

4.7 Discussion and conclusions

The TL facility described in this chapter is a reliable, easy to use and fully automated system for the measurement of emission spectra during thermoluminescence of samples subjected to controllable thermal treatments and irradiated to adjustable absorbed doses. The facility allows experiments by which effects of thermal treatments on trapping and luminescent centres can be studied. The TL emission spectrometer of the TL research facility is very sensitive in the UV-VIS region (200 nm - 800 nm). The wavelength resolution is 29 nm which is sufficient for most measurements of TL emission spectra. A better resolution (down to 6 nm) can be obtained but at the expense of the sensitivity. TL emission spectra of LiF:Mg,Ti (TLD-100) and CaF_2:Dy (TLD-200), irradiated to absorbed doses as low as 75 mGy and 3 mGy respectively, could be measured at a signal to noise ratio of about 10:1. Although it is difficult to compare different spectrometers from the literature we think that our spectrometer is one of the most sensitive spectrometers based on the principle of a dispersive system employed nowadays in TL spectroscopy (Kanemaki *et al* 1991, Bakas 1984, Huntly *et al* 1988, Luff and Townsend 1992). Spectrometers based on Fourier transform spectroscopy (Prescott *et al* 1988, Haschberger 1991) are comparable or show a higher

sensitivity compared to the spectrometer described in this chapter. A limitation of these spectrometers, however, is a lower spectral cut-off at 350 nm.

The TL emission spectra measured with the facility can be evaluated according to an analysis method that accounts for the system response. When the Franck-Condon model for emission is used in the analysis, a good fit is obtained for the LiF:Mg,Ti emission bands. The parameters of the high energy band are in good agreement with the parameters found by Fairchild *et al* (1978) and Delgado and Delgado (1984). However we found just two emission bands contributing to the emission spectrum while Fairchild *et al* (1978) and Delgado and Delgado (1984) found three emission bands. This discrepancy is probably caused by the high overlap of the emission bands. The high overlap of the bands makes it difficult to resolve the different bands and differences in analyzing method could lead to different results. Our analyzing procedure is different from that of Fairchild *et al* (1978) in two aspects. Firstly, we did not deconvolute the measured spectrum but convoluted the spectrum obtained from the model. Secondly we fitted the spectrum at different temperatures simultaneously with the parameters C_1, C_2, and S for each band equally at each temperature interval while Fairchild fitted the emission spectrum at each temperature interval separately.

Chapter 5

Effects of non-ideal heat transfer on glow curve and emission spectrum analysis

Abstract: In this chapter a simple model for the heat transmission between a heating element and a thermoluminescent sample is used to estimate the temperature lag of the sample with respect to the heating element during linear heating. According to the model the temperature lag is linear dependent on the heating rate (β) and temperature difference between heating element (T_1) and the surroundings (T_g). For a LiF:Mg,Ti (TLD-100) sample with dimensions 3.2 x 3.2 x 0.9 mm^3 the temperature lag during the linear heating is $\Delta T = 1.7\beta + 0.037(T_1 - T_g)$. The non-uniformity of the temperature inside a TLD-100 sample can be neglected. The consequences of neglecting the temperature lag on glow curve analysis and analysis of the luminescence emission spectrum are discussed.

5.1 Introduction

An important part of thermoluminescence measurements concerns the heating of the thermoluminescent sample during the readout. There are various types of heating (planchet heating, gas heating, microwave heating and laser heating) but the far most widespread form of heating is planchet heating (Mahesh *et al* 1989, McKeever 1985).

Planchet heating is the heating of a planchet or heating element on which the thermoluminescent sample is placed. The heating element and sample are placed in an inert gas to avoid chemiluminescence. The temperature control is achieved by means of a thermocouple mounted on the heating element. This method of temperature control regulates only the temperature of the heating element and not the temperature of the sample placed on it. It is inevitable that during heating there is a difference between the temperature of the sample and the heating element. This difference in temperature could influence the outcome of an analysis of the emitted light intensity versus temperature because the only information about the temperature that is obtained from a measurement is that of

the heating element.

In this chapter the influence of a small temperature difference between the measured temperature of the heating element and the real temperature of the sample, on the analysis of glow curves and emission spectra is described. A simple model for heat transfer is used to describe the temperature difference. Experiments are performed to get an estimation of the temperature difference between sample and heating element.

5.2 A model for the heat transfer

In this section a formula for the sample temperature is derived in case the heating element is heated at a constant rate. The formula is derived from a (simple) model for heat transfer from the heating element to the sample and from the sample to the surroundings. This model assumes that all heat transmission is due to conduction. This is certainly not true for heat transmission from the sample to the surroundings where convection plays an important role. The description of the heat transmission due to conduction must therefore be interpreted as a first order approach. The heat transfer between the heating element and the sample is schematically represented in Fig. 5.1.

In Fig. 5.1, five compartments are distinguished, the heating element (h), the contact layer (c), the sample (s), the sample-gas interface (d) and the surroundings. Each compartment can be characterised by a heat capacity C (J K^{-1}) and a thermal conductance H (J K^{-1} s^{-1}). The heat is transferred from the heating element to the sample through the contact layer. From the top and the sides of the sample, heat is transferred to the surroundings through the sample-gas interface. The contact layer and the sample-gas interface are imaginary zones of which the properties represent the non-ideal heat transfer from the heating element to the sample and from the sample to the surroundings. For simplicity some assumptions are made:

(1) The temperature distributions inside the heating element and sample are homogeneous. This assumption is true if the diffusivity of these compartments is very large. In appendix B the temperature difference between top and bottom of the sample and of the heating element is estimated. This difference depends on the heating rate, the temperature and the thickness of the sample or heating element. For a 0.9 mm thick LiF sample at 450 K and a heating rate of 6 K s^{-1} the temperature

difference between top and bottom of the sample is about 2 K. The temperature difference between top and bottom of the heating element (3 mm thick, at 450 K and heating rate of 6 K s^{-1}) is about 0.3 K.

(2) The surrounding temperature is constant.

(3) The heat capacities of the contact layer and the sample-gas interface are zero.

(4) The heat capacities and the thermal conductance of the compartments are temperature independent. For the heat capacity of a LiF sample the validity of this assumption can be checked. The specific heat of LiF is (13.2 + 0.0084 T) J kg^{-1} K^{-1}. So changes in the heat capacity in a temperature range of 100 K are on the order of 6 %.

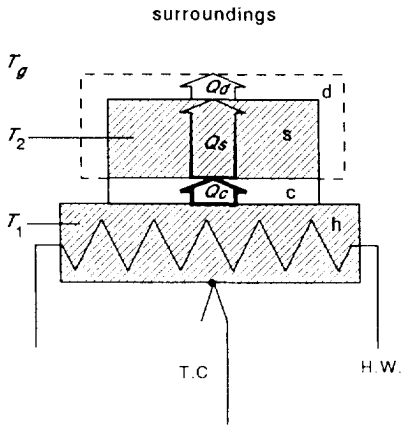

Fig. 5.1 Schematic representation of the heat transfer between heating element, sample and the surroundings. (h) = heating element, (c) = contact layer, (s) = sample and (d) = sample-gas interface. T_1 is the temperature of the heating element, T_2 is the temperature of the sample and T_g is the temperature of the surroundings. T.C. is thermocouple and H.W. is heating wire.

To describe the heat transfer the following symbols are used:

Q_c = Energy transferred from the heating element to the sample (J)

Q_d = Energy transferred from the sample to the surroundings (J)

H_c = Thermal conductance of the contact layer (J s^{-1} K^{-1})

H_d = Thermal conductance of the sample-gas interface (J K^{-1} s^{-1})

H' = $H_c + H_d$

C_s = Heat capacity of the sample (J K^{-1})

T_1 = Temperature of the heating element measured with the

thermocouple (K)

T_2 = Temperature of the sample (K)

ΔT = Temperature lag of sample: $T_1 - T_2$

T_g = Temperature of the surroundings (K)

T_0 = Temperature of the sample and heating element at t = 0 s (K)

T_0' = Effective starting temperature: $T_0 - \beta' C_s/H'$

β = Heating rate (K s^{-1})

β' = Effective heating rate: $(H_c/H')\beta$

The change of the sample temperature dT_2/dt is equal to:

$$\frac{dT_2}{dt} = \frac{1}{C_s}\left(\frac{dQ_c}{dt} - \frac{dQ_d}{dt}\right) \tag{5.1}$$

where dQ_c/dt is the rate of heat transfer through the contact layer from heating element to the sample and dQ_d/dt is the rate of heat transfer through the sample-gas interface from the sample to the surroundings. The rate of heat transfer through the contact layer dQ_c/dt is:

$$\frac{dQ_c}{dt} = H_c(T_1 - T_2) \tag{5.2}$$

and the rate of heat transfer through the sample-gas interface dQ_d/dt is:

$$\frac{dQ_d}{dt} = H_d(T_2 - T_g) \tag{5.3}$$

Substituting Eq. (5.2) and Eq. (5.3) into Eq. (5.1) gives:

$$\frac{dT_2}{dt} = \frac{H_c}{C_s}(T_1 - T_2) - \frac{H_d}{C_s}(T_2 - T_g) \tag{5.4}$$

For a linear heating profile: $(T_1 = T_0 + \beta t)$ Eq. (5.4) becomes:

$$\frac{dT_2}{dt} = \frac{H_c T_0 + H_d T_g + H'(\beta' t - T_2)}{C_s} \tag{5.5}$$

where $\beta' = \beta H_c/H'$ and $H' = H_c + H_d$. The solution of Eq. (5.5) is:

$$T_2(t) = \frac{H_c T_0 + H_d T_g}{H'} + \beta' t - \left[1 - \alpha \exp\left(-\frac{H'}{C_s} t\right)\right] \beta' \frac{C_s}{H'} \qquad (5.6)$$

The value of the coefficient α depends on the start condition $T_2(t=0)$. Figure 5.2 shows a simulation of the temperature of the heating planchet and the sample versus time according to Eq. (5.6) with realistic values of $\beta' = 10$ K s^{-1}, $C_s/H' = 3$ s, $H_d/H' = 0.03$, $T_0 = T_g = 300$ K and $\alpha = 1$ ($T_2(t=0) = T_0$) (see section 5.5).

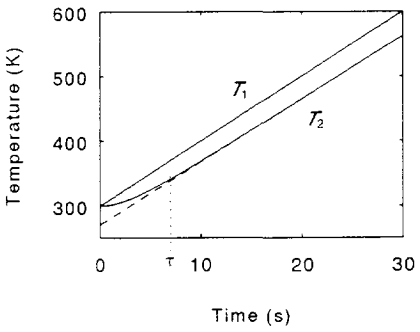

Fig. 5.2 Simulation of sample temperature T_2 as function of time. T_1 is the temperature profile of the heating element. The heating rate $\beta = 10$ K s^{-1}, $C_s/H' = 3$ s, $H_d/H' = 0.03$, $T_0 = T_g = 300$ K and $\alpha = 1$. After a start period κ the heating of the sample is almost linear with heating rate $\beta' = 9.7$ K/s and $T_0' = 270.9$ K (broken line).

After a transient period, the factor $[1-\alpha\exp(-H't/C_s)]$ approaches to 1, so Eq. (5.6) can be approximated by:

$$T_2(t) = T_0' + \beta' t \qquad (5.7)$$

where $T_0' = (H_c T_0 + H_d T_g - \beta' C_s)/H'$. Thus, after a start period, the temperature profile of the sample has the same form as that of the heating element but with the heating rate β replaced by an effective heating rate β' and the starting temperature T_0 replaced by an effective starting temperature T_0'. The temperature lag ΔT of the sample with respect to the measured temperature is:

$$\Delta T = T_1 - T_2 = \frac{\beta' C_s + H_d (T_1 - T_g)}{H'} \qquad (5.8)$$

In the next paragraph it is described how the temperature lag affects the analysis of glow curves and emission spectra. In paragraph 5.5 the temperature lag is estimated quantitatively.

5.3 Effect of temperature lag on the glow curve

The light intensity emitted by the sample during the heating up can be described by the well known Randall-Wilkins model (see chapter 1). This model comprises three parameters per glow peak *i.e.* the initial concentration of trapped charge carriers $n(t=0)$, the activation energy E and the frequency factor s. In case the temperature lag of the sample is ignored, the light intensity $I(t)$ is:

$$I(t) = n\,s\exp(-E/kT_1) \tag{5.9}$$

where n satisfies:

$$\frac{dn}{dt} = -n\,s\exp\left(-\frac{E}{kT_1}\right) \tag{5.10}$$

If the temperature lag is taken into account Eq. (5.9) becomes:

$$I(t) = n\,s\exp\left(-\frac{E}{k(T_1-\Delta T)}\right) \tag{5.11}$$

The errors that are made in the determination of E and s if Eq. (5.9) is used and ΔT cannot be neglected (but is still small), can be determined by comparing Eq. (5.11) with Eq. (5.9). Although these equations are of a different form Eq. (5.11) can be approximated by a function of the same form as Eq. (5.9). To do so the exponent in Eq. (5.11) is developed around T_m (temperature of the maximum TL intensity) into powers of $(T_1 - \Delta T - T_m)$:

$$\begin{aligned}
\frac{E}{k(T_1-\Delta T)} &= \frac{E}{k}\,\frac{1}{T_m + (T_1 - \Delta T - T_m)} = \frac{E}{k}\sum_{i=0}^{\infty}\frac{(-T_1 + \Delta T + T_m)^i}{T_m^{(i+1)}} \\
&\approx \frac{E}{k}\left(\sum_{i=0}^{\infty}\frac{(-T_1 + T_m)^i}{T_m^{(i+1)}} + \frac{\Delta T}{T_m}\sum_{i=0}^{\infty}(i+1)\,\frac{(-T_1 + T_m)^i}{T_m^{(i+1)}}\right) + O\left(\frac{\Delta T^2}{T_m^3}\right) \\
&\approx \frac{E}{k}\left(\frac{1}{T_1} + \frac{2\Delta T}{T_m T_1} - \frac{\Delta T}{T_m^2}\right) + O\left(\frac{\Delta T(T_m-T_1)^2}{T_m^4}\right)
\end{aligned} \tag{5.12}$$

So Eq. (5.11) becomes:

$$I(t) = n\, s \exp\left(\frac{\Delta T E}{k T_m^2}\right) \exp\left(-\frac{E(1+2\Delta T / T_m)}{kT_1}\right) \tag{5.13}$$

This equation has the same form as Eq. (5.9) but with s in Eq. (5.9) replaced by $s' = s \exp[(\Delta TE)/(kT_m^2)]$ and E by $E' = E(1+2\Delta T/T_m)$. From Eq. (5.9) it is seen that if the temperature lag is ignored the activation energy and the logarithm of the frequency factor are overestimated by an amount of:

$$\begin{aligned} \Delta E &= \frac{2\,\Delta T}{T_m} E \\ \Delta \ln(s) &= \frac{\Delta E}{2kT_m} \end{aligned} \tag{5.14}$$

For realistic values of ΔT = 14 K, T_m = 450 K, E = 1.7 eV and $\ln(s)$ = 43 the overestimation is: ΔE = 0.1 eV and $\Delta \ln(s)$ = 1.35

5.4 Effect of temperature lag on the emission spectrum

The emission spectrum can be described by the simple version of the Franck-Condon model of chapter 4. In this model, only the width of the emission band depends on the temperature. If the temperature lag is ignored the width U of the emission band is:

$$U^2 = 2C q_0^2 kT_1 \tag{5.15}$$

where Cq_0^2 is the unknown parameter to be determined. If the temperature lag is not ignored Eq. (5.15) becomes:

$$U^2 = 2C q_0^2 k(T_1 - \Delta T) \tag{5.16}$$

For small ΔT, Eq. (5.16) can be approximated by:

$$U^2 \approx 2C q_0^2 kT_1 \left(1 - \frac{\Delta T}{T_m}\right) \tag{5.17}$$

so that an expression of the same form as that of Eq. (5.15) is obtained with the parameter Cq_0^2 replaced by $Cq_0^2(1-\Delta T/T_m)$. So the value of the parameter Cq_0^2 is

underestimated by an amount of:

$$\Delta C\, q_0^2 = \frac{\Delta T}{T_m} C\, q_0^2 \qquad (5.18)$$

For realistic values of ΔT = 14 K, T_m = 450 K and Cq_0^2 = 3 eV the underestimation is ΔCq_0^2 = 0.09 eV.

5.5 Estimation of the temperature lag

The parameters describing the heat transfer are C_s, H_c, H_d and T_g. The value of C_s can be calculated from the dimensions of the sample and data from literature (see Table 5.1):

$$C_s = c_s \rho_s A_s d_s \qquad (5.19)$$

where ρ_s is the density of the sample, c_s is the specific heat, A_s is the area of the top of the sample and d_s is the thickness of the sample. The thermal conductance of the sample-gas interface H_d is:

$$H_d = h_d (A_s + L_s d_s) \qquad (5.20)$$

where h_d is the heat transfer coefficient and L_s is the perimeter of the sample. The factor $(A_s + L_s d_s)$ is the total area of the sample for heat dissipation A_d.

In this paragraph a method for the determination of H_c, h_d and T_g is described. The heating element used in the experiment is the heating element of the reader of the TL research facility described in chapter 4. The samples used are polycrystalline LiF:Mg,Ti(TLD-100) with dimensions 3.2 x 3.2 x 0.9 mm^3 (Harshaw). So the perimeter L_s of the samples is 4 x 3.2 = 12.8 mm and the heat transfer area A_s is 3.2 x 3.2 = 10.2 mm^2. To obtain samples with different heat capacity, the samples of six groups have been scoured off to a thickness d_s of 0.8 mm, 0.7 mm, 0.6 mm, 0.5 mm, 0.4 mm and 0.3 mm. Each group contains three samples.

Table 5.1 Physical quantities of the heat transfer compartments of Fig. 5.1. The table contains physical quantities of LiF (sample material) Cu and Au (heating element materials). The dimensions of the samples, the thermal conductances and heat capacities are included as well.

Quantity	Value	Dimension	Description	ref[1].
M_s	2.59×10^{-2}	kg mol^{-1}	Molar mass of LiF	(a)
ρ_s	2.64×10^{3}	kg m^{-3}	Density of LiF	(a)
c_s[2,4]	1.70×10^{3}	J kg^{-1} K^{-1}	Specific heat of LiF	(b)
k_s[2,5]	9.0	J K^{-1} m^{-1} s^{-1}	Thermal conductivity of LiF	
a_s[2,6]	2.1×10^{-6}	m^2 s^{-1}	Diffusivity of LiF	(c)
T_μ	1115	K	Melting point of LiF	(a)
ρ_{Cu}	8.96×10^{3}	kg m^{-3}	Density of Cu	(d)
c_{Cu}	3.9×10^{2}	J kg^{-1} K^{-1}	Specific heat of Cu	(d)
k_{Cu}	3.9×10^{2}	J K^{-1} m^{-1} s^{-1}	Thermal conductivity of Cu	(d)
a_{Cu}	1.1×10^{-4}	m^2 s^{-1}	Diffusivity of Cu	
ρ_{Au}	1.93×10^{4}	kg m^{-3}	Density of Au	(d)
c_{Au}	1.3×10^{3}	J kg^{-1} m	Specific heat of Au	(d)
k_{Au}	3.0×10^{2}	J K^{-1} m^{-1} s^{-1}	Thermal conductivity of Au	(d)
a_{Au}	1.2×10^{-4}	m^2 s^{-1}	Diffusivity of Au	
d_h	3×10^{-3}	m	Thickness of heating element	
k_h	3.5×10^{2}	J K^{-1} m^{-1} s^{-1}	Thermal conductivity of heating element (mean of k_{Au} and k_{Cu})	
a_h	1.15×10^{-4}	m^2 s^{-1}	Diffusivity of heating element material (mean of a_{Au} and a_{Cu})	
H_c	$(22.5\pm1.7)\times10^{-3}$	J K^{-1} s^{-1}	Thermal conductance of contact layer	(e)
A_s[7]	1.02×10^{-5}	m^2	Heat transfer area of sample	
d_s[7]	9×10^{-4}	m	Thickness of sample	
L_s[7]	1.28×10^{-2}	m	Outline of sample	
m_s[7]	2.43×10^{-5}	kg	Mass of sample	
C_s[2,7]	4.13×10^{-2}	J K^{-1}	Heat capacity of sample.	
A_d[7]	2.18×10^{-5}	m^2	Heat transfer area of dissipation layer	

Continuation of table 5.1.

Quantity	Value	Dimension	Description	ref[1].
h_d[3]	38±20	J K^{-1} m^{-2} s^{-1}	Heat transfer coefficient for solid-gas interfaces	(e)
H_d[7]	(8.3±4.3)x10^{-4}	J K^{-1} s^{-1}	Thermal conductance for heat transfer from the sample to the surrounding gas	
T_g	333±80	K	Temperature of surroundings	(e)

1) References (a): Weast *et al* 1965, (b): Perry and Chilton 1973, (c): Touloukian 1970, (d): Jansen 1977, (e): This work

2) At 450 K

3) Heat transfer coefficient for a solid-gas interface is about 17 J K^{-1} m^{-2} s^{-1} to 57 J K^{-1} m^{-2} s^{-1} [ref. (b)]

4) c_s = (13.2 + 0.0084 T) J kg^{-1} K^{-1}

5) $k_s = a_s c_s \rho_s$

6) a_s = (6.05 - 0.0086 T)x10^{-6} m^2 s^{-1}. The coefficients are calculated with data from Touloukian (1970) in the temp region 350 K - 550 K

7) For a LiF sample with dimensions 3.2 x 3.2 x 0.9 mm^3

Before each experiment was started, the samples were submitted to an annealing procedure of 1 hour at 673 K followed by a quick cooling to room temperature. All samples were irradiated with a ^{60}Co source to an absorbed dose of 25 Gy and read out at heating rates of 10 K s^{-1}, 6 K s^{-1} and 3 K s^{-1}. The glow curves of the different samples obtained by the same heating rate consist of four peaks which appear for all samples at the same sample temperature but at a different heating element temperature depending on the thickness of the samples. By rewriting Eq. (5.7) and usage of equations (5.19) and (5.20) a relationship between T_1 and d_s is obtained:

$$T_1 = T_2 + \frac{(T_2 - T_g)h_d(A_s + L_s d_s)}{H_c} + \frac{\beta c_s \rho A_s d_s}{H_c + h_d(A_s + L_s d_s)} \qquad (5.21)$$

Figure 5.3 shows the heating element temperature versus the sample thickness

for four sample temperatures corresponding to the temperature of maximum TL intensity of the four glow peaks of TLD-100 numbered according to the usual numbering: 2, 3, 4, and 5 and three heating rates. Temperatures at peak maxima were determined by glow curve fitting. The parameters H_c, h_d and T_g and the sample temperatures T_2 at the peak maxima can be obtained by fitting Eq. (5.21) to the data of Fig. 5.3. The values for H_c, h_d and T_g obtained in this way are: H_c = (22.5 ± 1.7)x10^{-3} J K^{-1} s^{-1}, h_d = (38 ± 20) J K^{-1} s^{-1} m^{-2} and T_g = (333 ± 80) K. The correlations are: $Cor(H_c,h_d)$ = -0.10, $Cor(H_c,T_g)$ = -0.71 and $Cor(T_g,h_d)$ = 0.69. The values of the sample temperatures (T_2) corresponding to the maxima of the glow peaks are shown in Table 5.2.

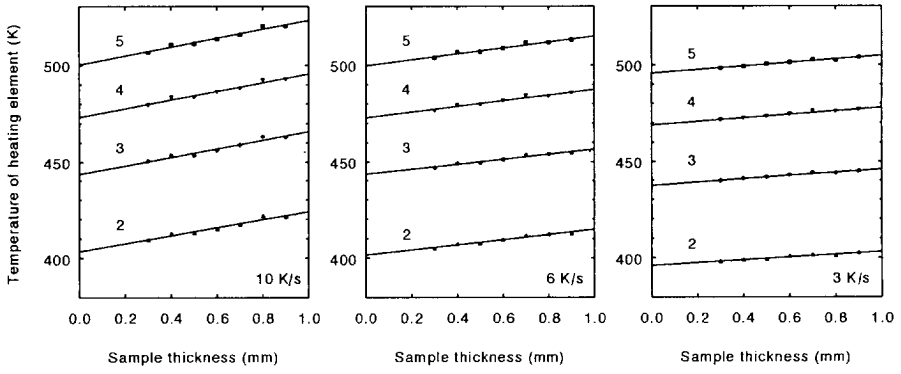

Fig. 5.3 The temperature of the heating element at the maxima of the glow peaks 2, 3, 4 and 5 of TLD-100 for samples of different thickness at three different heating rates.

The value for the thermal conductance of the sample-gas interface H_d can be calculated by Eq. (5.20). For a 0.9 mm thick sample H_d = (8.3 ± 4.3)x10^{-4} J K^{-1} s^{-1}. With the values of C_s, H_c, H_d and T_g it is possible to obtain values for the effective heating rate β', the effective starting temperature T_0' and the temperature lag ΔT. For a 0.9 mm sample the effective heating rate is: $\beta' = 0.964\ \beta$, and the effective starting temperature is: $T_0' = (H_c T_0 + H_d T_g - \beta' C_s)/(H_c + H_d)$ = (0.964 T_0 + 11.8 - 1.77 β) K. If a temperature profile $T_1 = T_0 + \beta t$ is applied then, according to Eq. (5.8), the temperature lag of the sample is:

$$\Delta T = \frac{H_c C_s}{(H_c + H_d)^2}\beta + \frac{H_d (T_1 - T_g)}{(H_c + H_d)} \qquad (5.22)$$

The first term on the right hand side of Eq. (5.22) can be interpreted as a temperature lag caused by a delay between the heating profile of the heating element and the sample. This delay times the heating rate is the temperature lag. The delay is in good approximation proportional to the thickness of the sample. In our case the delay is about 2 s per mm thickness. The second term in Eq. (5.22) can be interpreted as the temperature difference at thermal equilibrium ($dQ_c/dt = dQ_d/dt$) when the heating element is hold at a constant temperature. For thin samples ($L_s d_s << A_s$) this temperature difference is independent of the thickness and is about $1.7 \times 10^{-2}(T_1 - T_g)$. For a LiF:Mg,Ti (TLD-100) sample with dimensions 3.2 x 3.2 x 0.9 mm^3 the temperature lag during the linear heating is $\Delta T = 1.7\beta + 0.037(T_1 - T_g)$.

Table 5.2 Temperatures of the sample at maximum peak intensity T_m of the glow peaks 2, 3, 4 and 5 of TLD-100 for different heating rates. The values of T_m are obtained from an analysis of the temperature of the heating element at the maximum of the peaks versus the thickness of the sample. The errors in T_m are typical ± 1 K

Peak nr.	3.0 K s^{-1}	5.95 K s^{-1}	9.9 K s^{-1}
2	395.0	400.4	402.2
3	436.0	441.0	441.9
4	466.7	470.3	470.7
5	492.8	496.8	497.2

The error in ΔT can be estimated by:

$$\sigma^2(\Delta T) = a + b T_1 + c T_1^2 \qquad (5.23)$$

where the coefficients a, b, and c depend on the heating rate, the sample thickness, the parameters H_c, h_d, T_g, A_s, L_s, c_s, ρ_s and the variances and covariances of H_c, h_d and T_g. For some heating rates and sample thicknesses the values of a, b and c are shown in Table 5.3. These values are obtained by fitting Eq. (5.23) to the errors in the temperature lag as function of T_1. The errors in ΔT

are obtained by the variances and covariances of H_c, h_d and T_g using error propagation (Bevington 1969 p. 56). The error in the temperature lag is about 1 K to 3 K.

Table 5.3 Coefficients for error estimation of the temperature lag for samples with different thickness d and at different heating rates β. The error in the temperature lag is about: $\sigma(T)^2 = a + b\,T_1 + c\,T_1^2$. The coefficients are determined from a fit of $\sigma(T)$ obtained by the variances and covariances of H_c, h_d, and T_g using error propagation. The values of the parameters needed for the calculations are shown in Table 5.1.

	Thickness								
	1.0 mm			0.5 mm			0.2 mm		
β (K s^{-1})	*a*	*b*	*c*	*a*	*b*	*c*	*a*	*b*	*c*
20	93	-0.37	3.7×10^{-4}	45	-0.19	2.0×10^{-4}	26	-0.11	1.2×10^{-4}
10	85	-0.36	3.8×10^{-4}	43	-0.19	2.1×10^{-4}	26	-0.11	1.2×10^{-4}
6	82	-0.35	3.8×10^{-4}	43	-0.19	2.1×10^{-4}	26	-0.11	1.2×10^{-4}
3	81	-0.35	3.8×10^{-4}	43	-0.19	2.1×10^{-4}	26	-0.11	1.2×10^{-4}
1	80	-0.34	3.8×10^{-4}	43	-0.19	2.1×10^{-4}	26	-0.11	1.2×10^{-4}
0.3	80	-0.34	3.8×10^{-4}	43	-0.19	2.0×10^{-4}	26	-0.11	1.2×10^{-4}

5.6 Discussion and Conclusions

The description of the heat transfer with the model used in this chapter shows that the temperature lag can be very large (14 K for β = 6 K s^{-1}, T_2 = 450 K and d_s = 0.9 mm). The temperature lag is mainly caused by two effects: (1) A delay of the temperature profile caused by the heat capacity of the sample and the thermal conductance of the contact layer (about 2 s per mm thickness). (2) A heat flow from heating element to sample to compensate the heat loss to the surroundings causing a contribution to the temperature lag of about $1.7\times10^{-2}(T_1 - T_g)$ K (for $d_s << A_s/L_s$).

For samples less than 1 mm thick, the temperature difference across the sample is small compared to the temperature lag (2 K for β = 6 K s^{-1}, T_2 = 450 K and d_s = 0.9 mm). This result is in agreement with the result of Gotlib *et al* (1984).

Our model for the heat transfer differs from the model used by Gotlib *et al* (1984) in two ways. Firstly, we neglected the temperature gradient in the sample which simplifies the calculations significantly. Secondly we accounted for the contribution of the sides of the sample to the heat transfer surface of the sample-gas interface. For the samples obtained by Harshaw this contribution is over 50% so it cannot be neglected.

The heat transfer coefficient of the sample-gas interface found in our experiment [(38±20) J K^{-1} s^{-1} m^{-2}] is in good agreement with that of Gotlib *et al* (1984) (42 J K^{-1} s^{-1} m^{-2}) and Betts and Townsend (1993) (25 J K^{-1} s^{-1} m^{-2}). However, the heat transfer coefficient of the contact layer h_c obtained by our method [$h_c = H_c/A_s$ = (2.3±0.2)x10^3 J K^{-1} s^{-1} m^{-2}] is 2.7 times greater than obtained by Gotlib *et al* (1984) ($h_c = \lambda_1/R$ = 8.4x10^2 J K^{-1} s^{-1} m^{-2} where λ_1 is the thermal conductivity of the contact layer and R is the thickness of the contact layer in the notation of Gotlib *et al*) and 4-5 times smaller than that obtained by Betts and Townsend (1993) (10x10^3 J K^{-1} s^{-1} m^{-2}). As a consequence our estimated temperature lag is smaller than that of Gotlib *et al* (1984) and greater than that of Betts and Townsend.

The effect of the temperature lag on glow curve analysis is an overestimation of E and s values. The effect of the temperature lag on the analysis of the shape of an emission band is an underestimation of the parameter Cq_0^2.

The real temperature of the sample during heating can be estimated by means of an effective heating rate and an effective starting temperature. The error in this estimation is about 1 to 3 K depending on heating rate, sample thickness and heating element temperature.

Chapter 6

TL emission spectra of some LiF:Mg,Ti samples

Abstract: The TL emission spectra of a LiF:Mg,Ti (TLD-100) sample and three LiF:Mg,Ti samples with different impurity concentrations (0-6 ppm Ti and 80-100 ppm Mg) are measured under different read-out, annealing and irradiation conditions. At a dose less than 22 Gy the emission spectrum of the TLD-100 sample and the sample without Ti comprises one emission band at 420 nm and at 620 nm, respectively. The spectra of the other two samples comprises two emission bands at 420 nm and 620 nm of which the 420 nm band increases with Ti concentration. Another weak emission band at 300 nm was observed which has been associated with an intrinsic defect. The intensity of the 420 nm and 620 nm bands as function of temperature shows four peaks in the temperature range from 350 K to 525 K (when heated at a rate of 6 K s^{-1}). However, there are slight differences in the temperatures at maximum intensities between TLD-100 and the other samples. The behaviour of the intensity of the emission bands as function of temperature appears to be dependent on heating rate and annealing procedure and can be explained by defect reactions. For the samples which comprises two emission bands (420 nm and 620 nm) irradiations to an absorbed dose of 30 kGy introduces new emission bands between 420 nm and 620 nm. The blue emission band is shifted to 395 nm and has become narrower. The dose response of the glow peaks is different for peaks at different temperatures and emission band. From these measurements we conclude that traps and luminescent centres are coupled.

6.1 Introduction

It has been suggested that defect reactions play a major role in the mechanism of TL in LiF doped with Ti and Mg (Grand and Cameron 1966, Taylor and Lilley 1982b, Bos *et al* 1992, chapter 2). The effect of these reactions on TL are usually investigated by the behaviour of the glow curve as a function of annealing procedure and read-out heating rate. The glow curves consist of a number of

glow peaks which are associated with defects which act as trapping centres for charge carriers. The changes in glow peaks as a function of the annealing procedure and heating rate then reflect the changes of concentration of traps due to defect interaction. However, glow curves contain no information about changes in the spectral distribution of the TL emission. Therefore, information about defects which act as luminescent centres is lost. Information about defect reactions concerning luminescent centres can be obtained by studying the TL emission spectrum as a function of annealing procedure, heating rate, linear energy transfer (LET) and dopant concentrations. Earlier investigations into the emission spectrum of LiF:Mg,Ti involved the influence of different dopant concentrations (Townsend *et al* 1983, Crittenden *et al* 1974), different LET (Fairchild *et al* 1978, Townsend *et al* 1983). The difference between emission spectra of samples annealed with different cooling rates in the annealing procedure has also been investigated (Crittenden *et al* 1974). Four emission regions have been observed around 300 nm, 420 nm, 520 nm and 620 nm to 640 nm. The 300 nm emission has been associated with intrinsic defects (Crittenden *et al* 1974) and the 420 nm emission has been associated with the Ti impurity (Townsend *et al* 1983). The origin of the 520 nm and 650 nm emission is uncertain. Townsend *et al* (1983) suggested that the 620 nm emission is due to Mn^{2+} traces. The effect of the length of an ageing period in the annealing procedure and of the read-out heating rate has only been investigated on TLD-100 (Delgado and Delgado 1984, Piters and Bos 1993). Delgado and Delgado (1984) observed no changes in the emission spectra and Piters and Bos observed only very small changes.

In this chapter measurements of TL emission spectra of LiF doped with Mg and Ti are described. The measurements are performed at different read-out heating rates, different annealing procedures and different absorbed doses. The purposes of the measurements described in this chapter are (1) to illustrate the capabilities of the research facility described in chapter 4 and (2) to investigate the behaviour of the different emission bands as a function of read-out heating rate, annealing procedure and absorbed dose in order to get more insight into the TL mechanism. It will be shown that TL emission spectra of LiF:Mg,Ti other than TLD-100 strongly depend on annealing procedure, read-out heating rate and absorbed dose. The observed behaviour of the emission spectrum is explained in terms of defect reactions.

6.2 Materials and methods

Four different samples denoted by A, B, C and D were used. The samples A, B and C are 1 mm thick slices of 2.5 cm long monocrystalline LiF:Mg,Ti bars with a diameter of 3.8 mm. The crystals were grown by the Bridgman method at the University of Groningen with different concentrations of Ti in the range of 0 - 6 ppm (molar fractions). The Mg concentration of the crystals was about 80-100 ppm (molar fraction). The impurities Mg and Ti were added in the form of MgF_2 and TiF_3. Magnesium has been assumed to be distributed uniformly in the crystal (Rossiter *et al* 1970) whereas for Ti a concentration gradient along the growth axes has been found (Rossiter *et al* 1971). Unfortunately, information about the origin of the used samples has been lost so the concentrations of Ti in the individual samples are unknown and had to be determined (Table 6.1).

Table 6.1 Concentration of Ti and Mg in used samples. The values for the Ti concentration in samples A, B and C are determined by optical absorption. The values are about ten times lower than expected. This could be due to oxygen that modifies the absorption centre. The values for Mg and Ti of sample D (TLD-100) are from Jain (1982)

sample	Mg ppm	Ti ppm
A	80-100	0.07
B	80-100	0.4
C	80-100	0.7
D	100-200	10-20

Sample D is a polycrystalline LiF:Mg,Ti (TLD-100) chip with dimensions of 3.2 x 3.2 x 0.89 mm^3 obtained from Harshaw Chemical Company. The Ti and Mg concentrations in TLD-100 have been determined by different authors. Values for the Ti concentration mentioned in the literature: 10-12 ppm (Wachter 1982), 10

ppm (McKeever 1984b) and 10-20 ppm (Jain 1982). Values for the Mg concentration are 170 ppm (McKeever 1984b) and 100-200 ppm (Jain 1982).

The annealing procedures were carried out with a PID (proportional, integral and differential) controlled oven specially designed by NORHOF for TLD experiments or with the oven of the TL facility described in chapter 4. Before each experiment the samples were submitted to a standard annealing procedure in air of 1 hour at (673±1) K (400 °C) followed by quick cooling down. The variation in the annealing procedure is in the length (0 h, 2 h, and 5 h) of a low temperature anneal at (343 ± 1)K (80 °C) given after the standard anneal and before the irradiation (pre-irradiation anneal) or after the irradiation (post-irradiation anneal). Irradiations were carried out with the ^{90}Sr - ^{90}Y β source of the TL research facility described in chapter 4 (for the absorbed doses less than 22 Gy) and with a ^{60}Co source (for the absorbed doses of 30 kGy). The used TL emission reader is described in chapter 4. Four different heating rates were used: 6 K s^{-1}, 1 K s^{-1} and 0.2 K s^{-1}. The TL spectra consist of 126 points taken at regular temperature intervals of 2.7 K (at 6 K s^{-1}), 2.6 K (at 1 K s^{-1}) and 2.8 K (at 0.2 K s^{-1}). For the dose irradiations less than 22 Gy the wavelength resolution of the emission spectra is 29 nm. For the 30 kGy irradiation the resolution is 18 nm (samples B and C) and 6 nm (samples A and D). The emission spectra are analyzed according to the simplified Franck-Condon model described in chapter 3. The analyzing method is described in chapter 4.

After the TL measurements an attempt has been made to determine the Ti concentration in the samples A, B and C by measuring the optical absorption spectra in the 190 nm - 300 nm range of the samples. The optical absorption measurements were performed in a Perkin-Elmer lambda 9 spectrophotometer at the University of Groningen. The samples were polished (grain size: 0.3 μm) to avoid scattering at the sample surface and the measurements were carried out under a dry nitrogen flow.

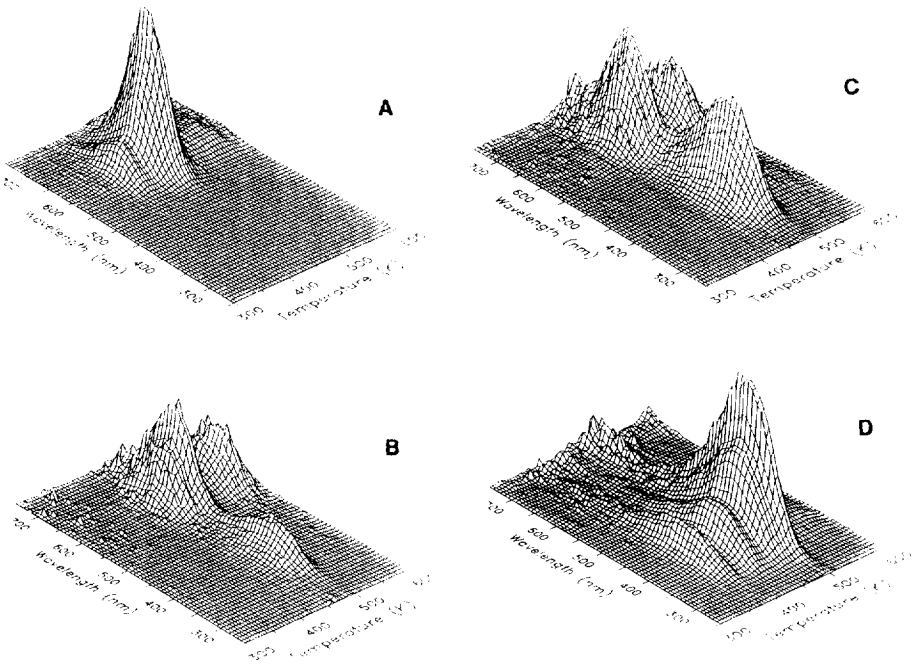

Fig. 6.1 TL emission spectra (number of photons per wavelength and temperature interval) of the samples A, B, C (Groningen) and D (TLD-100). The spectra are corrected for the response of the optical system of the reader. The read-out heating rate is 1 K s^{-1} and the absorbed dose is 10 Gy for the samples A, B and C and 5 Gy for sample D. The ageing time is 0 h.

6.3 Effect of impurity content on emission spectra

Figure 6.1 shows the emission spectra (number of emitted photons per wavelength and temperature interval) of the three Groningen samples A, B, and C and the TLD-100 sample D. The samples were given a standard anneal with the NORHOF oven and irradiated to an absorbed dose of 10 Gy (sample A, B and C) and 5 Gy (sample D). The high noise level at the long wavelength end of the spectral range is a consequence of the insensibility of the detector in this range (see chapter 4).

Three emission regions can be observed at 300 nm, 420 nm and 620 nm. The intensity of the 300 nm emission is very low and is not noticeable in Fig. 6.1. However, in Fig. 6.3 at T = 468 K the 300 nm emission is present. The differences in the spectra of the samples A, B and C are caused by the differences in the concentration of Ti. An indication of the Ti concentration is obtained by the optical absorption spectra of the samples. Fig. 6.2 shows the absorption spectra of sample A, B, and C. The measured data (dots) of samples A, B and C have been fitted simultaneously to a Gaussian shaped absorption band in the energy domain (solid line). The optical absorption shows a peak at 200 nm which has been associated with Ti (Rossiter *et al* 1971, Capelletti *et al* 1987). According to Rossiter *et al* (1971) the height of the 200 nm absorption peak for a concentration of 10 ppm Ti is 3.5 cm^{-1}. If we assume that the height is proportional to the concentration of Ti then from the heights of the absorption bands in Fig. 6.2 we find for the Ti concentrations: 0.07 ppm (sample A), 0.4 ppm (sample B), and 0.7 ppm (sample C) (see Table 6.1). These values are about ten times smaller than expected (we expected values in the range 0-6 ppm). An explanation could be that oxygen has entered the sample during the annealing procedure which could modify the absorption centre (Rossiter *et al* 1971). Nevertheless, it can be seen from Fig. 6.2 that the Ti concentration goes up from sample A to C. This is in agreement with the observed differences of the intensity of the 420 nm emission which is associated with Ti (Townsend *et al* 1983).

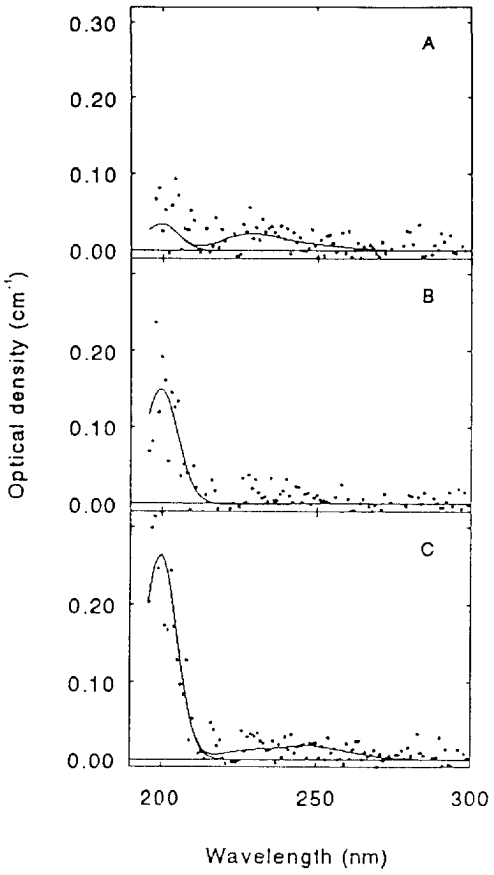

Fig. 6.2 Optical absorption spectra of the samples A, B, and C at room temperature.

6.4 Fitting parameters of the TL emission spectra

The theory of the shape of the emission band of chapter 3 has been applied to describe the emission at low absorbed dose. For the emission around 420 nm good fits were obtained when the spectra for samples B, C and D are described by two emission bands with central photon energies E_0 of 3.0 eV and 2.5 eV. These values for the central photon energies are obtained from previous work on TLD-100 (Piters and Bos 1993). To obtain the other parameters ($2S\hbar\omega = 2Cq_0^2$ and peak content), five emission spectra of sample D at temperatures 407 K, 452 K, 488 K, 515 K and 574 K, recorded at 6 K s^{-1}, have been fitted simultaneously.

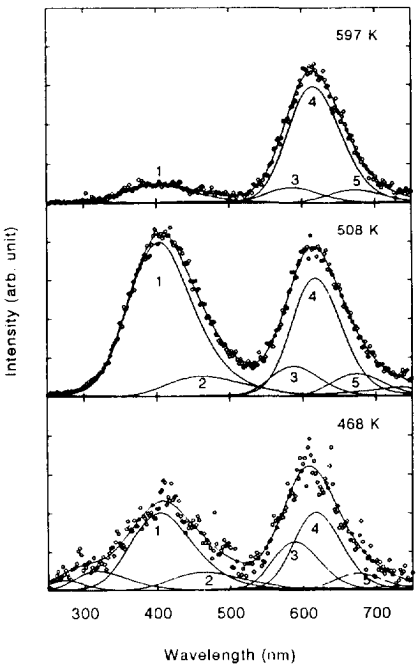

Fig. 6.3 Result of an analysis of the TL emission spectra of sample B. The different bands are fitted according to the simplified Franck-Condon model. The fitting parameters are listed in Table 6.2. The measured spectra are not corrected for the system response of the detector. Instead the fitted emission bands are convoluted according to the system response.

The 620 nm emission can be described by three emission bands with central photon energies of 2.07 eV, 1.98 eV and 1.81 eV. The parameters of these three emission bands are obtained by fitting the 620 nm emission of three spectra

simultaneously (two emission spectra at 387 K and 466 K of sample A heated at a rate of 1 K s^{-1} and one emission spectrum at 433 K of sample C heated at a rate of 6 K s^{-1}). Chi-square of the fit (1340 degrees of freedom) was 1.07. The chi-square distribution for 1340 degrees of freedom is in good approximation equal to the chi-square distribution shown in Fig. 4.10 of chapter 4. If the emission around 620 nm was fitted with two emission bands chi-square was 1.33 which is significantly higher than 1.07 found by the fit with three bands (see Fig. 4.10 in chapter 4). Fits were performed on a Vax-4300 computer using the routine FATAL (Salmon and Booker 1972). The required computation time to obtain the best fits was 5 to 10 minutes. The fitted parameter values are shown in Table 6.2. Figure 6.3 shows the measured and fitted emission spectra at three temperatures of sample B. In Fig. 6.3 only the areas of the emission bands are fitted, the other parameters are from Table 6.2. The fitted parameters may be used to estimate the influence of quenching (see chapter 3). The luminescence efficiency η as defined in chapter 3 is calculated with Eq. (3.27) at T = 600 K where the ratio s_{nr}/s_r in Eq (3.28) is taken 10^6. According to these calculations quenching does not play a significant role for temperatures below 600 K ($\eta(600) \approx 1$). We realize that the fitted emission bands do not necessarily represent the physical phenomenon as assumed by the model. In the model the oscillator strength of the excited state and ground state are equal. If the oscillator strength for the ground state is higher than for the excited state, then the role of quenching will be more important. However, the fitting parameters can be used to characterize the emission spectra.

Table 6.2 Parameters of the emission bands of LiF:Mg,Ti according to the simple version of the Franck-Condon model described in chapter 3.

band	E_0 (eV)	$2S\hbar\omega$ (eV)	E_Q (eV)	$U(T = 450\ K)$ (eV)	λ_{max} (nm)
1	3.00	2.86	1.6	0.33	413
2	2.51	2.26	1.4	0.29	494
3	2.07	0.28	7.6	0.10	599
4	1.98	0.23	8.5	0.094	626
5	1.81	0.19	8.6	0.085	685

6.5 Effect of different thermal treatments

Figure 6.4 and Fig. 6.5 show the glow curves of the two emission regions for samples A, B and C at different read-out heating rates for an ageing period of 0 h (Fig. 6.4) and for an ageing period of 5 h (Fig. 6.5). The glow curves are obtained by adding up the contents of emission bands 1 and 2 for the 420 nm region and emission bands 3, 4, and 5 for the 620 nm region. The contents of each band is fitted at 120 temperatures. The time required for the calculations of a fit at one temperature is about 53 s. The glow curves are corrected for the system response of the detector and are proportional to the number of emitted photons.

In all glow curves of Fig. 6.4 and Fig. 6.5 the low temperature glow peaks can be recognized as peak 2, 3, 4 or 5 of TLD-100. However, their relative heights differ for the glow curves of different emission bands and samples. Furthermore, it is seen that peaks 2 and 3 of sample A for the 620 nm emission are shifted to higher temperatures with respect to the glow peaks of sample D for the 420 nm emission. Sample B and C show a huge high temperature complex while peaks 2 and 3 are relatively low compared to peak 2 and 3 of sample A and D.

For sample B and C aged at 353 K for 5 hours (Fig. 6.5) a remarkable effect of the heating rate is observed for peak 4. With decreasing heating rate peak 4 increases for the 620 nm region and decreases for the 420 nm region.

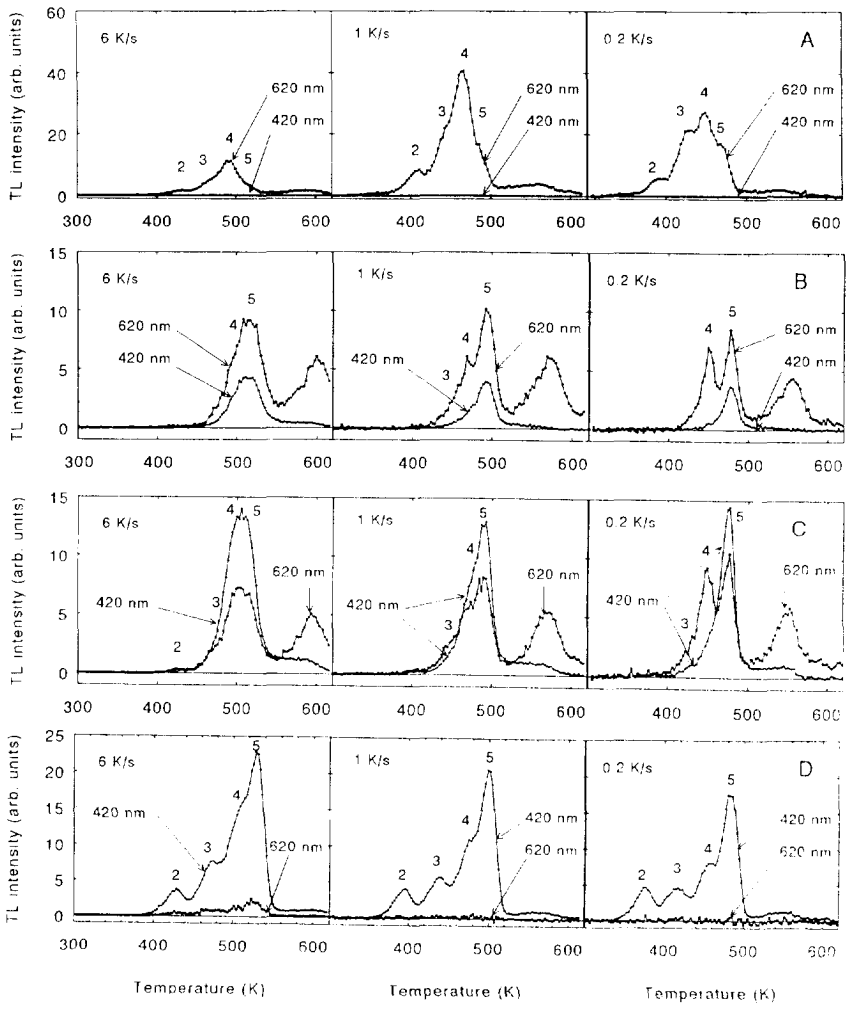

Fig. 6.4 Glow curves of samples A, B, C and D for the 420 nm and 620 nm emission at different read-out heating rates. The ageing time in the annealing procedure is 0 h.

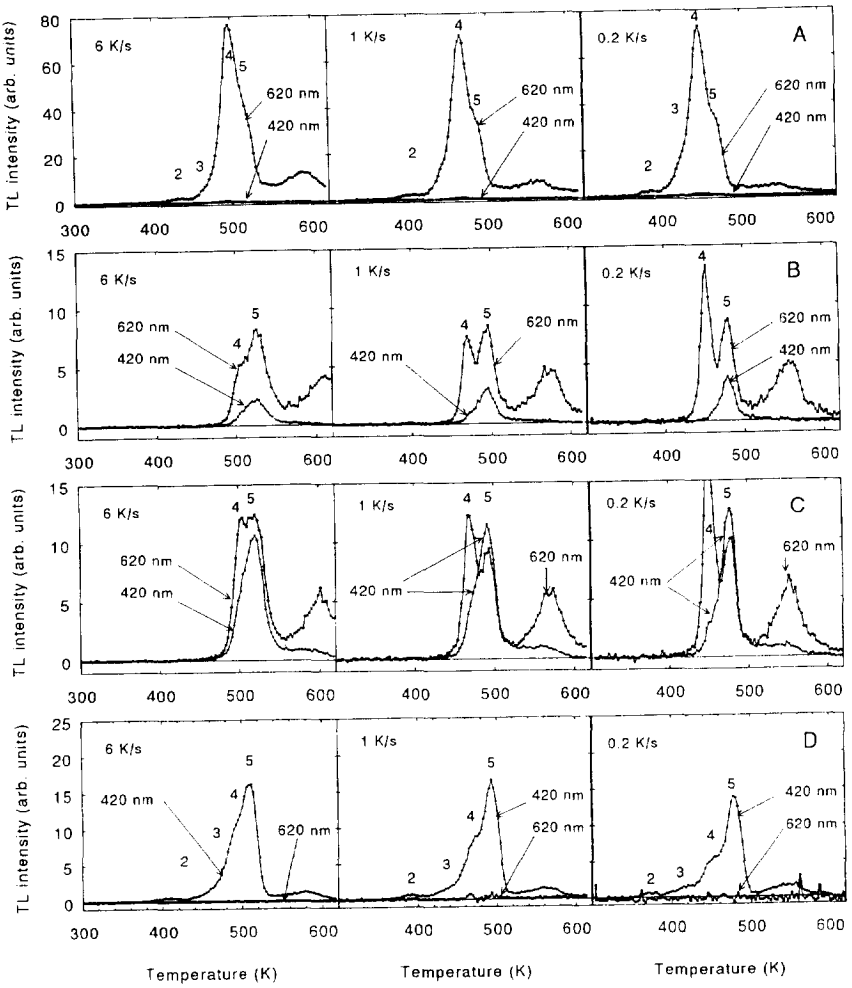

Fig. 6.5 Glow curves of samples A, B, C and D for the 420 nm and 620 nm emission at different read-out heating rates. The ageing time in the annealing procedure is 5 h.

In chapter 2 it has been shown that the behaviour of *glow curves* as a function of heating rate and annealing procedure could be explained by reactions between traps and other defects. Now we try to explain the behaviour of the *emission bands* in terms of defect reactions.

The luminescent centre responsible for the 420 nm emission has been associated with a Ti-complex denoted as TiX which is the product of the reaction:

$$X + Ti \rightarrow TiX \qquad (6.1)$$

The measurements (Fig. 6.1) indeed show an increase of the 420 nm emission when a higher amount of Ti is added. With an increasing amount of Ti in the sample the X concentration decreases due to reaction (6.1). The observations may be explained by assuming that the 620 nm emission is connected to the X concentration. At a molar fraction of 10 ppm Ti the 620 nm emission is not present which indicates that X is not an intrinsic defect or a composition of Mg impurities. Furthermore the absence of the 620 nm emission in the 10 ppm sample (sample D) for different annealing procedures (Fig. 6.4 D and 6.5 D) indicates that the TiX defect is tightly bounded. However, if the 620 nm emission is ascribed only to the X defect one would expect that the ratio of the 420 nm and the 620 nm intensities during the readout is a fixed quantity or monotone decreasing or increasing quantity with time. The observed ratio of the 420 nm and 620 nm intensities is plotted in Fig. 6.7. It is seen that the ratio is certainly not constant or monotone. This suggests that there is another defect involved in the TL process. The strong variations in the 420 nm and 620 nm intensity ratio indicate that this other defect is involved in a number of defect reactions which increase and decrease its concentration. A possible candidate for this other defect could be the $(MgV)_3$ defect which is known to be involved in the defect reactions (Strutt and Lilley 1981):

$$MgV \rightleftarrows (MgV)_3 \rightleftarrows \text{precipitates} \qquad (6.2)$$

The concentrations of MgV and $(MgV)_3$ are dependent on the annealing procedure. For an annealing procedure of 1 hour at 673 K (400 °C) the concentration is high for MgV and low for $(MgV)_3$ and precipitates. A fast cooling down to room temperature freezes this concentration distribution. When an ageing period at 353 K (80 °C) follows, the distribution of defect concentrations changes to the equilibrium distribution at 353 K *i.e.* low concentration of MgV and high concentration of $(MgV)_3$ and precipitates. Peak 5 in the TLD-100 glow curve is usually associated with the $(MgV)_3$ defect which acts as an electron trap (Dryden and Shutter 1973, McKeever 1984a and b, Bos *et al* 1992). If this defect

can also act as a luminescent centre it must be able to capture a hole as well. To explain why $(MgV)_3$ only captures a hole in the presence of X we propose the following mechanism.

During irradiation, the defect X can capture a hole:

$$X + h \rightarrow X^* \qquad (6.3)$$

The defect $(MgV)_3$ does not capture a hole during the irradiation but can react with X^* at temperatures where X is mobile (first part of the read-out cycle) according to:

$$X^* + (MgV)_3 \rightarrow X + (MgV)_3^* \qquad (6.4)$$

It may seem unrealistic that although $(MgV)_3^*$ is a stable defect $(MgV)_3$ cannot capture a hole by itself. With the help of a configuration diagram as defined in chapter 3, this can be explained. Figure 6.6 shows the configuration diagram of $(MgV)_3$ plus a free hole and of $(MgV)_3^*$. The minimal energy of $(MgV)_3^*$ is lower than that of $(MgV)_3$ plus a hole, so $(MgV)_3^*$ is stable. However, the minimal energy is reached at different coordinates. The configuration coordinate of $(MgV)_3$ with the lowest energy is q_0. When a hole passes by, a transition to $(MgV)_3^*$ is very unlikely because the energy of $(MgV)_3^*$ at q_0 is higher than the energy of $(MgV)_3$ plus a free hole.

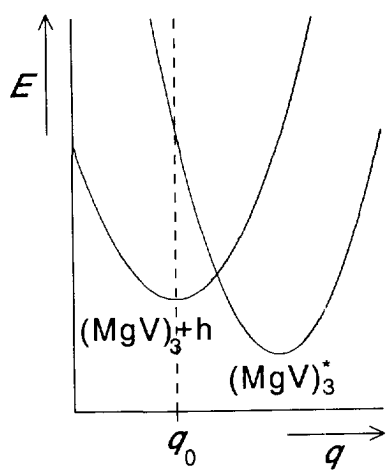

Fig. 6.6 Configuration diagram for the 620 nm emission luminescent centre with potential energy curves as function of the configuration coordinate q for the $(MgV)_3$ plus hole state and the $(MgV)_3^*$ state. The configuration diagram explains why $(MgV)_3$ does not capture a hole during irradiation. The configuration coordinate of $(MgV)_3$ with the lowest energy is q_0. When a hole passes by, a transition to $(MgV)_3^*$ is very unlikely because the energy of $(MgV)_3^*$ at q_0 is higher than the energy of $(MgV)_3$ plus a free hole.

In the following it will be illustrated that the observations of samples B and C shown in Figs. 6.4 and 6.5 may be explained by assuming various defect reactions in which the defects X^*, MgV, $(MgV)_3$, and $(MgV)_3^*$ are involved. The TiX^* is assumed to be not involved in any defect reaction. If we assume that the cross sections for recombination at $(MgV)_3^*$ and TiX^* are similar, the changes in the ratio of the intensity of the 620 nm and 420 nm emission of Fig. 6.7 may be interpreted as the changes in the $(MgV)_3^*$ concentration.

To describe the various defect reactions during the readout, four temperature regions are distinguished (see Fig. 6.7). The behaviour of the emission spectra in these regions can be understood in terms of different defect reactions.

In temperature region I defect X^* becomes mobile and may pass by a defect $(MgV)_3$. At $(MgV)_3$, the defect X^* can carry over the captured hole and form the luminescent centres $(MgV)_3^*$ according to reaction (6.4). The rate of reaction (6.4) depends on the $(MgV)_3$ concentration. Thus when an ageing at 353 K has been applied during the annealing stage (high $(MgV)_3$ concentration) the concentration of $(MgV)_3^*$ at the end of region I of Figs. 6.7 d, e and f will be higher than in the situations of Figs. 6.7 a, b and c where no ageing has been applied. Unfortunately, for sample C aged for 5 hours the intensity is too low to calculate the ratio in region I. A decrease of the heating rate increases the time period in which reaction (6.4) can take place. So for low heating rates the concentration of $(MgV)_3^*$ at the end of region I will be higher than for high heating rates (as can be seen by comparison of Figs. 6.7 a, b and c).

In temperature region II the MgV defects become mobile. They can react according to reaction (6.2). Further, they can react with $(MgV)_3^*$ to form precipitates* according to:

$$(MgV)_3^* + MgV \rightarrow \text{precipitate}^* \qquad (6.5)$$

This reaction lowers the $(MgV)_3^*$ concentration. Simultaneously reaction (6.4) occurs which increases the concentration of $(MgV)_3^*$. So for a high MgV and low $(MgV)_3$ concentration (Figs. 6.7 a, b, c) a decrease of $(MgV)_3^*$ is observed due to a preference of reaction (6.4) and for a low MgV concentration (Figs. 6.7 d, e, f) an increase of $(MgV)_3^*$ is observed due to a preference of reaction (6.5).

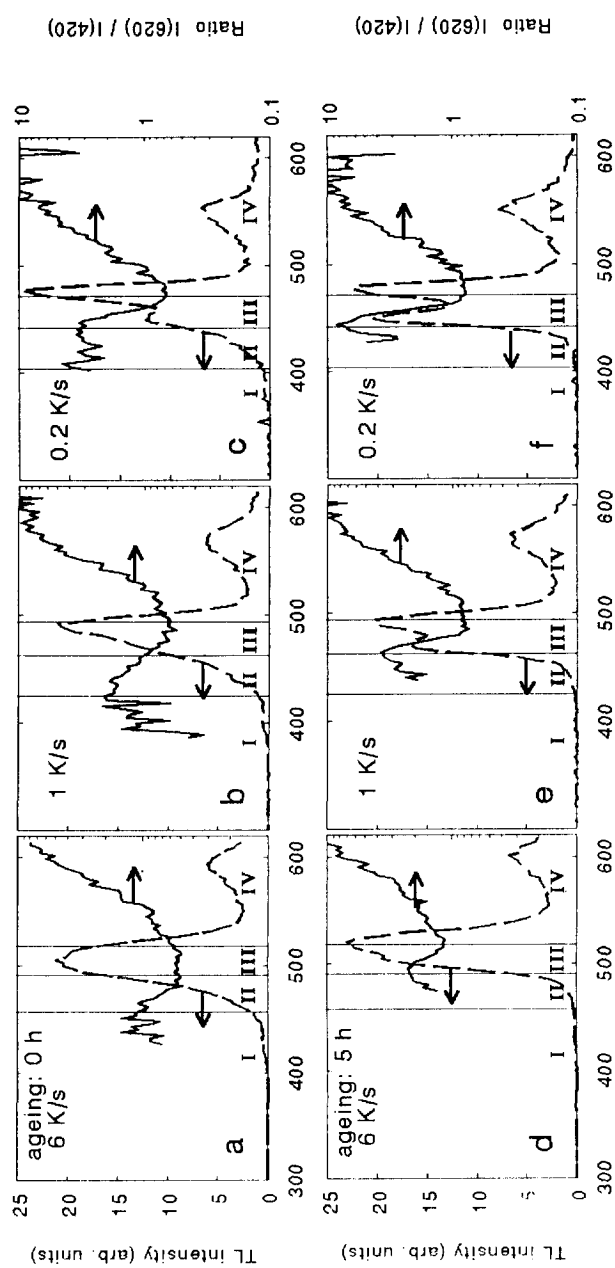

Fig. 6.7. Glow curves of sample C (sum of 420 nm and 620 nm emission) (left y-axis) and the ratio: the intensity of the 620 nm emission band divided by the intensity of the 420 nm band (right y axis) measured at different heating rates (see top-left corner of each graph). The upper figures (a, b and c) correspond to a *pre*-irradiation anneal of 0 hour ageing and the lower figures (d, e and f) to a pre-irradiation anneal of 5 hours ageing. The change in the ratio is interpreted as the change in the $(MgV)_3^*$ concentration responsible for the 620 nm emission, due to defect reactions only. The graphs are divided in four temperature regions in which different processes dominate (see text section 6.5).

In temperature region III the $(MgV)_3$ or $(MgV)_3^*$ defects become mobile and can react with each other according to:

$$(MgV)_3^* + (MgV)_3 \rightarrow \text{precipitate}^* \qquad (6.6)$$

This reaction decreases the concentration of $(MgV)_3^*$. So for a high concentration of $(MgV)_3$ (Figs. 6.7 d, e, f) the $(MgV)_3^*$ concentration decreases more rapidly than for a low concentration of $(MgV)_3$ (Figs. 6.7 a, b, c). Note that peak 4 is located in region III. It could be possible that the mobility of $(MgV)_3$ or $(MgV)_3^*$ plays a role in the TL mechanism of this peak.

The increase of the $(MgV)_3^*$ concentration in region IV may be explained by the dissolution of the precipitates*:

$$\text{precipitates}^* \rightleftarrows (MgV)_3^* + MgV \qquad (6.8)$$

The reaction rates in this temperature region are so high that the concentration distribution follows closely that of equilibrium. So in this region there are no major differences expected between different annealing procedures and read-out heating rates.

The discussion so far has been concerned with annealing procedures *before* irradiation. In Fig. 6.8 the results (ratio and glow curve) are shown of sample C annealed at 353 K for 5 hours *after* irradiation. In this case the observations can also be understood in terms of defect reactions. During the five hours ageing at 353 K the concentrations of MgV_3 and MgV_3^* increase due to reaction (6.2) and reaction (6.4) respectively. So at the end of region I a higher MgV_3^* concentration is seen in this case than in the case of Fig. 6.7 a. During the first part (region I) of the read-out cycle the MgV_3^* concentration in case of Fig. 6.7 a (and Fig. 6.7 d) increases but will stay lower than the MgV_3^* concentration in the case of Fig. 6.8. This is indeed observed (compare the ratios at the beginning of region II of Figs. 6.8 and 6.7 a). In region II of Fig. 6.8 the reactions (6.4) (which increases the MgV_3^* concentration) and (6.5) (which decreases the MgV_3^* concentration) compete with each other. The rate of reaction (6.4) is very low because of a small X^* concentration so that as a result the MgV_3^* concentration decreases (see region II in Fig. 6.8). In region III reaction (6.6) is responsible for a further decrease of the MgV_3^* concentration. In region IV the MgV_3^* concentration increases again due to reaction (6.8).

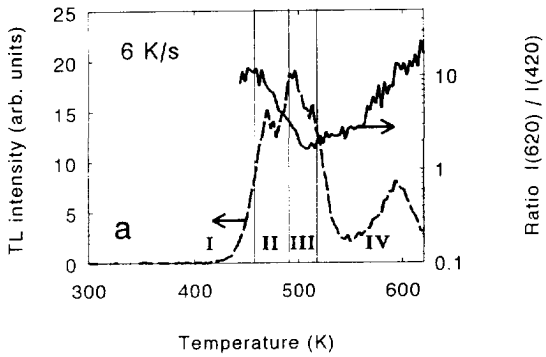

Fig. 6.8 Total glow curve of samples C (420 nm plus 620 nm emission) and the ratio: 620 nm emission divided by 420 nm measured at a heating rate of 6 K s^{-1} and with a post-irradiation anneal of 5 hours ageing. The ratio is interpreted as a measure the $(MgV)_3^*$ concentration responsible for the 620 nm emission, caused by defect reactions only. The change in concentration caused by recombination has no influence on the ratio. The graph is divided in four temperature regions in which different processes dominate (see text section 6.5).

6.6 High dose irradiations

Figure 6.9 shows the emission spectra of heavily irradiated (30 kGy) samples A, B, C and D. The samples were given a standard anneal with the Norhof oven and were read out at 1 K s^{-1}. The TL emission of sample A at 600 K and 620 nm has been dramatically increased with respect to the lower temperature emission (compare the emission spectrum of Fig. 6.9 A with that of the low dose irradiation in Fig. 6.1 A). The spectral distributions of the high and low dose irradiated sample A are similar for the 620 nm band. The spectrum also shows a very low intensity emission in the wavelength range from 365 nm to 525 nm (not notable in Fig. 6.9 A). At 575 K the intensity of this signal is about 1.5 % of the intensity of the 620 nm band. The spectra of sample B and C at high dose (Figs. 6.9 B and C) are very different from the spectra at low dose (Figs. 6.1 B and C). The blue emission band is now much narrower and shifted from 420 nm to 395 nm. Furthermore, the increase of this band at peak 5 (about 500 K when heated at a

rate of 1 K s^{-1}) from sample B to sample C is less significant for the high dose irradiation (13 % of the intensity of sample C) than for the low dose irradiation (52 % of the intensity of sample C). This suggests that the 395 band has another origin than the 420 nm emission band which is seen at low dose irradiation.

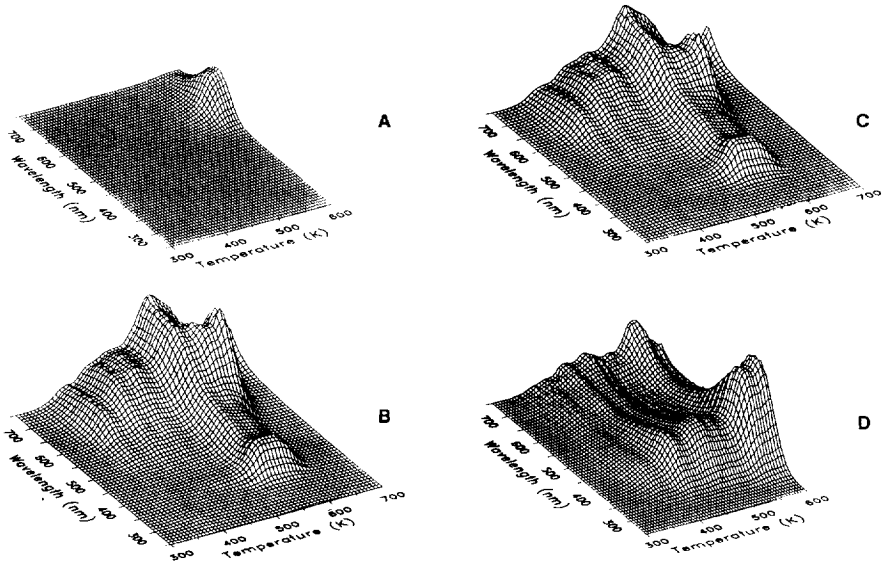

Fig. 6.9 TL emission spectra (number of photons per wavelength and temperature interval) of the samples A, B, C (Groningen) and D (TLD-100). The spectra are corrected for the response of the optical system of the reader. The read-out heating rate is 1 K s^{-1} and the absorbed dose is 30 kGy. The ageing time in the annealing procedure is 0 h (standard anneal).

Between the blue emission band (395 nm) and the red emission band (620 nm) of sample B and C a complex of emission bands is present. To illustrate the complexity of the emission the emission spectra of sample C at 382 K, 533 K and 609 K are simultaneously fitted with ten emission bands. The results are shown in Fig. 6.10 and the parameters used in this fit are shown in Table 6.3. Chi-square reduced of the fit was 10.5. This indicates that the spectrum exists out of more emission bands than shown in Fig. 6.10 (if one assumes that each band can be described by the model of chapter 3). However, attempts to fit the spectra with more bands yielded unrealistic results. Some bands became negative and others became extremely broad (these bands could not exist because they would be quenched at the temperatures considered). At the long wavelength end (750 nm) of the spectrum an emission band is present which is not seen at the low dose irradiation (emission band 10 in Fig. 6.10). This band is also present in the emission spectrum of sample D (the TLD-100 sample with a high concentration of Ti) but does not appear in sample A (with a very low Ti concentration). This suggests that this band is related to Ti defects. Perhaps this band is formed due to the trapping of more than one charge carrier in a Ti related defect during the irradiation. The 420 nm bands of high and low dose irradiations of sample D are similar in shape.

Table 6.3 Parameters of the emission bands according to the simple version of the Franck-Condon model (described in chapter 3) of LiF:Mg,Ti (sample C) irradiated to an absorbed dose of 30 kGy.

band	E_0 (eV)	$2S\hbar\omega$ (eV)	E_Q (eV)	$U(T = 450\ K)$ (eV)	λ_{max} (nm)
1	3.74	4.63	1.5	0.42	332
2	3.21	0.72	7.2	0.167	386
3	3.15	0.43	12	0.129	394
4	2.77	1.33	2.9	0.227	448
5	2.53	0.24	14	0.096	491
6	2.20	0.82	3.0	0.178	563
7	2.07	0.28	7.7	0.10	599
8	1.98	0.23	8.5	0.094	626
9	1.81	0.19	8.6	0.085	685
10	1.57	0.40	3.08	0.125	790

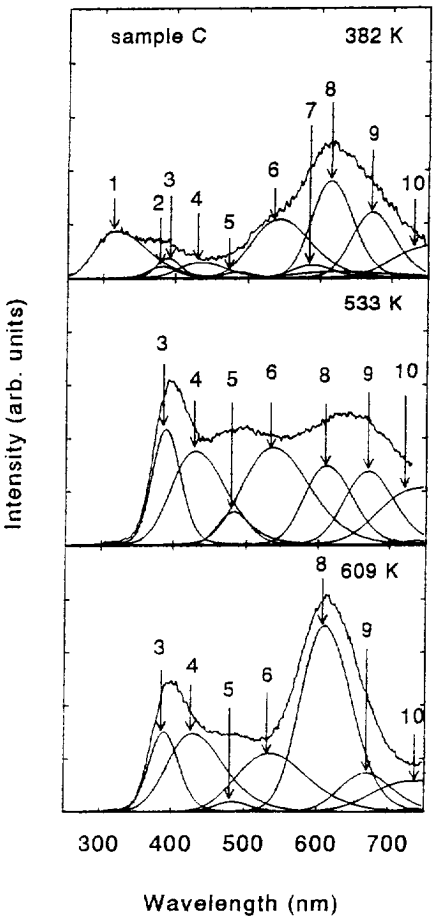

Fig. 6.10 Result of an analysis of the TL emission spectrum of sample C. The different bands are fitted according to the simplified Franck-Condon model. The fitting parameters are listed in Table 6.3. The spectra are not corrected for the system response of the detector. Instead the fitted emission bands are convoluted according to the system response.

6.7 Dose response

After the experiments with the high dose irradiations the dose response of sample A (in the range 1.5 Gy to 11 Gy), sample B and C (in the range 3 Gy to 22 Gy) and of sample D (in the range 0.7 Gy to 5 Gy) was determined. It appeared that the glow curves of the two emission bands of sample A, B and C were slightly altered. The response of the 620 nm emission band was intensified and that of

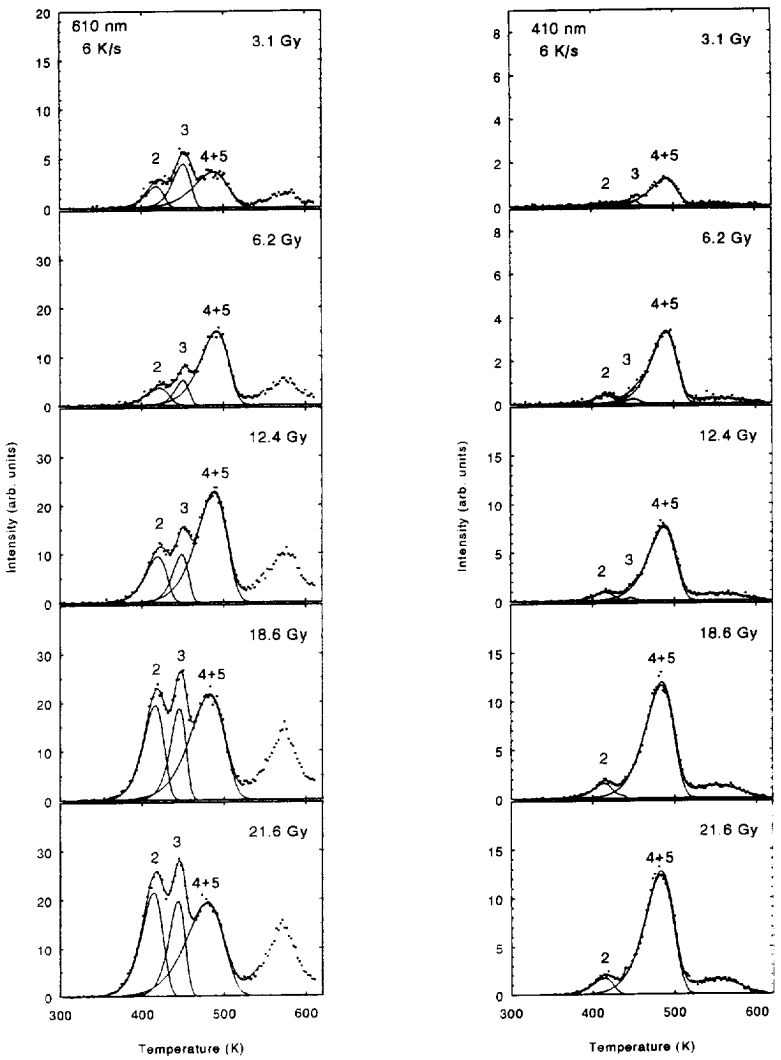

Fig. 6.11 The glow curves of sample C irradiated to different absorbed doses (see right top corner) at 620 nm (left) and 420 nm (right) recorded at a heating rate of 6 K s^{-1}. The glow curves are analyzed with the Randall Wilkins model. The temperature lag due to the thickness of the sample was taken into account. The mean parameter values of the glow curves are shown in Table 6.4.

the 420 nm emission was weakened after the high dose irradiation. Furthermore the low temperature peaks at 620 nm of sample C were more pronounced. Probably some of the irradiation damage did not recover during the annealing procedure.

Figure 6.11 shows the glow curves of the 420 nm emission and 620 nm emission of sample C at different doses. The glow curves were fitted with three peaks: peak 2, peak 3 and a peak denoted by 4+5. The temperature lag due to the imperfect heat transfer has been taken into account. The values of the fitting parameters are shown in Table 6.4. In Table 6.5 data of thin TLD-100 samples irradiated at a low dose is shown. These data come from previous work on the effect of the heating rate on the trapping parameters of TLD-100 (Bos *et al* 1992). It is seen that there are small differences between the results obtained with the modified Harshaw reader and thin samples (0.38 mm) and the reader for TL emission spectra and thick samples (0.9 mm) on the order of 0.1 eV.

Table 6.4 Randall-Wilkins parameters of glow curves of samples A, B, C and D. Read-out heating rate: 6 K s^{-1}. Annealing procedure: 1 hour at 673 K followed by a quick cool.

620 nm emission band									
Peak	Sample A			Sample B			Sample C		
	E (eV)	$^{10}\log(s)$ ($\log(s^{-1})$)	T_{max} (K)	E (eV)	$^{10}\log(s)$ ($\log(s^{-1})$)	T_{max} (K)	E (eV)	$^{10}\log(s)$ ($\log(s^{-1})$)	T_{max} (K)
2	1.32±0.07	15.6±0.9	420	1.05±0.08	12.2±1.3	415	1.17±0.06	13.5±0.4	420
3	-	-	-	-	-	-	1.68±0.05	19±1	450
4+5	1.26±0.02	12.9±0.3	476	1.08±0.02	10.6±0.2	489	1.17±0.14	11±2	492
420 nm emission band									
Peak	Sample D			Sample B			Sample C		
	E (eV)	$^{10}\log(s)$ ($\log(s^{-1})$)	T_{max} (K)	E (eV)	$^{10}\log(s)$ ($\log(s^{-1})$)	T_{max} (K)	E (eV)	$^{10}\log(s)$ ($\log(s^{-1})$)	T_{max} (K)
2	1.25±0.03	15.2±1	405	1.35	9±3	410	1.16±0.06	13.8±0.8	415
3	1.37±0.05	15.2±0.6	445	-	-	-	-	-	-
4	1.7±0.1	18±1	478	-	-	-	-	-	-
5	2.23±0.05	22.0±0.2	507	1.11±0.03	25.1±0.5	488	1.12±0.01	11.2±0.2	485

Table 6.5 Randall-Wilkins parameters of TLD-100. Read-out heating rate: 6 K s^{-1}. Annealing procedure: 1 hour 673 K followed by quick cool. Data is from previous work on the effect of the heating rate on the trapping parameter (Bos *et al* 1992).

Peak	E (eV)	$^{10}\log(s)$ ($\log(s^{-1})$)	T_{max} (K)
2	1.35	16.3	411
3	1.44	15.8	451
4	1.55	15.4	481
5	2.10	21.6	508

The peak areas are used to make the dose response plots of Fig. 6.12, Fig. 6.13, Fig. 6.14 and Fig. 6.15. Peak 6 in Fig. 6.14 and Fig. 6.15 denotes the contents of the high temperature complex at 560 K (see Fig. 6.11). It is seen that the peak areas as function of dose behave very different even when they belong to the same emission band (*e.g.* peak 4+5 and peak 2 of sample C at 620 nm in Fig. 6.15) or the same temperature (*e.g.* peak 4+5 of sample C at 620 nm and 420 nm in Fig. 6.15). In general the intensity of the 420 nm emission behaves more linear to the absorbed dose than the 620 nm emission. The glow peaks of the 620 nm emission show sublinear behaviour (*e.g.* Fig. 6.14 peak 4+5) as well as supralinear behaviour (Fig. 6.15 peak 4+5 and peak 6 and Fig. 6.14 peak 4+5 below 5 Gy). This behaviour is not compatible with the simple idea that luminescence centres and trapping centres are completely uncoupled. If the luminescent and trapping centres were completely uncoupled then the saturation of peak 4+5 would be either due to a saturation of the luminescent centre

responsible for the 620 nm emission or to a saturation of the trap responsible for peak 4+5. In case the 620 nm luminescent centre saturates, it is not possible to explain why peak 2 and 3 of sample C (see Fig. 6.15) are not saturated. In case that the trap responsible for peak 5 saturates it is not possible to explain why peak 5 at the 420 nm emission is not saturated (see Fig. 6.15). So the data of Fig. 6.12 to 6.15 suggest that a coupling between luminescent centres and trapping centres must exist.

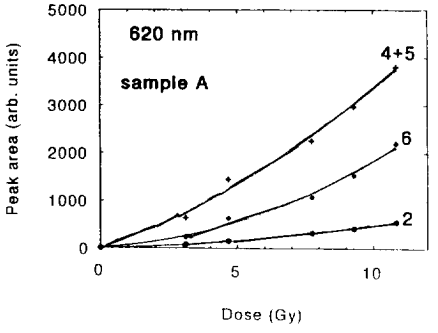

Fig. 6.12. Areas of peak 2 (2), peak 4 + peak 5 (4+5) and of the high temperature complex around 580 K (6) as function of the absorbed dose for sample A. The read-out heating rate was 6 K s^{-1} and the annealing procedure is the standard procedure of 1 hour at 673 K followed by a quick cool.

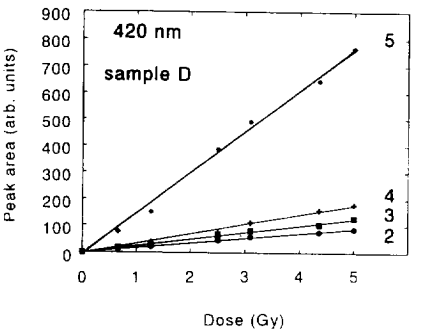

Fig. 6.13. Areas of peak 2 (2), peak 3 (3), peak 4 (4) and peak 5 (5) as function of the absorbed dose for sample D (TLD-100). The read-out heating rate was 6 K s^{-1} and the annealing procedure is the standard procedure of 1 hour at 673 K followed by a quick cool.

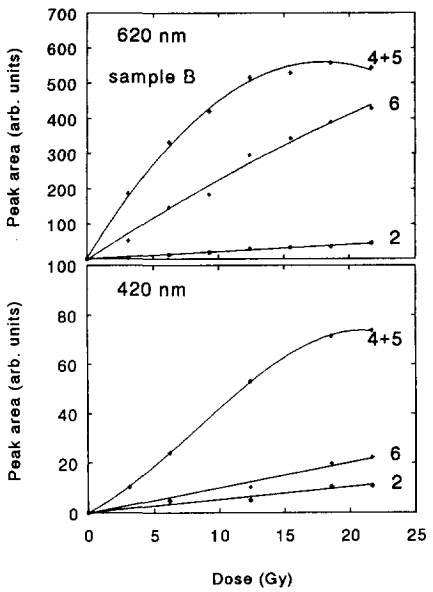

Fig. 6.14. Areas of peak 2 (2), peak 4 + peak 5 (4+5) and of the high temperature complex around 580 K (6) at 420 nm and 620 nm (see left top corner) as function of the absorbed dose for sample B. The read-out heating rate was 6 K s^{-1} and the annealing procedure is the standard procedure of 1 hour at 673 K followed by a quick cool.

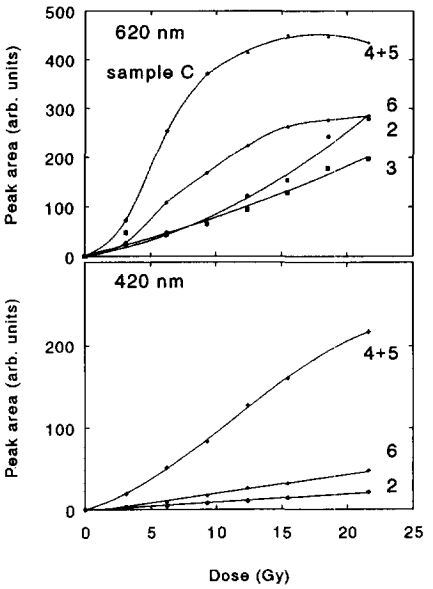

Fig 6.15. Areas of peak 2 (2), peak 3 (3), peak 4 + peak 5 (4+5) and of the high temperature complex around 580 K (6) at 420 nm and 620 nm (see left top corner) as function of the absorbed dose for sample C. The read-out heating rate was 6 K s^{-1} and the annealing procedure is the standard procedure of 1 hour at 673 K followed by a quick cool.

Supralinearity has been explained in terms of competition between radiative recombination and nonradiative recombination as described by Mische and McKeever (1989). In their model the dose response $F(D)$ can be written as:

$$F(D) = \eta n(D)\left(K+(1-K)\frac{S\,m(D)}{\Sigma(D)}\right) \qquad (6.9)$$

where D is the dose, η is an efficiency factor, $n(D)$ is the number of traps filled after irradiation, K is the fraction of traps that are coupled with luminescent centres, S is the cross section for recombination, $m(D)$ is the number of luminescent centres after the irradiation and $\Sigma(D)$ is the sum of all recombination centres after irradiation (including competitors of which the amount may decrease with increasing dose) weighted by their cross section for recombination. When K is close to one the dose response depends only on the increase of the number of filled traps. In this case one expects a linear or sublinear behaviour. In case K is close to zero the response can become supralinear because the ratio (Sm/Σ) may increase with increasing dose due to a saturation in the creation of a recombination centre or a decrease in the concentration competitors appearing in the summation Σ. The difference between the dose response of peak 4+5 and 6 at 620 nm and 420 nm of sample C below 7 Gy (in Fig. 6.15 it is seen that this is supralinear for the 620 nm band and linear for the 420 nm band) may be explained by different fractions K.

6.8. Discussion and conclusions

There is a disagreement between the expected Ti concentration in our samples and the measured concentration of Ti of about a factor 10. This may be due to oxygen that has entered the crystal during the annealing stages.

At a dose level of 10 Gy the measured emission spectra of LiF doped with Mg and Ti show two main emission bands around 420 nm and 620 nm and a low intensity band around 300 nm. This is in agreement with previous observations (Townsend *et al* 1983 and Crittenden *et al* 1974). The spectrum of the TLD-100 sample contains mainly one emission band which is in agreement with the measurements of Townsend *et al* (1982) and Fairchild *et al* (1978) but in disagreement with measurements of Luff and Townsend (1993). At 30 kGy we observe a new emission complex containing several emission bands between the 420 nm and 620 nm and a new band at the long wavelength end (750 nm) of our

spectral range. These results are in close agreement with the observations of Crittenden *et al* (1974) who observed at doses higher than 10 kGy an extra emission band around 520 nm. In addition we observed a change in the shape (narrower for 30 kGy than for 10 Gy) and position (395 nm for 30 kGy and 420 nm for 10 Gy) of the blue emission band.

The shape of the blue emission band of the TLD-100 sample at 30 kGy is similar to the shape at 5 kGy. This is in disagreement with the measurements of Fairchild *et al* (1978) who observed at high dose two emission bands 428 nm and 477 nm at 333 K to 423 K. Such separation between peaks (about 50 nm) would not be unnoticed by our instrument (our TLD-100 spectrum has been measured with a resolution of 6 nm).

We observed a different dose response for peaks at different temperatures and emission bands. From these observations we conclude that luminescent centres and trapping centres are coupled. This conclusion is in agreement with the 'competition during heating' model for supralinearity described by Mische and McKeever (1989). This model assumes a coupling between trap and luminescence centre to explain a linear dose response at low dose. The existence of a coupling is also in agreement with the observation that the TL process in LiF:Mg,Ti (TLD-100) follows first order kinetics at low doses (see chapter 1 and McKeever 1984b).

The evolution of the two main emission bands, 420 nm and 620 nm, with increasing temperature is strongly dependent on the heating rate and the annealing procedure. It is possible to explain qualitatively the different behaviour of the 420 nm and 620 nm emission during the readout by assuming the occurrence of defect reactions. The defects involved are associated with Ti, MgV, and an unknown defect X. The combination of Ti and X is responsible for the 420 nm emission and the trimer $(MgV)_3$ is responsible for the 620 nm emission. A consequence of this interpretation is that $(MgV)_3$ can act as electron trap as well as hole trap. However, during irradiation $(MgV)_3$ can only trap electrons. A hole can be trapped at $(MgV)_3$ by a reaction with a X defect that has trapped a hole during the irradiation. The occurrence of reactions involving luminescent centres even at low temperature is also supported by the observation of Crittenden *et al* (1974) that the 520 nm and 650 nm emission bands caused by a high dose irradiation could be suppressed by a storage at room temperature for 24 hours. They assumed that this suppression is the result of atomic diffusion of defects.

In chapter 2 a model for the influence of defect reactions during the readout

on the glow curve has been described. In that chapter trapping centres were involved in the defect reactions. The results of this chapter suggest that reactions involving luminescent centres occur as well. The results also suggest that luminescent centres and trapping centres are coupled so that a reaction with a luminescent centre implies a reaction with a trapping centre.

Our model which describes the change of the ratio between intensities of the 620 nm and 420 nm band assumes that the defect associated with the 420 nm emission is not involved in any defect reaction during the readout. This assumption conflicts with our conclusion about the coupling between the trap and luminescent centre (this chapter) and the assumption of the occurrence of reactions involving traps (chapter 2). Probably there are much more processes simultaneously active during the readout. However, the description of the processes in this chapter give some insight into the important role of defect reactions.

The emission spectra of LiF:Mg,Ti samples read out at different heating rates and annealed at different pre-irradiation and post-irradiation annealing procedures show great differences. Therefore, this kind of measurements is very useful for obtaining information about the mechanism responsible for the TL production in LiF:Mg,Ti. However, the interpretation of these measurements is not straight forward because the differences in the emission spectra can be caused by more than one process.

APPENDIX A

Calculation of the integral $\int P(E,q)dE$

In this appendix it is shown that the probability $P(q)$ of finding the excited state of a luminescent centre at a certain configuration coordinate q, is a Gauss function in q. $P(q)$ is an integral of $P(E,q)$ over all vibration levels. Based on the expression for $P(E,q)$ the integral is evaluated:

$$\int_{W_e(q)}^{\infty} P(E,q)\,dE = \frac{\displaystyle\int_{W_e(q)}^{\infty}\left[\frac{\exp(-E/kT)}{\pi\sqrt{E_v/C_e - q^2}}\right]dE}{\displaystyle\int_{E_e}^{\infty}\exp(-E/kT)dE} \qquad \text{(A.1)}$$

where E is the total energy of the excited state at a certain vibration level, E_v the vibration energy, W_e the potential energy at a certain configuration coordinate, E_e the electronic excitation energy and C_e the force constant of the excited state. With the relation $E = E_v + E_e$ and by adjusting the integration boundaries this expression can be simplified by:

$$\int_{W_e(q)}^{\infty} P(E,q)\,dE = \frac{\displaystyle\int_{W_e(q)-E_e}^{\infty}\left[\frac{\exp(-E_v/kT)}{\pi\sqrt{E_v/C_e - q^2}}\right]dE_v}{\displaystyle\int_{0}^{\infty}\exp(-E/kT)dE} \qquad \text{(A.2)}$$

Substitution of

$$\begin{aligned} E_v &= kTx + C_e q^2 \\ W_e(q) - E_e &= C_e q^2 \\ \int_0^{\infty}\exp(-E/kT)\,dE &= kT \end{aligned} \qquad \text{(A.3)}$$

into equation (A.2) gives:

$$\int_{W_e(q)}^{\infty} P(E,q)\,dE = \frac{\exp\left(-C_e q^2 / kT\right)}{\pi\sqrt{kT / C_e}} \int_0^{\infty} \frac{\exp(-x)}{\sqrt{x}}\,dx \qquad \text{(A.4)}$$

The integral in this equation can be solved:

$$\int_0^{\infty} \frac{\exp(-x)}{\sqrt{x}}dx = 2\int_0^{\infty} \exp(-u^2)du = \sqrt{\pi} \qquad \text{(A.5)}$$

Substitution of Eq. (A.5) into Eq. (A.4) gives:

$$\int_{W_e(q)}^{\infty} P(E,q)\,dE = \frac{\exp\left(-C_e q^2 / kT\right)}{\sqrt{\pi kT / C_e}} \qquad \text{(A.6)}$$

This is a Gauss function in q.

APPENDIX B

Temperature inhomogeneity in sample and heating element

In this appendix the temperature differences between bottom and top of the thermoluminescent samples and the heating element during linear heating are estimated. To simplify the calculations it is assumed that all energy transfer takes place in one direction from bottom to top. Figure B.1 shows the situation.

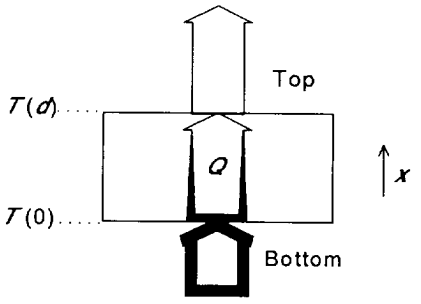

Fig. B.1. Heat transfer through sample or heating element. $T(d)$ denotes the temperature at the top and $T(0)$ denotes the temperature at the bottom. The arrows denote the energy flux dQ/dt. At the bottom of the sample, the energy flux is largest (thick arrow). from bottom to top the energy flux decreases due to the heating of the sample.

The sample or heating element is heated from the bottom and dissipates heat at the top. The temperature inside the sample or heating element is described by the following differential equation:

$$\frac{dT}{dt} = a\frac{d^2T}{dx^2} \qquad \text{(B.1)}$$

where a is the thermal diffusivity. The heating rate dT/dt of the sample is assumed to be equal to the effective heating rate β'. Differences in heating rate across the sample are neglected (this leads to a slight overestimation of the

temperature difference between bottom and top). So Eq. (B.1) becomes:

$$\frac{d^2T}{dx^2} = \frac{\beta'}{a} \qquad \text{(B.2)}$$

The solution of eq (B.2) is:

$$T(x) = \frac{\beta'}{2a}x^2 + \gamma x + T(0) \qquad \text{(B.3)}$$

Where γ can be determined from the condition that the rate of heat transfer at $x = d$ is:

$$\frac{dQ_d}{dt} = H_d\,(T(d) - T_g) \qquad \text{(B.4)}$$

This is also equal to:

$$\frac{dQ_d}{dt} = -\frac{dT(d)}{dx}kA \qquad \text{(B.5)}$$

where k is the thermal conductivity and A is the heat transfer area. So the temperature gradient at $x = d$ is:

$$\frac{dT(d)}{dx} = \frac{h_d\,(T_g - T(d))}{k} \qquad \text{(B.6)}$$

where h_d is the heat transfer coefficient. Differentiating Eq. (B.3) at $x = d$ gives:

$$\frac{dT(d)}{dx} = \frac{\beta'}{a}d + \gamma \qquad \text{(B.7)}$$

Comparing Eq. (B.6) with Eq. (B.7) gives:

$$\gamma = -\frac{\beta'}{a}d - \frac{h_d(T(d) - T_g)}{k} \qquad \text{(B.8)}$$

Substitution of Eq. (B.8) into Eq. (B.3) gives for the temperature at $x = d$:

$$T(d) = T(0) - \frac{\beta'}{2a}d^2 - \frac{h_d(T(d) - T_g)}{k}d \qquad \text{(B.9)}$$

The temperature difference between top and bottom $\delta T = T(0) - T(d)$ is:

$$\delta T = \frac{\beta'}{2a} d^2 + \frac{h_d (T(d) - T_0)}{k} d \qquad \text{(B.10)}$$

For a heating rate of 6 K s^{-1} and at a temperature of 450 K, the temperature difference between top and bottom of a 0.9 mm thick LiF sample δT_s and of the 3 mm thick heating element δT_h can be calculated using Eq. (B.10) and the values from Table 5.1, giving the results: δT_s = 2.0 K and δT_h = 0.3 K.

Bibliography

Agullo-Lopez F, Catlow C R A, Townsend P D 1988 *Point Defects in Materials, Academic Press, Londen*

Attix F H 1986 *Introduction to Radiological Physics and Radiation Dosimetry, John Wiley and Sons, New York*

Bakas G V 1984 *Radiat. Prot. Dosim.* **9** 301

Balian H G and Eddy N W 1977 *Nucl. Instr. Meth.* **145** 389

Bevington P R 1969 *Data Reduction and Error Analysis for the Physical Sciences, McGraw-Hill, New York*

Böhm M and Scharmann A 1981 *Applied Thermoluminescence Dosimetry, Eds Oberhofer M and Scharmann A, ECSC, EEC, EAEC, Brussels and Luxembourg* 11

Bos A J J 1988 *Proceedings of the Symposium on Thermoluminescence Dosimetry, Eds Aalbers A H L, Bos A J J and Mijnheer B J, NCS report 3, Bilthoven* 5

Bos A J J and Dielhof J B 1991 *Radiat. Protec. Dosim.* **36** (4) 231

Bos A J J and Piters T M 1993a *Nucl. Tracks and Radiat. Meas.* **21** 163

Bos A J J and Piters T M 1993b *Radiat. Prot. Dosim.* **47** 41

Bos A J J, Vijverberg R N M, Piters T M and McKeever S W S 1992 *J. Phys. D: Appl. Phys.*

Busuoli G 1981 *Applied Thermoluminescence Dosimetry, Eds Oberhofer M and Scharmann A, ECSC, EEC, EAEC, Brussels and Luxembourg* 83

Capelletti R, Mora C and Ruani G 1987 *Cryst. Latt. Def. and Amorph. Mat.* **16** 153

Chen R 1984 *Thermoluminescence and Thermoluminescent Dosimetry, Ed. Horowitz Y S, CRC Press, Boca Raton* **1** 49

Crittenden G C, Townsend P D, Gilkes J and Wintersgill M C 1974 *J. Phys. D: Appl. Phys.* **7** 2410

Daniels F Boyd C A and Saunders D F 1953 *Science* **117** 343

Delgado A Gomez Ros J M and Muniz J L 1991 *J. Phys. D: Appl. Phys.* **24** 1126

Delgado L and Delgado A 1984 *J. Appl. Phys.* **55** 515

DeWerd L A and Stoebe T G 1972 *Phys. Med. Biol.* **17** 187

Dryden J S and Shuter B 1973 *J. Phys. D: Appl. Phys.* **6** 123

Fairchild R G, Mattern P L, Lengweiler K and Levy P W 1978 *J. Appl. Phys.* **49** 4512

Garlick G F J and Gibson A F 1948 *Proc. Phys. Soc.* **60** 574

Gotlib V I, Kantorovich L N, Grebenshicov V L and Nemiro E A 1984 *J. Phys. D: Appl. Phys.* **17** 2097
Grant R M and Cameron J R 1966 *J. Appl. Phys.* **37** 3791
Haschberger P 1991 *Appl. Radiat. Isot.* **42** 797
Horowitz Y S 1982 *Phys. Stat. Sol. (A)* **69** K29
Horowitz Y S 1984 *Thermoluminescence and Thermoluminescent Dosimetry, Ed. Horowitz Y S, CRC Press, Boca Raton* **1**, 1
Huntly P J, Gotfrey-Smith P I, Thewalt M L W, and Berger G W 1988 *J. Luminesc.* **39** 123
Jacobs P W M and Menon A K 1971 *J. Chem. Phys.* **55** 5357
Jain V K 1982 *Radiat. Prot. Dosim.* **2** 141
Jain V K, Kathuria S P and Ganguly A K 1975 *J. Phys. C: Solid State Phys.* **8** 2191
Jansen A I 1977 *BINAS, Wolters Noordhoff, Groningen*
Johnson R P 1939 *J. Opt. Soc. Am.* **29** 387
Julius H W and de Planque G 1984 *Radiat. Prot. Dosim.* **6** 253
Kanemaki M, Ninawa K, Yamamoto I, Nakagawa M, Wada T, Yamashita Y and Endo K 1991 *Nucl. Tracks and Radiat. Meas.* **18** 81
Kantorovich L M Fogel G M and Gotlib V I 1990 *J. Phys. D: Appl. Phys.* **23** 1219
Kirsh Y 1992 *Phys. Stat. Sol.* **129** 15
Kitis G Spiropulu M Papadopoulos J and Charalambous S 1993 *Nucl. Instrum. Meth.* **B73** 367
Lax M 1952 *J. Chem. Phys.* **20** 1752
Levy P W 1984 *Nucl. Instr. Meth.* B1 436
Lewandowski A C and McKeever S W S 1991 *Phys. Rev. B* **43** 8163
Luff B J and Townsend P D 1992 *Meas. Sci. Technol.* **3** 65
Mahesh K, Weng P S and Feretta C 1989 *Thermoluminescence in Solids and its Applications, Nuclear Technology Publishing, Ashford.*
Martin B R 1971 *Statistics for Physicists, Academic Press* p. 85-98
Metha S K Merklin J F and Donnert H J 1977 *Phys. Stat. Sol. (A)* **44** 679
McKeever S W S 1984a *Radiat. Prot. Dosim.* **8** 3
McKeever S W S 1984b *J. Appl. Phys.* **56** 2883
McKeever S.W.S 1985 *Thermoluminescence of Solids, University Press, Cambridge*
Mische E F and McKeever S W S 1989 *Radiat. Prot. Dosimetry* **29** 159
Moelwyn-Hughes E A 1971 *The Chemical Statics and Kinetics of Solutions, Academic Press, Londen*
Moharil S V 1980 *Sol. St. Commun.* **33** 697
Nink R and Kos H J 1976 *Phys. Stat. Sol. (A)* **35** 121

Perry J H and Chilton C H 1973 *Chemicals Engineers' Handbook, McGraw-Hill, New York*

Piters T M and Bos A J J 1991 *Radiat. Effects Defects Sol.* **119-121** 69

Piters T M and Bos A J J 1993 *Radiat. Prot. Dosim.* **47** 91

Piters T M and Bos A J J (..) *J. Phys. D: Appl. Phys.* (submitted)

Piters T M, Bos A J J and Zoetelief J 1992 *Radiat. Prot. Dosim.* **44** 305

Piters T M, Meulemans W H and Bos A J J 1993 *Rev. Sci. Instr.* **64** 109

Prescott J R, Fox P J, Akbar R A, and Jensen H E 1988 *Appl. Opt.* **27** 3496

Press W H, Flannery B P, Teukolsky S A and Vetterling W T 1988 *Numerical Recipes, Cambridge University Press*

Randall J T and Wilkins M H F 1945 *Proc. Roy. Soc. Lond.* **184** 366 and 390

Rossiter M J, Rees-Evans D B and Ellis S C 1970 *J. Phys. D: Appl. Phys.* **3** 1816

Rossiter M J, Rees-Evans D B, Ellis S C and Griffiths J M 1971 *J. Phys. D: Appl. Phys.* **4** 1245

Sagastibelza F and Alvarez Rivas J L 1981 *J. Phys. C: Solid State Phys.* **14** 1873

Salmon L and Booker D V 1972 *Report* No. AERE-R 7129, Harwell Laboratory, Oxfordshire

Schulman J H, and Compton W D 1963 *Color Centers in Solids, Pergamon Press, Oxford*

Strutt J E and Lilley E 1981 *J. Phys. Chem. Solids* **42** 943

Tale I, Tale V and Nagornyi A 1990 *Radiat. Prot. Dosim.* **33** 71

Taylor G C and Lilley E 1978 *J. Phys. D: Appl. Phys.* **11** 567

Taylor G C and Lilley E 1982a *J. Phys. D: Appl. Phys.* **15** 1243

Taylor G C and Lilley E 1982b *J. Phys. D: Appl. Phys.* **15** 1253

Taylor G C and Lilley E 1982c *J. Phys. D: Appl. Phys.* **15** 2053

Townsend P D, Ahmed K, Chandler P J, McKeever S W S and Witlow H J 1983 *Radiat. Eff.* **72** 245

Townsend P.D and Kirsh Y 1989 *Contemp. Phys.* **30** 337

Touloukian Y S 1970 *Thermal Conductivity Nonmetalic Solids, IFi/Plenum, New York*

Vana N and Ritzenger 1983 *Radiat. Prot. Dosim.* **6** (1-4) 29

de Vries W Hoogenboom J E Dielhof J B and Bos A J J 1988 *Proc. Symp. Thermoluminescence Dosimetry* NCS report 3, Bilthoven 31

Wachter W 1982 *J. Appl. Phys.* **53** 5210

Weast R C, Selby S M and Hodgman C D 1965 *Handbook of Chemestry and Physics, Chemical Rubber Publishing Company, Cleveland*

Wichmann E H 1971 *Quantum physics, Berkeley physics course volume 4, McGraw-Hill book company, New York*

Yeh S H and Weng P S 1991 *Radiat. Eff. Def. Sol.* **116** 353
Yossian D Mahajna S Ben-Shachar B and Horowitz Y S 1993 *Radiat Protec. Dosim.* **47** 129

Summary

A STUDY INTO THE MECHANISM OF THERMOLUMINESCENCE IN A LiF:Mg,Ti DOSIMETRY MATERIAL

Thermoluminescence (TL) is the phenomenon of light emission from an insulator or semiconductor when it is heated after a previous absorption of energy from ionising radiation. During the irradiation an amount of energy is stored in the material. When the material is heated this energy is released in the form of light. An important application of this phenomenon is found in the dosimetry and in particulary personal dosimetry where thermoluminescent materials are used as solid state dosimeters. The most used thermoluminescent material in personal dosimetry is LiF doped with Mg (200 ppm) and Ti (10 ppm) (trade name: TLD-100). It appears that TL in this material is very dependent on the thermal history and the heating rate during the read out. The mechanism responsible for these dependencies is not well understood. The purpose of the research described in this thesis is to get more insight into the mechanism of TL in LiF:Mg,Ti.

Thermoluminescence in LiF is frequently described by the Randall-Wilkins (RW) model. In this model the amount of released energy in a small time interval during heating is proportional to the amount of stored energy times a Boltzmann factor [$s \exp(-E/kT)$ where T is the temperature] times the length of the small time interval. The intensity of the emitted light is proportional to the amount of released energy. With this model the intensity of the light emission as a function of temperature (glow curve) during a read out can be very well described. However, the values of the parameters s and E in the Boltzmann factor have to be chosen different for different thermal procedures. In chapter 2 a model (referred to as the interactive defect (ID) model) is described which explains this dependence. In the ID model stored energy can be released by more than one process. In the simplest case there are two processes of which the rates are proportional to $s \exp(E/kT)$ and to $s' \exp(E'/kT)$. The first process leads to light production but the second process does not. It is shown that the ID model can explain why the RW parameters s and E are dependent on thermal procedures and Ti and Mg concentration, and why they could be higher than expected from general physical principles. Moreover the ID model explains why fading rates (the release of energy when stored at room temperature) are faster than expected from the RW parameters s and E.

The TL emission spectrum contains information about the concentration of different luminescent centres. Furthermore, the width and central photon energy

of an emission band can reveal information about the luminescence efficiency. In chapter 3 a model for the shape of the emission band is described. In this model the lattice vibrations are classically treated and the electronic transitions are assumed instantaneously. In this model the emission band appears to be a Gauss function of the photon energy. The central emission energy is temperature independent and the width is proportional to the square root of the temperature.

The TL light intensity of samples irradiated at dose levels as low as commonly occur in personal dosimetry are so low (μGy) that TL measurements are usually restricted to measurements of the luminescence integrated over all wavelengths so that the spectral information is lost. An important purpose of the work described in this thesis has been the construction of a TL research facility containing a sensitive emission spectrometer, an annealing oven and a β-irradiator. In chapter 4 the TL research facility is described. The spectrometer is based on a dispersive grating and an intensified diode array (512 elements) and covers the 200-800 nm wavelength range. The wavelength resolution of the spectrometer is 6 nm when a 25 μm wide entrance slit is used and 29 nm when a 1 mm wide entrance slit is used. The spectrometer could measure emission spectra of LiF:Mg,Ti (TLD-100) irradiated at an absorbed dose as low as 75 mGy at a signal to noise ratio of 10:1. A detailed description is given how the measured data can be related to spectra predicted by a model, taking into account all detection system aberrations.

An essential part of TL measurements concerns the heating of the sample during the read out. Due to non-ideal thermal contact between sample and heating element it is inevitable that there is a temperature difference between sample and heating element. In chapter 5 a simple model for heat transfer is used to estimate the temperature lag of the sample and errors made in the analysis of the emission spectra and glow curve. In the estimation of the temperature lag the non-uniformity of the temperature inside the sample could be neglected. The temperature lag of a LiF sample with dimensions 3.2x3.2x0.9 mm^3 is about $\Delta T = 1.7\beta + 0.037(T_1 - T_g)$ where T_1 is the temperature of the heating element, T_g is the temperature of the surroundings and β is the heating rate.

In chapter 6 results of measurements of TL emission spectra of a LiF:Mg,Ti (TLD-100) sample and three LiF:Mg,Ti samples with different impurity concentrations (0-6 ppm Ti and 80-100 ppm Mg) at different read out, annealing procedure and irradiation dose are described. At dose levels less than 22 Gy the emission spectra of the TLD-100 sample and the sample without Ti comprise one emission band at 420 nm and 620 nm, respectively. The TL emission spectra of the other two samples comprise two emission bands at 420 nm and 620 nm. The

ratio of the intensities of the two bands vary with temperature during the read out. This behaviour is dependent on the thermal procedure. These dependencies are explained in terms of defect reactions. The glow peaks at different emission bands show different dose response. This observation suggest that the place where the energy is stored and where TL is produced are spatially closely connected.

Samenvatting

EEN ONDERZOEK NAAR HET MECHANISME VAN THERMOLUMINESCENTIE IN EEN LiF:Mg,Ti DOSIMETRIE MATERIAAL

Thermoluminescentie is het verschijnsel dat een isolator of halfgeleider licht uitzendt tijdens verwarming nadat het met ioniserende straling is bestraald. Tijdens de bestraling wordt er een hoeveelheid energie opgeslagen die er tijdens de verhitting weer in de vorm van licht uitkomt. Een belangrijke toepassing van dit verschijnsel is het gebruik van thermoluminescentiemateriaal als dosismeters in de dosimetrie en in het bijzonder in de persoonsdosimetrie. Het meest gebruikte thermoluminescentie materiaal in de persoonsdosimetrie is LiF verontreinigd met Mg (200 ppm) en Ti (10 ppm). Het blijkt dat thermoluminescentie in dit materiaal erg afhankelijk is van de thermische geschiedenis van het materiaal. Het mechanisme dat verantwoordelijk is voor deze afhankelijkheid is niet goed begrepen. Het doel van dit onderzoek is meer inzicht te krijgen in het mechanisme van thermoluminescentie in LiF:Mg,Ti.

Thermoluminescentie wordt vaak met het Randall-Wilkins (RW) model beschreven. In dit model is de hoeveelheid tijdens de verhitting vrijgekomen energie per tijdsinterval rechtevenredig met de hoeveelheid opgeslagen energie maal een Boltzmannfactor [$s \exp(E/kT)$ waarin T de temperatuur is] maal de duur van het tijdsintervalletje. De hoeveelheid licht die wordt geëmitteerd tijdens de verhitting is recht evenredig met de hoeveelheid vrijgekomen energie. Met dit model kan de lichtintensiteit gedurende de verhitting als functie van de temperatuur (gloeicurve) zeer goed worden beschreven. Echter de parameter waarden s en E in de Boltzmann factor moeten anders worden gekozen bij verschillende thermische procedures. In hoofdstuk 2 wordt een model beschreven (het interactief defecten (ID) model) dat deze afhankelijkheid verklaart. In het ID model kan de opgeslagen energie vrijkomen door meer dan één proces. In het eenvoudigste geval zijn er twee processen waarvan de reactiesnelheden rechtevenredig zijn met $s \exp(E/kT)$ en $s' \exp(E'/kT)$. Alleen het eerste proces leidt tot de produktie van zichtbaar licht. Met dit model kan worden verklaard waarom de RW parameters afhankelijk zijn van verschillende thermische behandelingen, Ti en Mg concentraties en waarom de RW parameters s en E hoger kunnen zijn dan verwacht op grond van algemene fysische principes. Het model verklaart ook waarom *fading* (het vrijkomen van energie gedurende opslag bij kamertemperatuur) veel sneller verloopt dan voorspeld met de RW parameters.

Het TL emissiespectrum bevat informatie over de concentratie van

verschillende luminescentiecentra. Uit de breedte en positie van de emissieband kan iets worden afgeleid over de efficientie van de luminescentie. In hoofdstuk 3 wordt een model voor de vorm van een emissie band beschreven. In dit model worden de roostertrillingen klassiek behandeld. De elektronische overgangen worden verondersteld zeer snel plaats te vinden. De vorm van een emissieband blijkt volgens dit model een Gaussfunktie van de fotonenergie te zijn. De centrale fotonenergie is temperatuur onafhankelijk en de breedte van de emissieband is evenredig met de wortel van de absolute temperatuur.

De intensiteit van de thermoluminescentie van monsters die bestraald zijn tot dosisniveau's zoals die voorkomen in de persoonsdosimetrie, is zo laag dat TL metingen beperkt blijven tot het meten van het TL signaal geïntegreerd over alle golflengtes zodat de spectrale informatie verloren is. Een belangrijk doel van het onderzoek beschreven in dit proefschrift is de constructie van een TL onderzoeksfaciliteit bestaande uit een zeer gevoelige emissie spectrometer, een annealing oven en een β-bestraler. In hoofdstuk 4 wordt deze onderzoeks faciliteit beschreven. De spectrometer is gebaseerd op een reflectie tralie en een *intesified diode array* (512 elementen). Het golflengtebereik van de spectrometer is 200 nm tot 800 nm en de resolutie is 6 nm als een 25 μm brede ingangs spleet wordt gebruikt en 29 nm als een 1 mm brede spleet wordt gebruikt. De spectrometer kan het spectrum van LiF:Mg,Ti (TLD-100) bestraald met een dosis van 75 mGy nog meten met een signaal ruis verhouding van 10:1. In hoofdstuk 4 wordt een gedetailleerde beschrijving gegeven over hoe het gemeten spectrum gerelateerd kan worden aan een spectrum voorspeld door een model. Hierbij wordt rekening gehouden met alle afwijkingen van het detectiesysteem.

Een belangrijk onderdeel van een TL meting is de verhitting van een monster tijdens de uitlezing. Doordat het monster geen ideaal warmtecontact maakt met het verhittingselement, zal er een temperatuursachterstand in het monster t.o.v het verhittingselement ontstaan. In hoofdstuk 5 wordt een simpel model voor warmte overdracht gebruikt om een schatting te maken van deze temperatuursachterstand en wordt nagegaan wat de invloed op de analyse van de gloeicurve en het emissie spectrum is. Bij de schatting van de temperatuursachterstand kunnen de temperatuursverschillen in het monster worden verwaarloosd. De temperatuursachterstand van een LiF monster met de afmetingen 3.2x3.2x0.9 mm^3 is ongeveer $\Delta T = 1.7\beta + 0.037(T_1 - T_g)$ waarin T_1 de temperatuur van het verhittingselement, T_g de temperatuur van de omgeving en β het opwarmtempo is.

In hoofdstuk 6 staan de resultaten van metingen van de TL-emissiespectra van een LiF:Mg,Ti (TLD-100) monster en drie LiF:Mg,Ti monsters met

verschillende concentraties Mg en Ti (0-6 ppm Ti en 80-100 ppm Mg). De metingen zijn uitgevoerd bij verschillende opwarmtempo's, thermische behandelingen en verschillende bestralingsdoses. Bij bestralingsdoses lager dan 22 Gy bevatten de spectra van het TLD-100 monster en het monster zonder Ti maar één emissie band bij 420 nm en 620 nm respectievelijk. De TL emissiespectra van de andere monsters bevatten twee emissiebanden, één bij 420 nm en één bij 620 nm. De verhouding tussen de intensiteiten van de twee emissiebanden verandert als functie van de temperatuur gedurende de uitlezing. De mate van verandering hangt af van de thermische behandeling die de monsters hebben ondergaan. De verandering in de verhouding tussen de intensiteiten van de emissiebanden wordt met behulp van defectreacties verklaard. De gloeipieken bij verschillende emissiebanden blijken een verschillende dosis responsie op te leveren Dit suggereert dat de plaats in het TL materiaal waar energie wordt opgeslagen, dicht in de buurt ligt van de plaats waar TL wordt geproduceerd.